

Exchange Bias Systems studied by High Resolution Quantitative Magnetic Force Microscopy

INAUGURALDISSERTATION

zur

Erlangung der Würde eines Doktors der Philosophie

vorgelegt der

Philosophisch-Naturwissenschaftlichen Fakultät

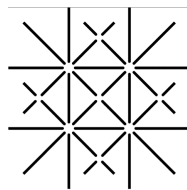
der Universität Basel

von

Sevil Özer

aus Istanbul (Turkei)

Basel, 2012



UNI
BASEL

Genehmigt von der Philosophisch-Naturwissenschaftlichen Fakultät
auf Antrag der Herren Professoren:

Prof. Dr. Hans Josef Hug
Prof. Dr. Ernst Meyer
Prof. Dr. Martino Poggio

Basel, den 22 May 2012

Prof. Dr. Martin Spiess , Dekan

Abstract

It is generally believed that exchange bias (EB) implies the presence of pinned uncompensated moments pin-UCS in the antiferromagnet (AF) layer that are coupled to the ferromagnet (F) layer. An obstacle to understanding the EB effect is that only a subset of the UCS (those pinned and coupled to the F) are responsible for the EB-effect. The materials used, but also the experimental method and preparation may affect these subsets of UCS in distinct ways [19], and an interpretation of UCS measurements must take this into account. Moreover, the materials morphology, texture, defect density and nature of grain boundaries influence the density and spatial distribution of the pin-UCS. Experimental methods that measure the pin-UCS density distribution with spatial resolution comparable to the materials' grain size are needed.

Here we study F/AF heterostructure-samples by VSM and quantitative, high resolution MFM. MFM works in magnetic fields (up to several T) but is not element specific. Analyzing data acquired with the F-layer in the saturated state and with different magnetization states of the tip allows the separation of the different sources of MFM contrast. Using quantitative MFM we measure the local areal density of pinned uncompensated moments (pin-UCS) in the antiferromagnetic (AF) CoO layer and correlate the F-domain structure in a perpendicular anisotropy CoPt multilayer with the pin-UCS density [15]. Larger applied fields drive the receding domains to areas of proportionally higher pin-UCS aligned antiparallel to F-moments. This confirms our prior results [19] that these antiparallel pin-UCS are responsible for the EB-effect, while parallel UCS coexist. The data confirm that the evolution of the F-domains is determined by the pin-UCS in the AF-layer, and also present examples of frustration in the system. This frustration and the inhomogeneous spatial distribution of the pin-UCS also have a major effect on the coercivity of the EB-systems that has not yet been accounted for. Moreover, grain-boundary engineering can be used to decouple the AF grains leading to a stronger EB-effect but a smaller coercivity.

New approaches with rare-earth-ferrimagnet/ferromagnet bilayers to increase unidirectional anisotropy provided by the EB-effect will be discussed.

Contents

Abstract	i
Introduction and Outline	2
1 Exchange Bias Review	3
1.1 Early theory: Meiklejohn and Bean's Model	3
1.2 Domain wall model of the uncompensated interface: Mauri Model	5
1.3 Malozemoff Random Interface Model	7
1.4 Uncompensated Interfacial AF spins: Takano Model	8
1.5 Domain State Model	9
1.6 Spin Glass Model	10
2 Introduction to Quantitative MFM	12
2.1 Magnetic Force Microscope	12
2.2 MFM Image Formation	15
2.3 MFM Operation Mode	18
2.4 Calibration of the Magnetic Tip	19
2.5 Summary	24
3 Quantitative Assessment of Exchange Bias Systems	25
3.1 Types of Magnetic Moment in Exchange-biased Samples	25
3.2 Overview on Neutron and X-ray Dichroism Method	28
3.3 How to Image p-UCS by MFM	29
3.3.1 First MFM experiments on Exchange Biased Samples	29
3.3.2 Separation of Van der Waal's and Magnetic Forces	31
3.3.3 Design of EB-sample for high-resolution MFM imaging	32
3.3.4 Engineering the domain size [1]	37
3.3.5 Analysis of the Topography Induced Magnetic and Non-magnetic contrast	42
3.3.6 Areal density of the pinned uncompensated AF moments	43
3.4 Discussions and Conclusions	46
4 Enhancement of the Exchange Bias	49
4.1 Coupling frustration at F/AF interfaces and exchange bias	49
4.1.1 Frustration from exchange-coupled AF-grains	50
4.2 Exchange-decoupling Antiferromagnet Grains	51
4.2.1 Magnetometry of EB-samples with AF grain decoupling	52

4.2.2	Microscopic consequences of inter-grain decoupling: MFM results	54
4.2.3	Pinned uncompensated spin distribution in AF with decoupled grains . . .	55
4.3	Conclusions	57
5	Giant Exchange Bias: beyond 1 Tesla	59
5.1	Tb ₂₃ Fe ₇₇ based Thin Film Structures	59
5.1.1	Macroscopic characterization of Tb ₂₃ Fe ₇₇ -based thin-film structures . . .	60
5.1.2	Microscopic characterization of Tb ₂₃ Fe ₇₇ -based thin-film structures by MFM	63
5.2	Conclusions	67
6	Conclusions and Outlook	68
	Bibliography	89
	List of Figures	89
	List of Symbols & Abbreviations	89
	List of Publications	89
	List of Presentations and Publications	89
	Acknowledgements	89

Introduction and Outline

Coupling different types of magnetic thin film materials is crucially important for the function of modern magnetic thin film-based devices. An especially prominent case is the coupling between ferromagnetic (F) and antiferromagnetic (AF) thin films that generate a unidirectional anisotropy of the ferromagnet, called exchange bias effect (EB-effect) and a pinned magnetic moment in the antiferromagnet. The first lead to a horizontal shift of the ferromagnetic hysteresis loop. The pinned AF moments often generate a vertical shift of the hysteresis loop. The EB-effect, is essential for the state-of-the-art magnetic read-head technology [2, 3], highly sensitive magnetic field sensors [4] and MRAM devices [5, 6].

The EB-effect was discovered more than 50 years ago [7, 8] and it is nowadays widely accepted that pinned uncompensated spins (UCS) in the AF must play a key role for the EB effect [9, 10]. However, the mechanisms leading to uncompensated spins, the pinning of at least a part of them to the antiferromagnetic lattice and their spatial distribution are still strongly debated. In the past decade many experimental techniques to detect, image and quantify such uncompensated spins, and to determine their role for the EB-effect became available [11, 12, 13, 14, 15, 16, 17, 18, 19, 20]. Among them, developed by the group of my Ph.D. advisor, magnetic force microscopy [12, 13, 15, 19].

The goals of this thesis are the:

- further development high-resolution and quantitative magnetic force microscopy methods to image the spatial distribution of pinned uncompensated spins,
- quantification of the local density of uncompensated spins and the correlation of these microscopic to macroscopic quantities related to the EB-effect,
- understanding the role of the uncompensated spins for the EB-effect
- understanding the mechanisms leading to uncompensation of AF spins
- development of materials systems with improved exchange bias

This thesis is structured into 5 chapters. After a short review of the relevant models for the EB-effect (chapter 1) the quantitative magnetic force microscopy methods used in this thesis are discussed in detail in chapter 2. Chapter 3 is devoted to the separation of the various contributions to the measured tip-sample interaction. The deconvolution of the contrast contribution arising from the pinned uncompensated moments and the determination of the local areal magnetic moment density is discussed in detail. Chapter 4 describes one method - applied for the first time in this thesis - to enhance the EB-effect. Relevant macroscopic parameters related to

the EB effect are compared to maps of pinned uncompensated spins imaged by MFM for conventional and improved antiferromagnetic materials. In chapter 5 we demonstrate that a much stronger EB-effect and exchange coupling is obtained, if the antiferromagnet is replaced by a rare-earth (RE) ferrimagnet. In such systems a new type of magnetization process is observed.

Chapter 6 summarizes the work and relates our experimental results to models of the EB-effect.

Chapter 1

Exchange Bias Review

The coupling of a ferromagnetic and antiferromagnetic thin film leads to a unidirectional magnetic anisotropy, i.e. to a preferred direction of the magnetization (EB-effect), and hence to a horizontal shift of the magnetic hysteresis loop. Often a vertical shift of the hysteresis loop attributed to a remanent magnetic moment attributed to pinned moments in the AF is observed. In this chapter a few relevant models explaining certain aspects of the EB-effect are reviewed.

1.1 Early theory: Meiklejohn and Bean's Model

A unidirectional magnetic anisotropy was first observed by Meiklejohn and Bean in CoO covered Co particles [7, 8, 21]. The EB effect was attributed to the existence of the CoO shell. In their first model was based on the following prerequisites:

- The F and AF layer are in a single domain state,
- The F magnetization rotates coherently if a field opposite to the direction of the ferromagnetic magnetization is applied,
- The AF magnetic lattices are rigid,
- The F/AF interface is atomically smooth and chemically sharp,
- There is a net unidirectional exchange coupling across the F/AF interface which is attributed either to the complete uncompensation of a perfect AF surface or to a partial uncompensation of the two antiferromagnetic sub-lattices at the F/AF interface (uncompensated moments).

Based on these conditions, Fig. 1.1 schematically explains the emergence of the exchange bias effect after field cooling an F/AF system. For a temperature between the Curie temperature, T_C , of the F and the Néel temperature, T_N , of the AF, the moments of F align along the direction of the applied field, whereas the AF moments remain in a disordered paramagnetic state (a). When field cooling to $T < T_N$ (b), the exchange coupling across the interface will align one of the AF sub-lattice moments in relation to the direction of the F magnetization. When reversing the field (c) the F moments start to rotate coherently (prerequisite of the Meiklejohn and Bean model), and finally reverse in a sufficiently strong field (d). The frozen AF moments then exert a

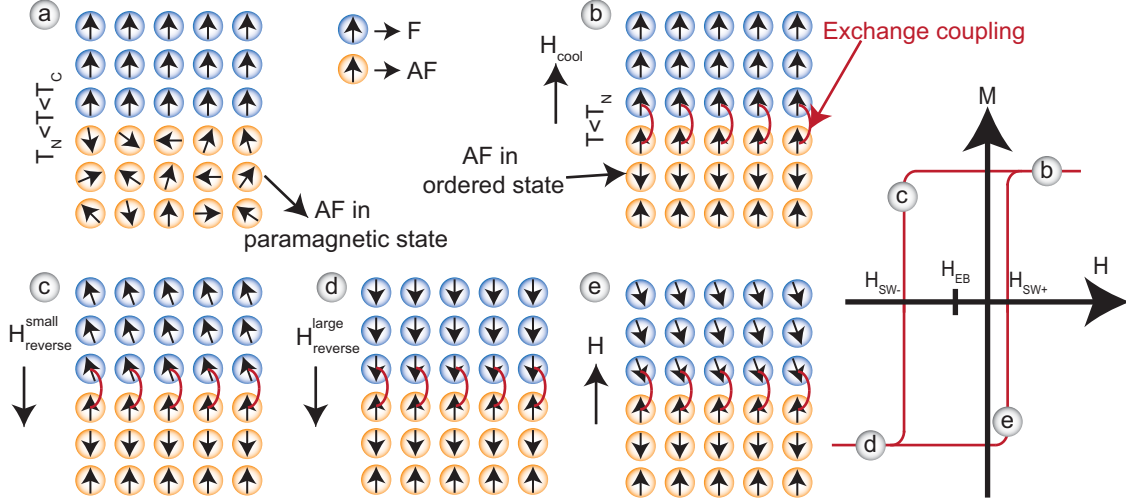


Figure 1.1: Phenomenological model of exchange bias for an F/AF bilayer. Indicated places in the hysteresis loop shows the corresponding magnetic moment configuration. In (a) the magnetic moment configuration at a temperature which is higher than T_N and smaller than T_C . AF-layer is in paramagnetic state while F-layer is ordered. (b) is the state after cooling the system below T_N , assuming a ferromagnetic coupling of AF and F moments at the interface due to the uncompensated moments at the interface. (c) Reversing the field starts to rotate the F moments but not the AF's. (d) the F magnetization has been completely reversed. (e) Reverse back the field into original direction will start to rotate F moments at smaller field. This appears as a shift in the field axis of the M-H loop.

restoring torque on the F moments, that helps to reset the initial magnetization direction if the reversal field is lowered or after applying a small re-setting field in the direction of the cooling field (e). The unidirectional anisotropy arising from F/AF coupling leads to the coercive fields to become asymmetric. The F magnetization prefers the direction set by the cooling field.

In the model, the energy per unit area, A (assuming coherent rotation of magnetization) is written as:

$$\frac{E}{A} = -\mu_0 H \cdot M_F \cdot t_F \cdot \cos(\Theta - \beta) + K_F \cdot t_F \cdot \sin^2(\beta) - J_{eb} \cdot \cos(\beta) \quad (1.1)$$

where H is the applied magnetic field which makes an angle Θ with respect to the cooling direction $\Theta = 0$, M_F is the F saturation magnetization, and t_F is the thickness F-layer. K_F is the uniaxial anisotropy of F which is assumed to be parallel to the cooling field direction, and J_{eb} is the interface exchange anisotropy. The angles are illustrated in Fig. 1.2 (a).

In an extension of the their model, they allowed the sub-lattice magnetization to rotate coherently away from the AF anisotropy axis and cooling field direction (Fig. 1.2 (b)). Further, the anisotropy of F was neglected, because often $K_{AF} t_{AF} \gg J_{eb} \gg K_F t_F$ is fulfilled, where the K_{AF} is the anisotropy of the AF. Eqn. 1.1 then becomes

$$\frac{E}{A} = -\mu_0 H \cdot M_F \cdot t_F \cdot \cos(\Theta - \beta) + K_{AF} \cdot t_{AF} \cdot \sin^2(\alpha) - J_{eb} \cdot \cos(\beta - \alpha). \quad (1.2)$$

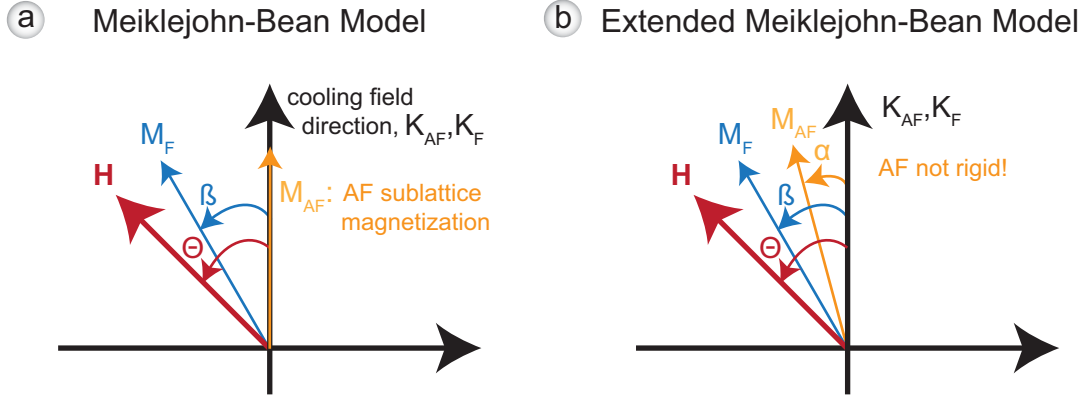


Figure 1.2: Schematics diagram of angles and vectors involved in Meiklejohn and Bean model. Note that the F and AF anisotropy axis (K_F and K_{AF}) are assumed to be collinear and that the AF sub-lattice magnetization M_{AF} has two opposite directions.

The definitions of the angles are illustrated in Fig. 1.2 (b). Assuming further that the AF anisotropy is sufficiently large, $K_{AF}t_{AF} \gg J_{eb}$, the minimizing of Eqn. 1.2 with respect to α and β , reveals

$$H_{eb} = -\frac{J_{eb}}{\mu_0 M_F \cdot t_F} \quad (1.3)$$

Note that both a unidirectional F/AF coupling and the condition for $K_{AF}t_{AF} \gg J_{eb}$ are required for the EB-effect. The exchange bias field predicted by these calculations depends on the assumed value of J_{eb} , and on the thickness and magnetization of the F. An agreement with experimental data is however obtained only if J_{eb} is chosen very small compared to typical intrinsic F or AF exchange coupling constants.

1.2 Domain wall model of the uncompensated interface: Mauri Model

In a better description of the interfacial magnetic state, the coherent rotation of the AF moments, a prerequisite of the Meiklejohn and Bean model is given up. Néel *at al.* [22] has proposed a partial domain wall formation in a weakly anisotropic uncompensated AF-layer which is coupled to an F-layer. This AF partial domain wall will store an important fraction of the exchange coupling energy, thus lowering the shift of the hysteresis loop. Partial domain wall concept was an important milestone in understanding of EB-effect, later it became a basis for further models [23, 24, 25] which use either Néel or Bloch wall formation to explain the reduced observed exchange bias.

In 1987, Mauri *at al.* [23] and coworkers proposed the first domain model of exchange bias. They suggested that the reversal of the F magnetization induces a partial domain wall parallel to the interface inside AF.

The main assumptions of this model were:

- F/AF interface coupling across a perfect flat interface,

- The antiferromagnetic interfacial layer is uncompensated,
- Parallel magnetization of the F and AF sub-lattices in the absence of an external field,
- An F layer thickness much smaller than the F domain wall width and the spins within F rotate coherently,
- A domain wall (DW) develops inside the AF. Note that AF-layer is infinitely thick, no restrictions for the AF domain wall formation due to thickness.
- And lastly, the AF-layer has a uniaxial anisotropy.

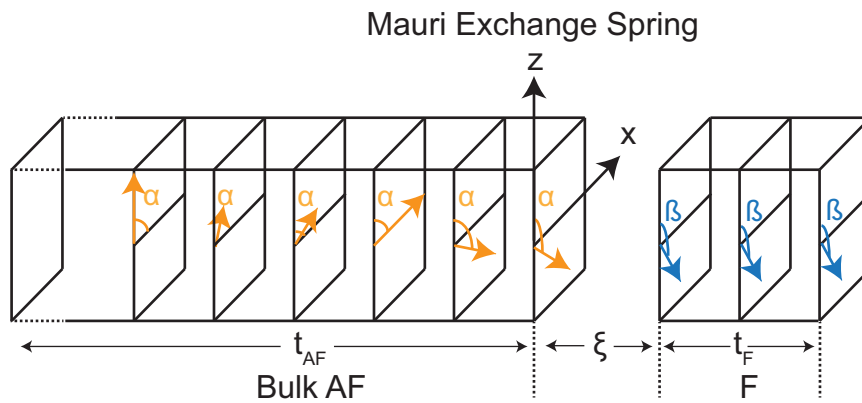


Figure 1.3: Mauri-Siegmann model of exchange bias. F film of thickness t_F is separated by an interface of thickness ξ from a thick AF. The uniaxial anisotropy of the AF is along z , and there is parallel coupling between the uncompensated interfacial moments and the F moments. The external field is applied at an angle β with respect to z and the F moments are aligned parallel to H . Near the interface the AF axis may rotate and form a domain wall. The rotation of the AF axis is given by $\alpha \leq \beta$, and depends on the magnetocrystalline anisotropy of AF [23].

The micromagnetic configuration suggested by Mauri is shown in Fig. 1.3. The anisotropy of the AF is along the z -axis. The ferromagnetic moments are assumed to rotate coherently by an angle β in an applied external field H and apply a torque to the moments of the first AF (sub-lattice) layer via an interfacial layer of thickness ξ and an interlayer coupling stiffness A_{12} . The moments of the first AF-layer are then rotated by an angle $\alpha < \beta$ and a partial domain wall is formed inside the AF. The areal energy density of this AF domain wall is given by

$$E/A = -2\sqrt{A_{AF}K_{AF}}(1 - \cos(\alpha)) \quad , \quad (1.4)$$

where A_{AF} and K_{AF} are the exchange stiffness and anisotropy of the AF. Mauri then replaces the energy term $K_{AF}t_{AF}$ for the coherent rotation of the AF in the Meiklejohn and Bean model (Eqn. 1.2) by Eqn. 1.4. Using the dimensionless parameters $\lambda := J_{eb}/(2\sqrt{A_{AF}K_{AF}})$, where the interface coupling energy J_{eb} is redefined as $J_{eb} := A_{12}/\xi$, $\mu := K_F t_F / 2\sqrt{A_{AF}K_{AF}}$ the reduced ferromagnetic anisotropy, and $k := \mu_0 H M_F t_f / 2\sqrt{A_{AF}K_{AF}}$ the reduced Zeemann energy, two

limiting cases have been described:

$$H_{eb} = -\frac{\left(\frac{A_{12}}{\xi}\right)}{\mu_0 M_F t_F} \quad (1.5)$$

for $\lambda \ll 1$, and,

$$H_{eb} = -\frac{2\sqrt{A_{AF}K_{AF}}}{\mu_0 M_F t_F} \quad (1.6)$$

for $\lambda \gg 1$.

In the weak coupling limit, $\lambda \ll 1$, the expression for the exchange field becomes identical with that of the Meiklejohn and Bean model (M+B model) if $J_{eb}^{M+B} = A_{12}/\xi$. In the strong coupling case, $\lambda \gg 1$, the exchange field is reduced, because the formation of a partial domain wall inside the AF costs less energy than a coherent rotation of the AF sub-lattice magnetization.

The Mauri model gives exchange field values consistent with experimental data. The exchange energy is spread out over a domain wall width $\sim \pi\sqrt{A_{AF}K_{AF}}$ instead of a single atomically wide interface, so the interfacial exchange energy is reduced by a factor of $\pi\sqrt{A_{AF}K_{AF}}/a$, which is a reduction of about two orders of magnitude.

1.3 Malozemoff Random Interface Model

In 1987, Malozemoff [26, 27, 28] introduced a random field model. He argued that the chemically and structurally rough interface causes a spatial variation of the local exchange bias field. This causes the formation of AF domains to minimize the total energy Fig. 1.4 (a). Fig. 1.4 (b) illustrates the pinning of a domain wall in the F. Assuming that the interfacial energy of one AF domain, σ_1 , differs from that of a second σ_2 , the field required to move the F-domain wall becomes

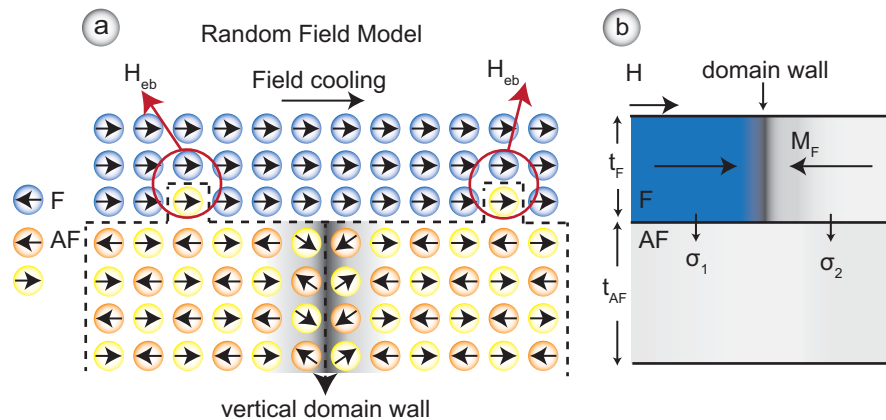


Figure 1.4: Schematic view of the vertical domain wall in AF layer (a), it appears as energetically favourable state of F/AF systems with rough interfaces. (b) schematic side view of the F/AF bilayer with a ferromagnetic wall driven by an applied field H .

$$H_{eb} = -\frac{\Delta\sigma}{2\mu_0 M_F t_F} \quad (1.7)$$

where $\Delta\sigma = \sigma_2 - \sigma_1$. Clearly, an ideally compensated interface will not generate an exchange bias effect, because $\Delta\sigma = 0$ everywhere. For an ideally uncompensated interface $\Delta\sigma = 2J_i/a^2$ on an atomistic scale, where J_i is the cross-interface exchange coupling constant and a is the lattice parameter. Then the exchange bias field becomes

$$H_{eb} = \frac{J_i}{a^2\mu_0 M_F t_F} \quad (1.8)$$

which is a field determined by the intrinsic coupling strength, and therefore orders of magnitude beyond experimental field values. Malozemoff then introduces a random interfacial coupling field. On a local scale such a random field generates a unidirectional anisotropy, but it rapidly decreases with the size of the interfacial area that is considered. It then becomes energetically favorable to break up the AF into domains Fig. 1.4 (a), that make use of the local unidirectional anisotropy. This leads to the following expression for the exchange bias field

$$H_{eb} = \frac{2z\sqrt{A_{AF}K_{AF}}}{\pi^2 M_F t_F} \quad (1.9)$$

where z describes the disorder of the F/AF interface and $\sqrt{A_{AF}/K_{AF}}$ is a measure for the domain wall energy. With Eqn. 1.9 exchange bias fields comparable to those obtained from experiments are found.

1.4 Uncompensated Interfacial AF spins: Takano Model

Meiklejohn and Bean originally suggested that unidirectional anisotropy was a consequence of the presence of uncompensated interfacial AF moments. However, the experimental confirmation of the existence of such pinned uncompensated moments was proven by Takano and coworkers [17, 18] in 1997, 40 years later. They measured the thermoremanent magnetization (TRM) after field cooling a series of CoO/MgO multilayers from $T > T_N$ to $T < T_N$. They concluded that the moments responsible for the TRM are located at the interface and only about 1 % of the AF moments of a fully uncompensated monolayer of CoO. Furthermore, the TRM showed the same temperature dependence as the exchange field of Ni₈₁Fe₁₉/CoO bilayers. Because the origin of the TRM was attributed to uncompensated interfacial AF moments, they concluded that unidirectional anisotropy arises from this uncompensated interfacial AF moments. The low density (≈ 1 %) of these moments also explains the observed low exchange fields compared to the predicted values by the ideal interface model (see section 1.1). Based on their experimental results, they proposed a model to explain the small interfacial density of uncompensated moments and the $\frac{1}{L}$ -dependence of H_{eb} with the size of the AF crystallites, L , in polycrystalline AF materials.

Takano *at al.* [17, 18] describe the coupling energy of each AF crystallite in a Heisenberg-like model as

$$U_{cryst} = -|J_{eb}|S_{AF} \cdot S_F \quad (1.10)$$

For an interfacial area A a coupling energy

$$U_{eb} = U_{cryst} \cdot \frac{A}{L^2} \quad (1.11)$$

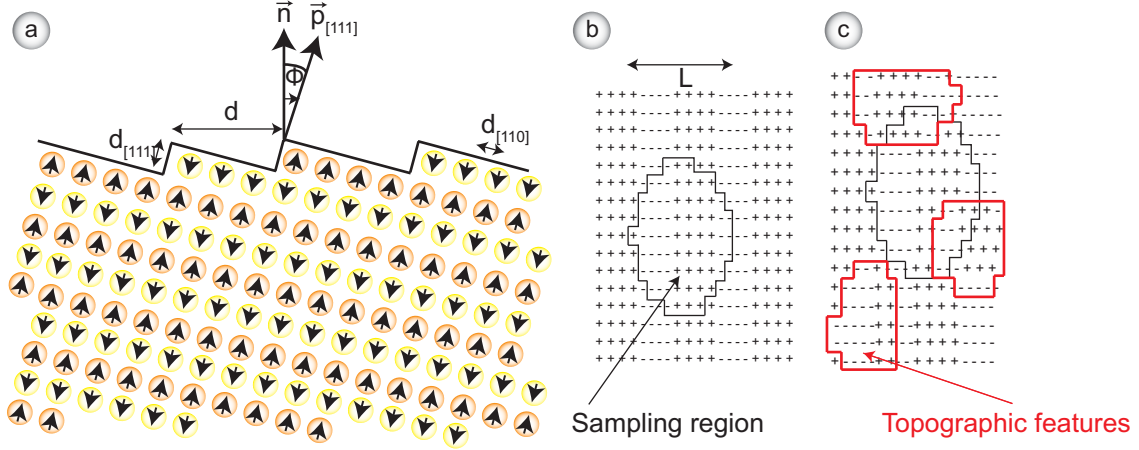


Figure 1.5: Schematic of Takano model: (a) shows a schematic of the interface cross section of an AF grain. \vec{n} is the film normal, and \vec{p} is the normal to the parallel [111] spin planes of AF. (b) shows a topographical representation of the interfacial plane as shown in (a) with a sampling region representing a model crystallite. (c) shows the elliptical “islands” of monoatomic layer thickness which were superimposed on the spin map to simulate roughness. Note that adding one atomic layer reverses the direction of the underlying spin.

is found, where $\frac{A}{L^2} = N_c$ is the number of crystallites in the area A . Using a model interface as depicted in Fig. 1.5 (a), Takano *et al.* found that the number of uncompensated moments in a sampling area described by the grain diameter L (Fig. 1.5 (b)) becomes

$$\langle \Delta N \rangle \propto L^{0.5}. \quad (1.12)$$

If roughness is introduced in addition (Fig. 1.5 (c)), they found

$$\langle \Delta N \rangle \propto L^{0.9-1.04} \quad (1.13)$$

together with Eqns. 1.10 and 1.11 the experimentally observed $\frac{1}{L}$ -dependence of H_{eb} is explained.

1.5 Domain State Model

Based on previous work on diluted antiferromagnets cooled in external fields (DAFF models) [29] and their own experimental work that showed an increased exchange bias in systems with a defective antiferromagnet [30], Nowak *et al.* [31] introduced a domain state model. They argued that like in a DAFF system, a defective AF would break up into domains such that at the F/AF interface the defects would lead to a net uncompensation of the two AF sub-lattices. The defects in the AF would facilitate the formation of domain walls because the energy cost of these walls is reduced if they run through the non-magnetic defects. The domains would then have very irregular shapes and extend into the bulk of the AF. Defect in the AF bulk would therefore also facilitate domain formation and hence an uncompensation of the AF interfacial moments. Fig. 1.6 (taken from their work [31]) schematically shows the interface surface of the AF. The domain enclosed by the black lines (domain walls) has three net up moments, but five AF bonds

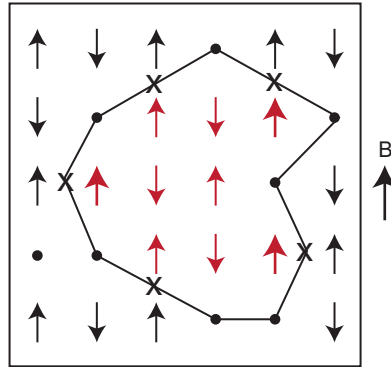


Figure 1.6: Sketch of the model with one F layer, and three diluted AF layers in (a). The dots mark defects. (b) shows the schematic illustration of the Imry-Ma argument.

or antiferromagnetic exchange interactions have to be broken. In a sufficiently high external field, the Zeemann energy will become larger than the energy of the broken bonds. Hence a domain as shown in Fig. 1.6 will form and the three net moments will align parallel to the field. In their work, Nowak *et al.* [31] point out that the coupling to these net-moments to the F can take the role of an external field and drive domain formation. Monte-Carlo simulations were used to study the effect of defect concentration on the EB-field, ferromagnetic hysteresis, training effect, cooling field and AF thickness dependence all with excellent qualitative and good quantitative agreement with experimental data. It was further pointed out that spin glasses similar mechanisms are at work to generate exchange bias.

1.6 Spin Glass Model

Radu *at al* and coworkers [32, 33] proposed a model based on the magnetic state of the interface between F and AF layers which is magnetically disordered, and behaving as spin glass system. The basic assumptions of this model are:

- At the F/AF interface two distinct magnetic states, one coupled strongly to the AF with a high unidirectional anisotropy and a second with a weaker coupling to the AF, i.e. with a lower anisotropy exist.
- The higher anisotropy magnetic state is pinned to one of the AF sub-lattices, and is responsible for the exchange bias effect.
- The lower anisotropy magnetic state part reverses with the F moments and responsible for the coercivity enhancement.

The presence of the low anisotropy magnetic state is attributed to frustration arising from disorders at the interface, such as the chemical intermixing, deviations from the stoichiometry, structural inhomogeneties, low coordination, breaking symmetries etc.

The schematic view on the magnetic moments distributions is depicted in Fig. 1.7 [32, 33]. The AF moments which have weaker (rotatable) and the higher (frozen) anisotropy are labelled

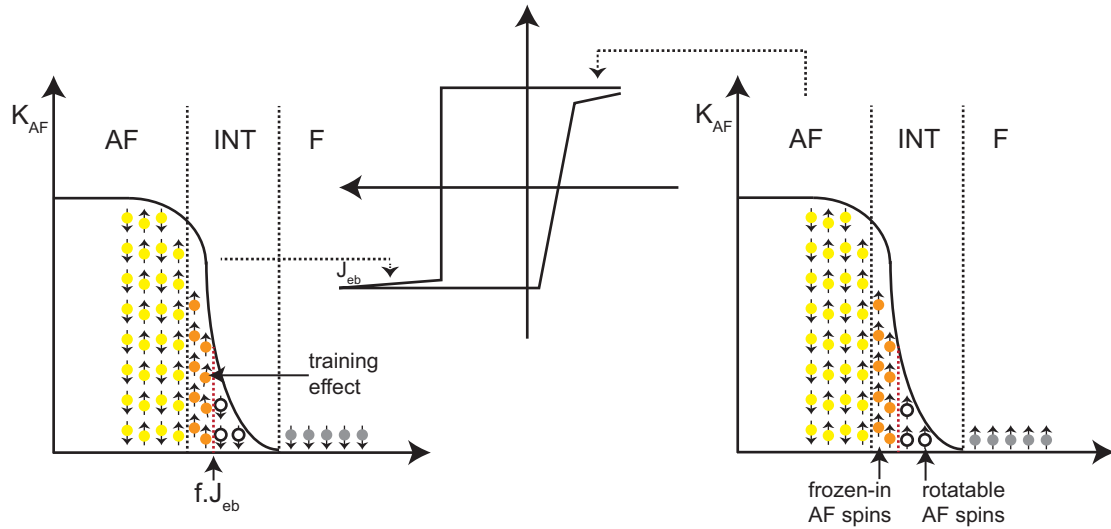


Figure 1.7: Schematic view of the F/AF moment arrangement in the spin glass model. At the interface between the F and AF layers, the AF anisotropy is assumed to be reduced. It has two types of AF uncompensated moments which are frozen and rotatable ones.

as open and orange filled circles, respectively. The right panel of Fig. 1.7 pictures the magnetic moments configuration after field cooling. It shows a collinear arrangement at the interface. After reversing the external field, the rotatable AF moments will follow the F moments (labelled with grey circles) and lead to the coercivity enhancement. The frozen AF moments remain unchanged in moderate external fields and lead to the exchange bias effect. However, some of these moments may deviate from its cooling direction and lead to the often observed training effect (see the open loop at the right side of the hysteresis loop).

In this model, the energy per unit area becomes

$$\frac{E}{A} = -\mu_0 \cdot H \cdot M_F \cdot t_F \cdot \cos(\Theta - \beta) + K_F \cdot t_F \cdot \sin^2(\beta) + K_{AF} \cdot t_{AF} \cdot \sin^2(\alpha) + K_{eff}^{SG} \cdot \sin^2(\beta - \gamma) - J_{eff} \cdot \cos(\beta - \alpha) \quad (1.14)$$

where the first three terms are the same as in Meiklejohn and Bean model, the fourth term is given an effective anisotropy.

$$J_{eff} = f \cdot J_{eb} \quad (1.15)$$

with $0 \leq f \leq 1$ instead of the intrinsic J_{eb} used in the Meiklejohn and Bean model. The fourth term with

$$K_{SG}^{eff} = (1 - f)J_{eb} \quad (1.16)$$

describes the contribution of the effective spin-glass anisotropy. The angle γ defines the average angle of the spin-glass induced uniaxial anisotropy relative to the sample normal.

Chapter 2

Introduction to Quantitative MFM

This chapter is devoted to a short description of the magnetic force microscopy (MFM) instrumentation (section 2.1) and operation mode (section 2.4) used in this thesis. Relevant aspects about MFM image formation (section 2.2) are summarized from earlier work of our group [34, 35, 36, 37, 38] to allow a later detailed discussion of the results obtained in this thesis. The last section 2.4 describes the calibration process of the MFM tip as used in this thesis.

2.1 Magnetic Force Microscope

Magnetic force microscopy is an imaging technique based on atomic force microscopy [39] that measures the magnetic forces or its derivatives exerted on the tip by a magnetic field and thus image the magnetic structure of the sample. Hence, all scanning force microscope can be used as a magnetic force microscope, using a tip with a magnetic moment. MFM was first introduced in 1987 [40], with the measurement of the forces between the ferromagnetic sample and a tip that carries a permanent magnetic moment. Most of the early work was devoted to imaging written structures in magnetic recording materials and to investigating the contrast mechanism. Since then, magnetic-field-mediated forces have been measured on a wide variety of samples and experiments were successfully performed under many different environmental conditions such as in air, vacuum, ultra high vacuum (UHV), low temperatures and strong magnetic fields.

All the magnetic force microscopy data presented in this thesis were acquired with a home-built UHV low temperature scanning force microscope in Basel [34, 35]. The instrument is operated at a base pressure of 10^{-10} mbar at temperatures down to 5 K and in magnetic fields up to ± 7 T perpendicular to the sample surface with using fiber-optic interferometry as a sensor for the cantilever deflection. The cantilever from Team Nanotech GmbH (improved super-cone tip with a tip radius smaller than 5 nm) has a stiffness of 0.35 N/m^2 and a free resonance frequency in the range of 42.000-52.000 Hz at the measurement temperature of 7-8 K.

UHV system

The LTMFM-instrument consists of two main UHV-chambers which are analysis-preparation chamber and the microscope chamber connected by a valve. A schematic view of the microscope shown in Fig. 2.1 (a). The analysis-preparation chamber is used for samples-cantilever

preparations. It has a heatable and coolable xyz-manipulator, a triple-electron beam evaporator, a quartz microbalance thickness monitor and a transport system. All the magnetic tips used in this thesis prepared in by means of e-beam evaporation of a thin Co layer. Using a transport system, samples and cantilevers can easily be transferred from one chamber to the other through the valve. On the rear side of the preparation chamber, there is a entry air lock which permits an exchange of cantilevers and samples from air into UHV system. The whole UHV system is mounted on a passive damping table to insulate it from the building vibrations and can be baked out at almost 120 C°.

Microscope

The microscope chamber is attached to the cryostat and contains the microscope and UHV-manipulator for sample-cantilever exchange. A schematic cross section of the cryostat containing the MFM in measurement position is shown in Fig. 2.1 (b). The microscope can be moved from manipulation position where the tip-sample is exchanged to the measurement position in the cryostat via bellows system. The cryostat is custom designed by Oxford Instruments and is a super-insulated bath cryostat with a UHV compatible, variable temperature insert. Additionally, it has a superconducting magnet capable of applying fields up to 7 T perpendicular to the sample surface and along the tip axis. In order to control the measurement temperature in a fixed value, a temperature sensor and a heater placed near the sample are used via a digital feedback loop. The heat flow is allowed from a cone of insert which is touching the inner part of the cryostat to keep the microscope in the measurement temperature around 7 – 8 K. The stability of the temperature is about ± 0.5 mK. All the electrical connections and optical fibre are guided along the cryostat-insert. To avoid the vibrational noises, the microscope is spring suspended at the end of the cryo-insert and vibration-insulated via eddy current damping.

The sample is mounted on a piezo tube which can scan in the x, y, z directions with a maximum scan range $6 \times 6 \mu m^2$ (x, y) in the measurement temperature, which is about 8 K (see the microscope in Fig. 2.1 (c)). Below the cantilever chip, there is a dither piezo to actuates the cantilever. The cantilever is driven on resonance f_0 with an oscillation amplitude A kept constant at a fixed value (mostly working in small amplitudes, as 5 nm). The deflection of the cantilever is detected by Fiber-optic interferometer [41]. A cleaved optic fibre end is brought close and parallel to the mirrored backside of the cantilever forming a Fabry-Perot cavity. The backside of the cantilever chip is coated with a thin aluminium (6-8 nm) to improve the reflection of the cantilever. This optical signal is converted by a photodiode into a sine-shaped electrical signal (measurement signal). This sine-shaped signal is treated by electronics. The frequency of the sine wave corresponds to the cantilever frequency and the amplitude can be calibrated using the wavelength of the laser light in order to avoid the contact of the cantilever with the sample surface. Amplitude has to be smaller than a quarter of the laser's wavelength and the distance between the fiber end and cantilever (L) has to be kept constant. In order to keep the L constant, additional piezo which is attached to the fiber is operated in a feedback loop (see Fig. 2.2). Note that the cantilever-fibre system is tilted by an angle of $\theta = 12^\circ$ with respect to the normal of the sample surface to avoid the touching of the sample surface with the cantilever chip. An important consequence of this is that the force (and the force derivative) is not measured along the z -direction but along a direction \mathbf{n} that is canted away from the z -direction by 12° . At the first sight, this looks like a neglectable error in the measurement absolute force, because $\cos 12^\circ = 0.978 \approx 1$. However, because all the derivative is taken along the \mathbf{n} -axis, the canting

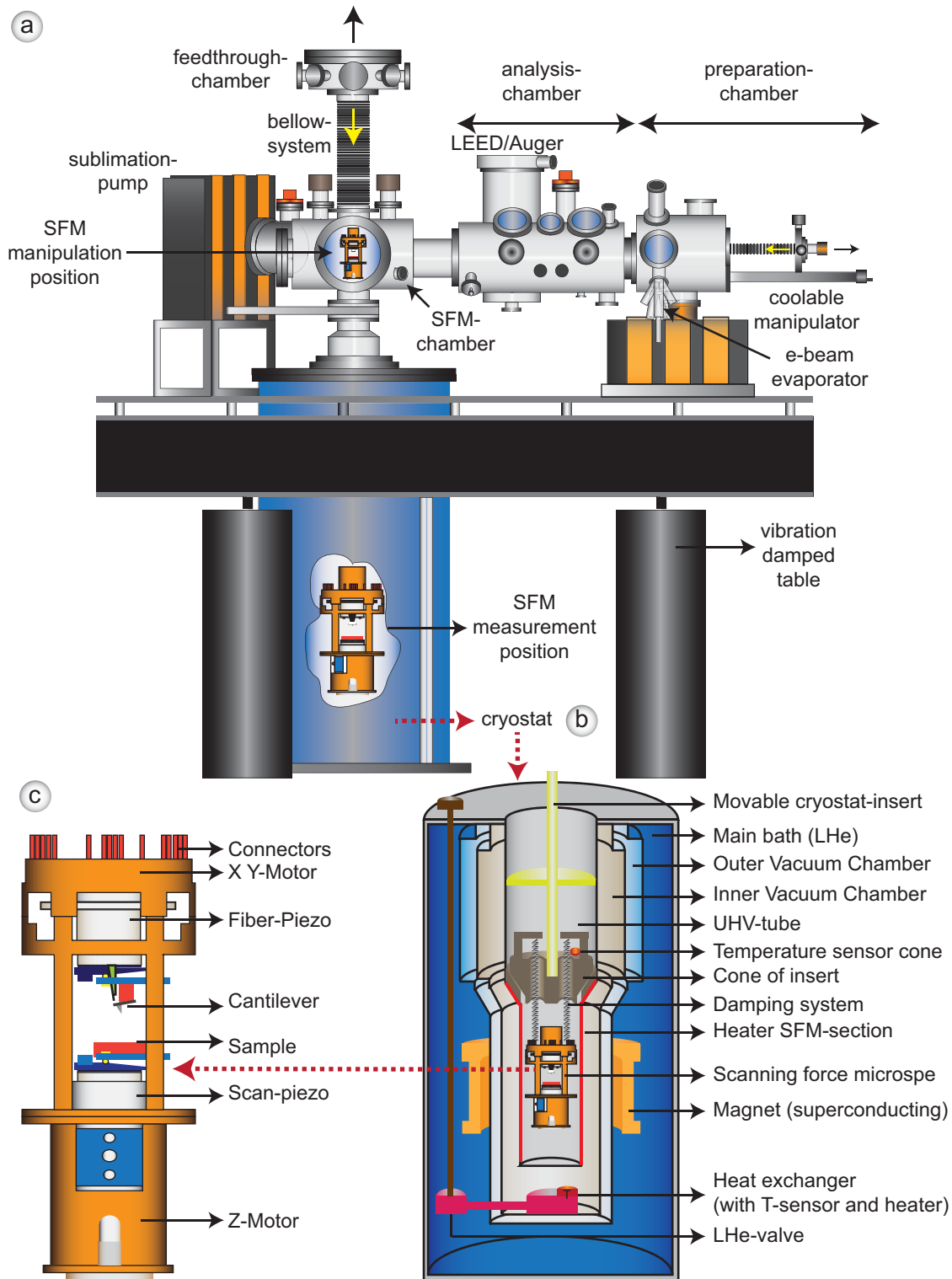


Figure 2.1: Schematics of the LTSFM UHV system. In (a) the microscope and preparation chamber seen on the left and right, respectively. (b) the cryostat, and (c) the scanning force microscope.

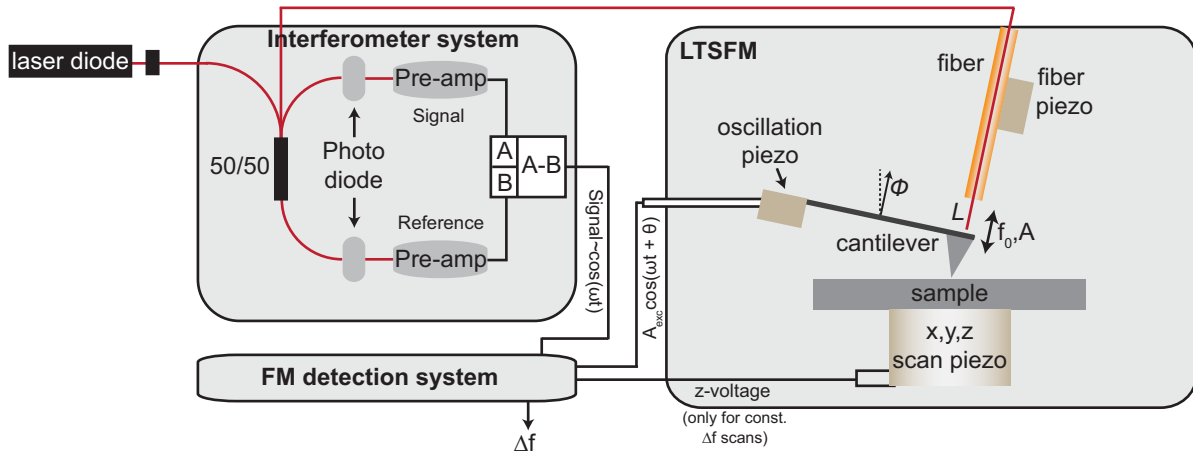


Figure 2.2: Schematic diagram of the LTSFM scanning and data acquisition. Cantilever is driven on resonance f_0 and amplitude A by a piezoelectric. Deflection of the cantilever is detected by Fabry-Perot interferometer.

leads also to a phase shift between the high- and low- spatial frequency Fourier components of the measured and hence to visible image distortions, such that the appropriate correction transfer-functions need to be applied (see section 2.4 and namely Eqn. 2.6, and Fig. 2.5).

A schematic of the scanning and data acquisition electronics with the interferometer system [37] is given in Fig. 2.2. The goal of the electronics to drive the cantilever at its resonance frequency f_0 with a constant amplitude A_0 and measures the frequency shift Δf of the cantilever induced by the force interaction. For this measurement, this is achieved using a fully digital phase-locked loop [42, 43] from NanoScan AG. PLL keeps the phase between the cantilever and a reference oscillator locked. This is done by a feedback loop which compares the phases of the cantilever oscillation and the reference signal. The recorded data comprises the frequency shift Δf , the phase, the oscillation amplitude A , the cantilever excitation (voltage applied to the oscillation piezo, Γ) and the variation in tip-sample distance (voltage applied to z -piezo).

These channels are transmitted to the acquisition software Scandirector developed by NanoScan AG. This software also generates the scan motion (x and y scan signal, plus the z signal to allow the slope correction).

2.2 MFM Image Formation

In order to understand the contrast formation, the interaction of this magnetic tip with the stray field of the sample needs to be analyzed. Here this is done under the assumption that the stray fields of the sample (tip) does not change the magnetization of the tip (sample), respectively.

Then the force acting on the magnetic MFM tip is given by the convolution of the tip magnetization distribution $\mathbf{m}_{tip}(\mathbf{r}')$ with the sample stray field ($\mathbf{B}_{sample}(\mathbf{r}')$)

$$F_{tip}(\mathbf{r}) = \int_{\mathbf{V}_{tip}} (\mathbf{m}_{tip}(\mathbf{r}') \cdot \Delta) \mathbf{B}_{sample}(\mathbf{r}') d^3 \mathbf{r}'. \quad (2.1)$$

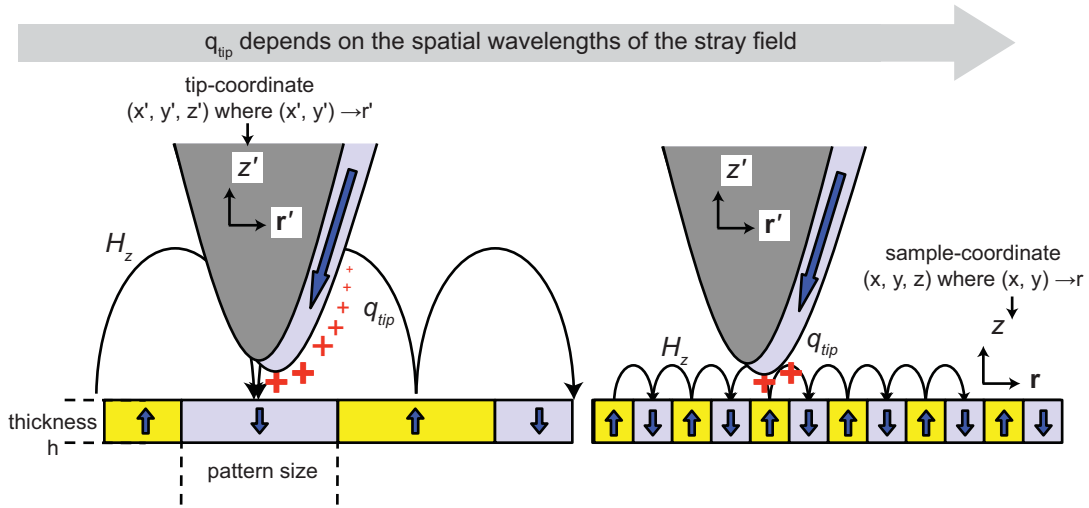


Figure 2.3: Schematics of a magnetic tip over a sample with a large/small domains with up/down magnetization. q_{tip} depends on the spatial wavelengths of the field.

Note that \mathbf{m}_{tip} is the full magnetic moment distribution of the tip and not known. According to Eqn. 2.1, a homogeneous field \mathbf{B}_{sample} does not generate any force on the MFM tip. For MFM measurements performed under vacuum conditions it is advantageous to use a dynamic measurement mode. In this mode the cantilever is driven on resonance at a fixed oscillation amplitude and the force-gradient induces shift of the resonance frequency Δf is measured as a function of the position of the above the sample. For oscillation amplitudes small compared to the decay length of the force field and for a cantilever oscillation along the z -direction, the frequency shift Δf is found to be proportional to the z -component of the tip-sample force,

$$\Delta f_{\mathbf{r}} \approx -\frac{f_0}{2c_L} \frac{\partial F_z(\mathbf{r})}{\partial z}, \quad (2.2)$$

where f_0 is the free resonance frequency of the cantilever, c_L is the force constant of the cantilever. For oscillation amplitudes comparable or larger than the decay length of the force field, the frequency is given by rather complicated equations

$$\Delta f_{\mathbf{r}} = -\frac{f_0^2}{\pi A c_L} \int_0^T \sin(\omega t) F_z(x, y, z + A \sin(\omega t)) dt \quad (2.3)$$

where A is the oscillation amplitude of the cantilever. A calculation of the frequency shift Δf using Eqns. 2.1, 2.2, 2.3 requires knowledge of the magnetic moment distribution $\mathbf{m}_{tip}(\mathbf{r}')$ of the MFM tip and an integration at each point \mathbf{r} above the sample surface (see Fig. 2.3). Both limit the usefulness of Eqns. 2.1, 2.2, 2.3 in practice.

As pointed in our earlier work [44] it is advantageous to describe the MFM contrast in a 2-dimensional Fourier space in which the coordinate triple $\mathbf{r} = (x, y, z)$ is transformed into $(\mathbf{k}, \mathbf{z}) = (k_x, k_y, z)$, where x and y coordinates but *not* the z -coordinate are transformed. Then the MFM frequency shift contrast becomes proportional to z -derivative of the z -component of the sample stray field:

$$\Delta f(\mathbf{k}) = \text{ICF}(\mathbf{k}) \cdot \frac{\partial}{\partial z} H_z(\mathbf{k}) \quad (2.4)$$

where

$$\text{ICF}(\mathbf{k}) = -\mu_0 \frac{f_0}{2c_L} \cdot q_{tip}^*(\mathbf{k}) \cdot \text{LCF}^2(\mathbf{k}), \quad (2.5)$$

is the instrument calibration function. The $\text{ICF}(\mathbf{k})$ contains the mechanical properties of the cantilever (c_L and f_0) and the complex conjugate of the tip-equivalent surface charge distribution function (or in short: tip-transfer function) $q_{tip}(\mathbf{k})$. The latter conveys the sensitivity of the tip for magnetic fields of a specific wavelength described by the wave-vector \mathbf{k} but also reflects the magnetic charge distribution of the tip in Fourier space (see Fig. 2.3). It can be calibrated either as documented in [44] or following procedures described in section 2.4. The cantilever-canting function [$\text{LCF}(\mathbf{k})$] describes the effects of the finite oscillation amplitude A of the cantilever that is canted by 12° relative to the surface normal in our instrument. The LCF can be calculated by

$$\text{LCF}(\mathbf{k}, \phi) = \frac{\mathbf{n} \cdot \nabla}{A \cdot k} \cdot 2\text{I}_1(A \cdot \mathbf{n} \cdot \nabla) \quad (2.6)$$

where I_1 denotes the first order modified Bessel function, and A is the finite oscillation amplitude of the cantilever. In the limit of small oscillation amplitudes Eqn. 2.6 simplifies to

$$\text{LCF}(\mathbf{k}, \phi) = \frac{\hat{\mathbf{n}} \cdot \nabla(\mathbf{k})}{k} \quad (2.7)$$

with where $\hat{\mathbf{n}}$ is the unit vector of \mathbf{n} .

The representation in the 2d-Fourier space also simplifies the calculation of the stray field emanating from the sample. As this work mainly focuses on thin films with perpendicular magnetic anisotropy (exchange-biased structures), we restrict our considerations to slab-like geometries with a h denoting the film thickness of the magnetic structure but infinite planar dimensions. For a thin ferromagnetic film domains with a magnetization perpendicular to the surface the z -component of the stray field and its z -derivative becomes

$$H_z(\mathbf{k}, z) = + \frac{M_z(\mathbf{k})}{2} \cdot e^{-kz} \cdot (1 - e^{-kh}) \quad (2.8)$$

and

$$\frac{\partial H_z(\mathbf{k}, z)}{\partial z} = -k \frac{M_z(\mathbf{k})}{2} \cdot e^{-kz} \cdot (1 - e^{-kh}) \quad (2.9)$$

where $M_z(\mathbf{k})$ is the magnetization (aligned along the z -direction) in Fourier space, $\exp(-kz)$ is the distance-loss factor, and $[1 - \exp(-kh)]$ is the thickness-loss factor with the layer thickness h .

Eqn. 2.8 and Eqn. 2.9 show how the stray field depends on the measurement distance z , thickness of the magnetic layer h and the size of the pattern \mathbf{k} (i.e. size of the domain in Fig. 2.3). Note that the distance-loss factor in Eqn. 2.8 and Eqn. 2.9 expresses the rapid exponential decay for the small-wavelength components of the stray field with increasing distance from the surface. When the domain size is much larger than the sample thickness (i.e. $\lambda \rightarrow \infty$ or $k \rightarrow 0 \Rightarrow [1 - \exp(-kh)] \rightarrow 0$), the stray field above the sample center of a domain, close to the surface of the sample becomes extremely small as long as the thickness is constant and the roughness of the sample is zero. Because the field generated by the magnetic charge at the top surface is almost compensated by that at the bottom surface. The largest field is observed at the domain walls. This is why a homogeneously magnetized sample ($\lambda \rightarrow \infty$), i.e. a saturated ferromagnetic thin film, does not generate a magnetic stray field. These considerations will be of high importance

for the analysis of the contrast measured on exchange bias samples (chapter 3 and 4). The dependence of the domain size on the measurement will be understood clearly in section 3.3.3 which we discuss the engineering the ferromagnetic domain size for optimized imaging of the pinned uncompensated spins in exchange-biased samples.

In contrast to a ferromagnetic, an antiferromagnetic has no net macroscopic magnetization, then it does not exhibit any magnetic stray field, because all magnetic moments are compensated. However, a thin antiferromagnetic film may contain uncompensated magnetic moments which may produce a magnetic stray field. The origin of the uncompensated moments can be explained by an alternating sheets of ferromagnetic spins with an odd number (see Fig. 1.1). A single sheet of antiferromagnetic spins of the atomic scale thickness, i.e. in the limit of small thickness, Eqn. 2.8, and the derivative of the field, Eqn. 2.9 generate a field of

$$\lim_{h \rightarrow 0} H_z(\mathbf{k}, z) = k \cdot \frac{1}{2} \frac{m_z(\mathbf{k})}{A} \cdot e^{-kz}, \quad (2.10)$$

and

$$\lim_{h \rightarrow 0} \frac{\partial H_z(\mathbf{k}, z)}{\partial z} = -k^2 \cdot \frac{1}{2} \frac{m_z(\mathbf{k})}{A} \cdot e^{-kz}, \quad (2.11)$$

respectively. Here we used $M_z(\mathbf{k}) = \frac{m_z(\mathbf{k})}{V}$, and $\frac{m_z(\mathbf{k})}{A}$ is the areal density of the z component of the magnetic moments projected onto one plane.

2.3 MFM Operation Mode

In most SFM experiments, the tip-sample distance is controlled to keep the tip-sample interaction is constant. However, magnetic forces are attractive and repulsive within the imaged sample area and therefore do not fulfill a condition of feedback stability of this mode which is that the derivative of the measured interaction must not change its sign within the scanned image. Consequently, other methods for tip-sample distance control were developed. In this thesis, MFM imaging is performed by measuring the Δf -signal as a function of the xy-position while the sample is scanned parallel to the average sample slope at an average tip-sample distance z_0 . The tip-sample distance is not actively controlled, but can be kept constant sufficiently long times at low temperatures. A fully digital PLL was used to measure the shift of the resonance frequency Δf (see Fig. 2.2). The highest spatial resolution and sensitivity is obtained if the tip is scanned close to the sample surface. However, the tip-sample distance z_0 has to be sufficiently large to prevent the tip from making contact with the highest topographical features in the scanned area. Typically z_0 is a few nanometers.

In order to determine (or set) the tip-sample distance, the dependence of the PLL signals on the tip-sample distance z is measured. Note that in the PLL setup used here an *amplitude feedback* keeps the oscillation amplitude of the cantilever constant by an appropriate adjustment of the cantilever excitation signal (A_{exc}). Fig. 2.4 (a) and (b) show the frequency shift ($\Delta f(z)$), and the excitation signal (A_{exc} drives the cantilever oscillation) as a function of the tip-sample distance z , respectively. The Δf signal first decreases slowly to more negative values as the tip-sample distance is reduced. In the last 15 nm before the tip makes contact with the sample, a rapid decrease to more negative frequency shift values is observed (Fig. 2.4 (a)). This reflects the increasing attractive van der Waals force with a small contribution of the local magnetic

force. Note that the contact potential has been compensated to minimize the electrostatic tip-sample interaction. In Fig. 2.4 (b) two different $A_{exc}(z)$ curves with a z -range of the 46 nm (grey line) and 47 nm (black line) are plotted to illustrate the reproducibility and the effect of the additional 1 nm-sized tip travel of the black approach curve. In the last nanometer, an increase of the excitation signal is detected. It is caused by the transferring energy from the oscillating cantilever into the sample. The distance where this distinct increase of the excitation signal occurs is used to redefine the a-priori relative z -scale. The z -scale given at the top axis of the Figs. 2.4 ((b) but also (a)) is now an absolute distance scale, with zero defined as the point where the tip-sample interaction becomes dissipative.

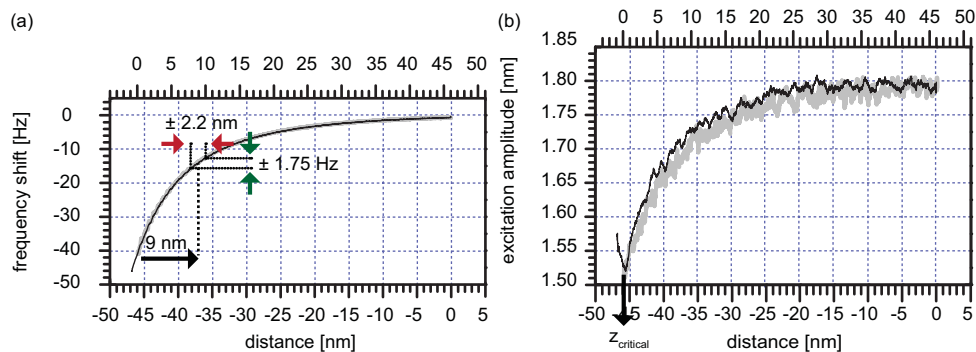


Figure 2.4: The actual tip-sample distance $z_{measured}$ can be determined from the dependence of the A_{exc} -signal on the tip-sample distance z . (a) shows the dependence of the frequency shift on the tip-sample distance travel (bottom z -scale). (b) shows the dependence of the excitation signal on the tip-sample distance. At a tip-sample distance smaller than a critical tip-sample distance $z_{critical}$ the excitation signal increases rapidly. This point in the tip-sample distance is used to define the zero-point of the absolute z -scale shown at the top axis of (b) and also (a). For imaging the tip is retracted 9 nm from this point (a). A topography induced local variation of the tip-sample distance of ± 2.2 nm would then cause a variation of the frequency shift of ± 1.75 Hz.

For the consecutive imaging the tip is retracted from the surface to the $z_o = 9$ nm (black arrow in Fig. 2.4 (a)). At this distance a topography-induced variation of the tip-sample distance of ± 2.2 nm (see the red arrows) would generate a variation of the van der Waals force with the corresponding generated frequency shift of ± 1.75 Hz (see the green arrows).

2.4 Calibration of the Magnetic Tip

As indicated by Eqns. 2.4 and 2.5, the stray field (derivative) of the sample can be deconvoluted from the measured frequency shift data, provided the response function of MFM tip was calibrated. The calibration of MFM tip requires the MFM data of a sample with pattern of up/down domains and a known magnetization. The geometry of the domains can be arbitrary but must contain all spatial frequencies relevant for later deconvolution procedures. Note that sharp domain walls running in different spatial directions generate variations high-spatial components in different directions. For the work performed in this thesis we use the native pattern of domains of the F-layer(s) for the tip-calibration. In some cases the thickness of the F-layer(s)

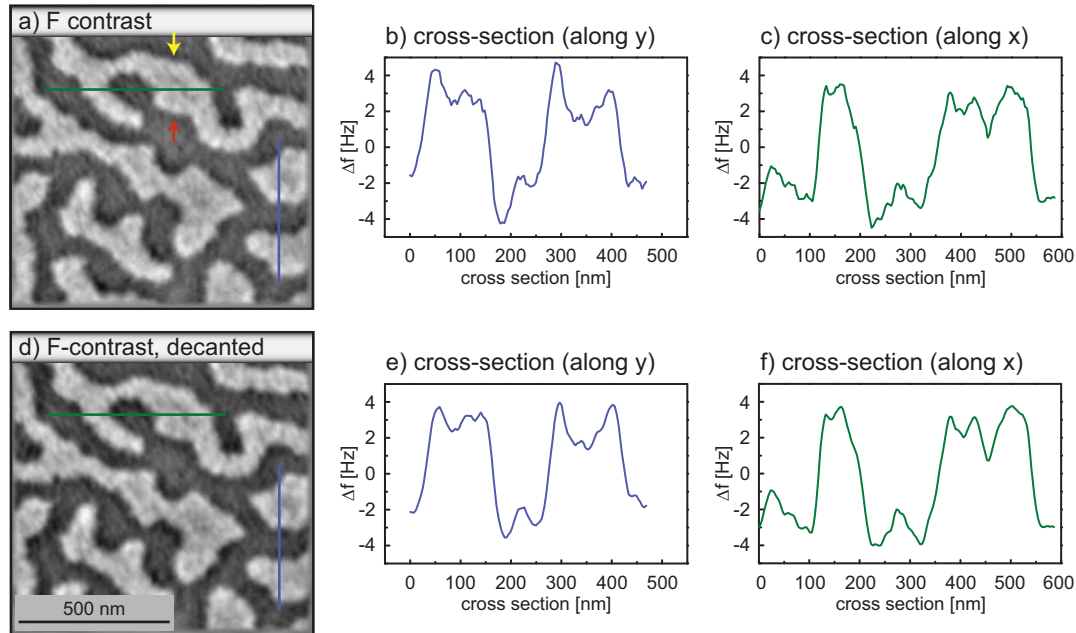


Figure 2.5: (a) MFM contrast caused by the up/down domains of the F-layer only. The contributions of the topography and the AF have been removed. (b) Note that the transitions from up-to-down domains (see red arrow) running along the x-direction show a characteristic dark shadow that is not visible in the corresponding down-to-up transitions in (c) (see yellow arrow). This asymmetry is not visible for domain walls (transition) running along the x-direction. The asymmetry of walls along the y-direction is caused by the canting of the cantilever along this direction by 12° , i.e. by the lever-canting function, $LCF(\mathbf{k})$ (Eqn. 2.6). The *decanted* data is shown in (d). The cross-sections (b) and (e) clearly reveal the effect of the *decanting* procedure. Now the walls running along the x- and y-direction (Fig 2.5 (e) and (f)) are symmetrical.

was (were) engineered to obtain a domain pattern with a domain size suitable for calibration and also for fulfilling additional conditions as discussed in in section 3.3.4. Further as will be discussed in section 3.3.3 in detail, the MFM contrast also contains contributions from the sample topography. These can be removed to a large extent using methods as described in section 3.3.2. Fig. 2.5 (a) shows the MFM data used for the tip calibration. For the calibration of the tip, a model magnetization pattern of the sample must be extracted from the MFM data. For the MFM data shown in Fig. 2.5 this can be achieved by discriminating frequency shift values above and below an appropriately selected frequency level.

However, two issues are found to be critical: Firstly, the selection of the discrimination level, and secondly artifacts in the MFM data arising from the canting of the cantilever to the surface. The first can cause problems if small reversal domains near a domain walls exist and/or for larger domain sizes. The latter leads to small fields in the domain center (see Eqn. 2.9) and consequently to small differences between the frequency shift of the up/down domains. It may thus become very delicate if not impossible to define a discrimination level that correctly differentiate between the up/down domains.

These issues can be at least partially resolved by deconvolving the MFM data (Fig. 2.5

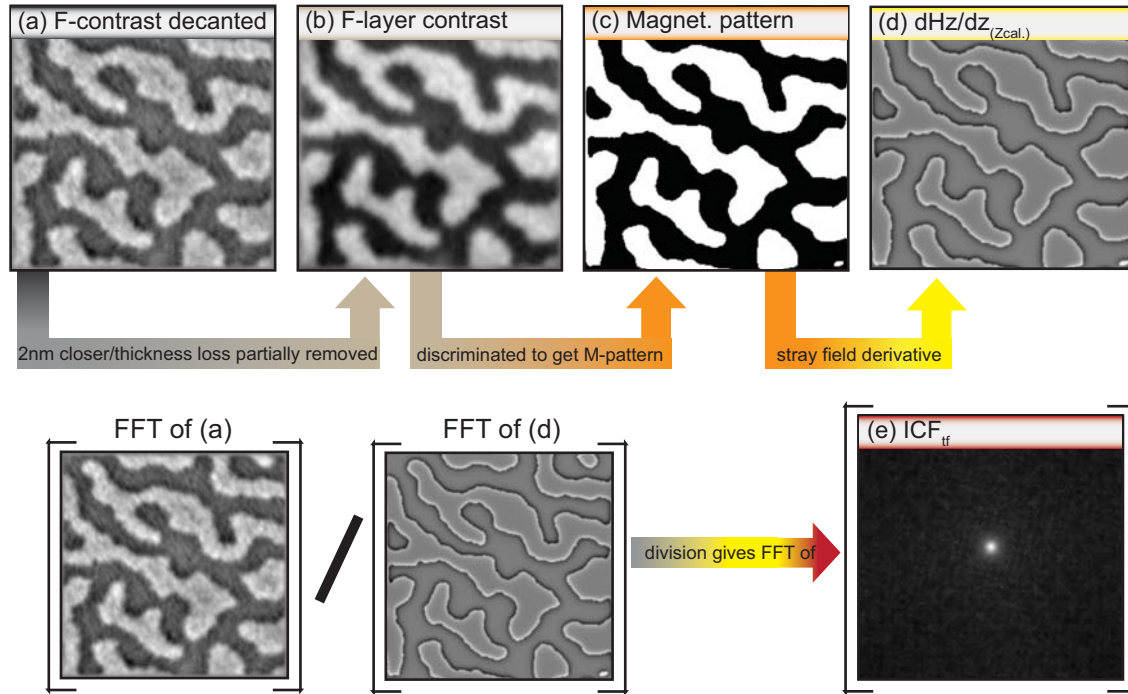


Figure 2.6: Procedure to create a Magnetization pattern and to calibrate an MFM tip: (a) $1\mu\text{m}\times 1\mu\text{m}$ MFM images acquired after zero-field cooling at 8.3 K. (b) is the calculation of the decanted image with the image is more closer and thickness loss partially removed. (c) shows the magnetization pattern which is determined by a discrimination process. (d) shows the stray field gradient is calculated from the magnetization pattern. (e) is the tip-transfer function which is calculated by dividing the FFT of the acquired image (a) by the FFT of the stray field gradient (d).

(d) and Fig. 2.6) from imaging artifacts caused by the cantilever canting (see Eqn. 2.6) and at least partially from the thickness loss factor (see Eqn. 2.9). The first leads to a pronounced asymmetry of the domain walls in the y -direction leading to the well visible under and overshoots at the white/black and black/white transitions (see Fig. 2.5 (b) compare to Fig. 2.5 (c)). The second lowers the frequency shift contrast in the center of the larger domains. The result of the decanting procedure is depicted in Figs. 2.5 (d-f) does not longer show these domain wall asymmetries. The partial removal of the thickness and distance loss factors leads to Fig. 2.6 (b), for which a discrimination level can be determined that correctly distinguishes the up from the down domains (Fig. 2.6 (c)). Note that this procedure assumes the magnetization to be uniform through the thickness of the sample and either $\pm M_{VSM}$ in the up/down domains, when M_{VSM} is the average M -value measured by VSM, ($M = 555564.0$ A/m). Once a model magnetization pattern (Fig. 2.6 (c)) has been determined, the stray field derivative pattern is calculated by Eqn. 2.9, at a tip-sample distance z_{calc} . The distance $z_{calc} := z_0 + z_{cap} - \Delta z = 8.3$ nm, where $z_0 = 9$ nm is the measured tip-surface distance (see section 2.4), $z_{cap} = 1.3$ nm is the thickness of the capping layer and $\Delta z = 2$ nm is an extra distance introduced for numerical reasons. The thickness of the F-layer is 5 nm (see Fig. 3.8).

Using the Fourier transforms of the acquired MFM data (Fig. 2.6 (a)) and the stray field

derivative data (Fig. 2.6 (d)), the instrument calibration function multiplied by a $\Delta z = 2$ nm distance loss factor, $\text{ICF}(\mathbf{k}, \Delta z)$, is calculated by

$$\begin{aligned} \text{ICF}(\mathbf{k}, \Delta z) &:= \text{ICF}(\mathbf{k}) \cdot \exp(-k\Delta z) \\ &= -\mu_0 \frac{f_0}{2c_L} \cdot q_{tip}^*(\mathbf{k}) \cdot \exp(-k\Delta z) \cdot [\text{LCF}(\mathbf{k})]^2 \\ &= \frac{\text{FFT}(\text{data of Fig. 2.6(a)})}{\text{FFT}(\text{data of Fig. 2.6(d)})}. \end{aligned} \quad (2.12)$$

Note that the reversed Fourier transform of $\text{ICF}(\mathbf{k}, \Delta z)$ is the stray field of the tip in a plane located 2 nm below the tip apex [44] multiplied by $-\mu_0 \frac{f_0}{2c_L}$ (Fig. 2.6 (e)). Further note that the “extra distance” $\Delta z = 2$ nm is introduced to reduce the sharpness of the direct space image of the tip-transfer function (Fig. 2.6 (e)) such that it can be well represented by the limited number of available pixels.

To test the validity or the numeric precision of the transfer-function $\text{ICF}(\mathbf{k}, \Delta z)$, MFM image (Fig. 2.7(c)) is simulated from the $\frac{\partial}{\partial z} H_z(\mathbf{k}, z_{calc})$ -pattern shown in Fig. 2.6 (c). The simulated F-layer image (Fig. 2.7(c)) is then subtracted from the initial F-layer data (Fig. 2.7 (e)). The resulting difference image (Fig. 2.7 (f)) shows a contrast only of $\pm 1 \cdot 10^{-6}$ Hz. This proves the ex-

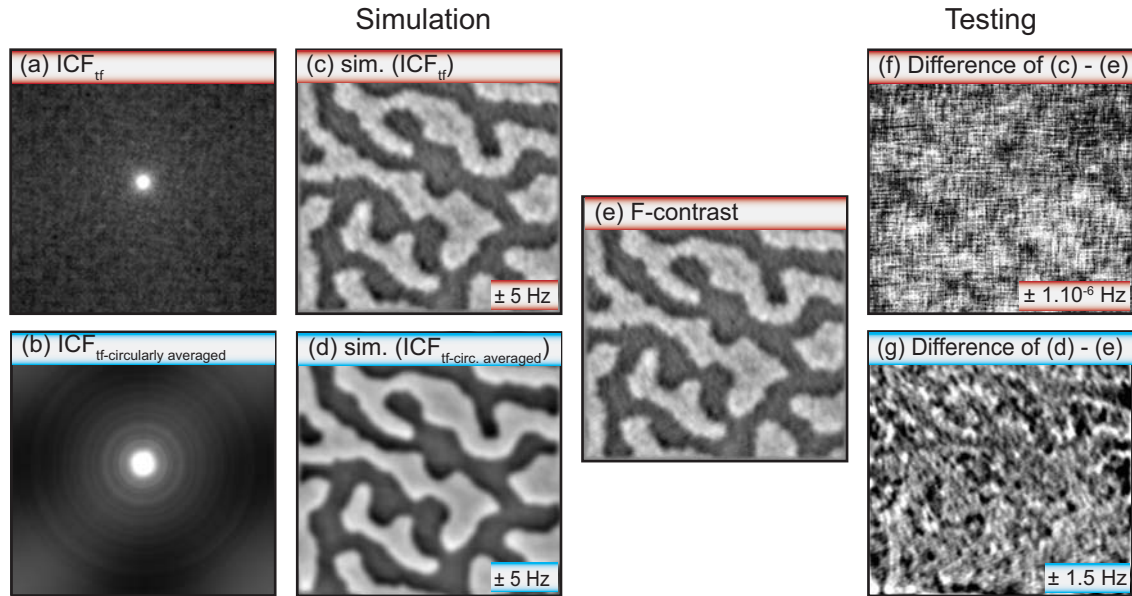


Figure 2.7: (a) ICF_{tf} , (b) the $\text{ICF}_{\text{tf-circ-averaged}}$. Test of the calibration functions: (c), and (d) are the simulated images by using ICF_{tf} and $\text{ICF}_{\text{tf-circ-averaged}}$, respectively. (e) is $1\mu\text{m} \times 1\mu\text{m}$ MFM images acquired after zero-field cooling at 8.3 K. (f) and (g) are the differences of the simulated images from the acquired image, (e).

cellent numerical quality of the transfer function. However, note the granularity of the F-contrast (Fig. 2.7 (e)). This granularity arises from remainders of the topography-induced contrast contributions (see section 3.3.3) and possibly from local variations of the F-layer thickness and local magnetization. This granularity is not contained in the model magnetization pattern (Fig. 2.6 (c)), therefore also not in the stray field derivative image Fig. 2.6 (d) calculated from it.

Hence the granularity must appear in a different form in the transfer function that is calculated from the granular F-contrast image (Fig. 2.7 (e)) and the smooth (non-granular) $\frac{dHz}{dz}$ -image (Fig. 2.6 (d)). Although this granularity-affected transfer function Fig. 2.7 (a) perfectly re-generates a granular F contrast image from the smooth $\frac{dHz}{dz}$ -image, the granularity in the transfer function is an artifact arising from the specific procedure used to calculate the transfer function.

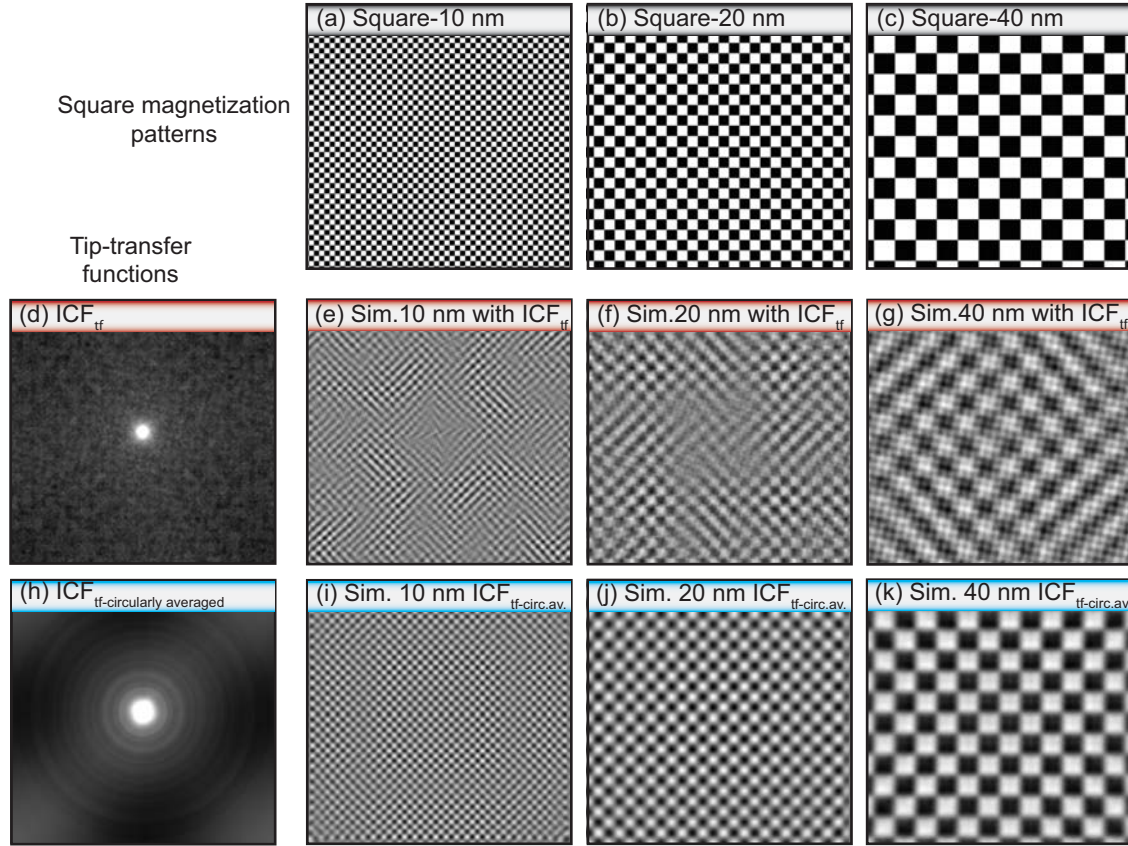


Figure 2.8: Simulation of the different sized patterns (a), (b), and (c) are the square pattern with a 10, 20 and 40 nm size. (e), (f), and (g) are the simulations of the pattern by using the non-averaged tip transfer function, ICF_{tf} (Fig. 2.8 (d)). Also (i), (j), and (k) are the simulations of the square patterns by using circularly averaged tip-transfer function, $ICF_{tf-circ.averaged}$, (Fig. 2.8 (h)).

For a later deconvolution of the magnetic moment distribution from measured MFM frequency shift data, the signal-to-noise ratio of the transfer function needs to be further improved and artifacts need to be reduced. This can be achieved by calculating the circular average in Fourier space. The real-space representation of the averaged transfer function is shown in Fig. 2.7 (b). The granularity is greatly reduced. A test of this circularly averaged transfer function gives a simulated F-contrast image with greatly reduced granularity (compare Fig. 2.7 (d) with Fig. 2.7 (c)).

The difference between the initial F-contrast image (Fig. 2.7 (e)) and the simulated image (Fig. 2.7 (d)) with the circularly averaged transfer function (Fig. 2.7 (b)) is shown in Fig. 2.7 (g).

The contrast of Fig. 2.7 (g) is higher than that of the difference image obtained with the non-averaged transfer function. One should however refrain from concluding that the non-averaged transfer function is better. The non-averaged function only contains artifacts that arise from the chosen, smooth model magnetization pattern. Hence a simulation performed with this transfer function that is based on the smooth model magnetization pattern will match the measured Δf -data better. The circular averaging process reduces the artifacts in the transfer function. A simulation performed with this average transfer function based on the smooth magnetization pattern will then however not contain any “magnetic roughness” and hence to a difference image of larger contrast.

A simple test to evaluate the quality of a transfer function is the application to stray fields of a periodic up/down magnetization test patterns, as depicted in Fig. 2.8 (a)-(c). Simulations obtained with the non average transfer function $ICF(k, \Delta z)$ (ICF_{tf} , Fig. 2.8 (d)) clearly show a waviness of the simulated MFM image (Fig. 2.8 (e)-(g)) that can not be real as known from experimental experience with MFM images of periodic patterns. Then artifacts clearly arise from the granularity of the transfer function. Simulations performed with circularly averaged transfer function (Fig. 2.8 (h)) do not show these artifacts (Fig. 2.8 (i)-(k)). This is a strong indication that circular averaging improves the signal-to-noise ratio of the transfer function and reduces the artifacts arising from the specific calibration procedure applied in here.

2.5 Summary

Magnetic force microscopy measures a frequency shift pattern related to the stray field emanating from all magnetic moment distributions inside the sample. Once the response of the MFM tip has been calibrated, the stray field at the surface of the sample can be deconvolved from the measured MFM frequency shift data. Although the relation between stray field and magnetic moment distribution inside the sample is not unique, information of the latter can be extracted from the stray field pattern using additional information on the magnetic sample state.

Chapter 3

Quantitative Assessment of Exchange Bias Systems

3.1 Types of Magnetic Moment in Exchange-biased Samples

It is generally accepted that exchange bias (EB) implies the presence of pinned uncompensated moments (m_{AF}^{p-uc}) in the antiferromagnet (AF) or at its interface with the ferromagnet (F). However, the coupling occurring at the interface between the F and AF, the mechanism for the generation of pinned uncompensated moments and their role for the EB-effect are not fully understood. In a most simplistic view (Fig. 3.1), the AF consist of a set of two antiferromagnetically coupled sub-lattices each of them consisting of ferromagnetically aligned moments, m_{AF} . For an AF without defects and an equal number of sub-lattices, the sum of all moments vanishes, i.e. there is no net magnetic moment in a perfect AF. Assuming that the interface between the F and AF was flat and chemically sharp and an orientation parallel to the AF magnetic sub-lattices, only one of them would couple to the F magnetic moments (coupling of m_{AF} with m_F in Fig. 3.1). Then, the interfacial plane of the AF would be fully uncompensated. Such an ideal interface would generate a strong unidirectional anisotropy of the F-layer, leading to a preference of one magnetization orientation of the F-layer, i.e. an EB-effect. However, such a fully uncompensated interface would generate an EB field that is about 100 stronger than typically observed values [32] (see also discussion on the models in Chapter 1). This, and the experimental fact that an EB-effect is also observed on nominally compensated interfaces prove that a simplistic model as depicted in Fig. 3.1 fails to describe the most experimental observations. A more realistic cartoon is shown in Fig. 3.2 (which is still neglecting that the magnetic moments may not be collinear). In the most general case, the F and AF moments (m_F and m_{AF}) may arise from different elements A and B of the F and AF, respectively (Fig. 3.2). Then element-specific magnetometry and microscopy methods can -in principle- separately address these magnetic moments and map their location in the sample. However, in EB systems (for example in the CoO(AF)/CoPt-multilayer (F), the magnetic moment of the F and AF arises from the same magnetic element (Co) albeit in a different oxidation state. Then the distinction of the AF and F moments becomes more delicate. Apart from the AF sub-lattice moments that compensate each other (labelled as (a) in Fig. 3.2), defects will exist that lead to pinned and rotating uncompensated moments m_{AF}^{p-uc} and m_{AF}^{r-uc} , respectively inside the AF (labelled as (b) Fig. 3.2). These uncompensated moments inside the AF may become pinned to one of

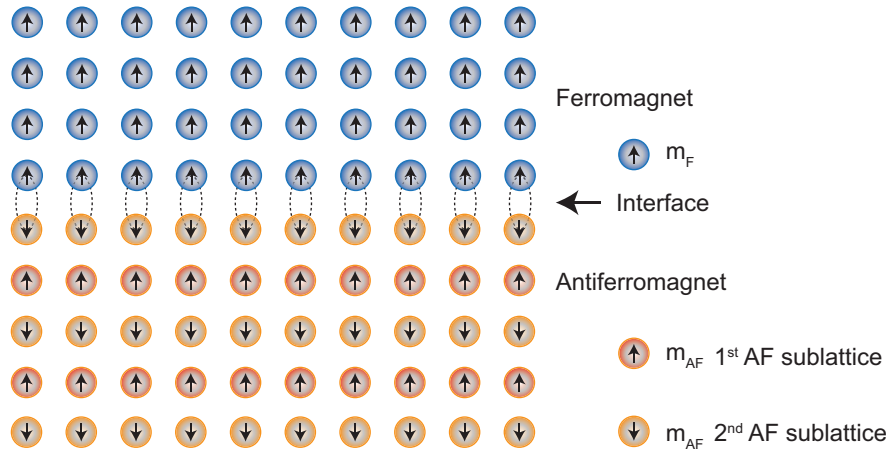


Figure 3.1: Schematic diagram showing the F/AF moment directions and distributions at the ideal F/AF interface. The m_F describe the distribution of magnetic moments, in ferromagnetic layer that are aligned co-linear and parallel. At the interface they coupled to the sub-lattice of AF, m_{AF} (yellow moments). All the sub-lattice of AF (yellow and orange moments of AF) are also aligned co-linear but antiparallel to have a zero net magnetic moment. The F and AF-layers have an atomically smooth interface, so that the interfacial AF moment plane is a fully uncompensated. Such an ideal interface would then generate a strong unidirectional anisotropy of the F-layer and leads to an EB-effect.

the AF sub-lattices m_{AF}^{p-uc} (pinned magnetic moments), or may remain in a paramagnetic state (m_{AF}^{r-uc}), i.e. follow the orientation of the applied field (see domain state and spin glass models in sections 1.5 and 1.6, respectively). In the latter case, such a magnetic moment give rise to a thermoremanent magnetization observed in AF's but will not contribute to the EB-effect [18, 19], but enhance the coercivity of the F-layer. Assuming a rough and chemically intermixed F/AF interface (see spin glass model in section 1.6), magnetic moments of the ferromagnetic element (m_F) can be located in the AF (denoted with (c) in Fig. 3.2), or moments of AF (m_{AF}) can occur inside the F (denoted with (d) in Fig. 3.2). For the former case, the F moment $m_F^{p,r-uc}$ may act as a magnetic defect inside the AF leading to an uncompensated moment inside the AF and playing a role similar to an uncompensated AF moment, $m_{AF}^{p,r-uc}$.

Uncompensated AF moments at or near the interface that couple to the F moments can contribute to the EB-effect or/and increase the coercive field of the F. In the former case the uncompensated AF moments m_{AF}^{p-uc} must remain pinned to one of the AF sub-lattice (labelled as (e) in Fig. 3.2). Note that depending on the F/AF system, this coupling between pinned AF moments (m_{AF}^{p-uc}) and the F moments can be parallel (ferromagnetic) or antiparallel (antiferromagnetic), or possibly even non-collinear. For the multilayer CoPt ferromagnet and CoO antiferromagnet studied here (as well as for the MnIr antiferromagnet studied before [13, 19]), we find an antiparallel coupling. For many years, our results and interpretation concerning this antiferromagnetic coupling were controversial discussed [14, 16]. Recently, more refined neutron [45] and X-ray reflectometry [20] experiments confirmed our results, leading a wider acceptance of our work. If the coupling of the $m_{AF}^{p,r-uc}$ to the F moment is larger than that with AF sub-lattice, the uncompensated AF moments will rotate with the F moments and con-

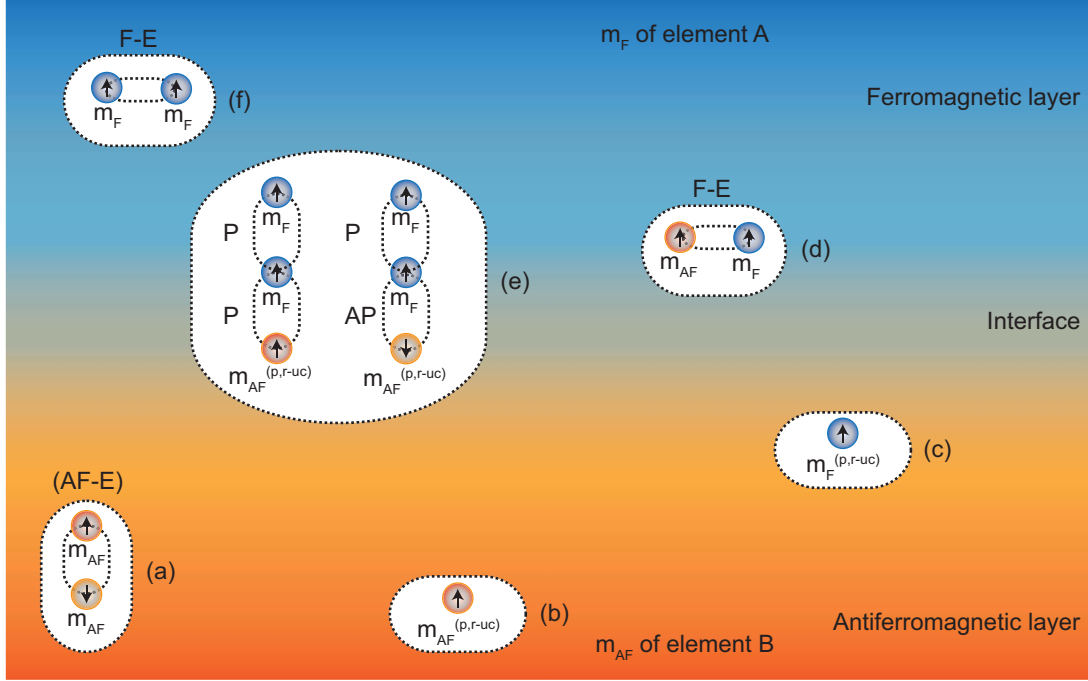


Figure 3.2: Schematic diagram of the sample showing the magnetic moments directions and distributions at the realistic F/AF interface. There is an interface region due the atomically rough surface and the chemically inter-mixed F/AF-layer. For simplicity all the magnetic moments aligned co-linear. Bubbles show the different possibility of the interaction that can be occurred at the interface or in F/AF. Magnetic moments of F labelled as $m_F^{p,r-uc}$ and that of AF for each sub-lattice as $m_{AF}^{p,r-uc}$. Here, “uc” used for uncompensated, “p” for pinned and “r” for rotating type of magnetic moments. When the magnetic moments of two AF sub-lattices inside AF couples as depicted in (a) that gives no net magnetization. Defects existed inside AF (b) leads to net magnetization that may pinned to one of the AF sub-lattice or in a paramagnetic state. There is an intermixing of F and AF magnetic moments near or at the interface as depicted in (c) and (d). Former case may also behave as a defective AF as in (b) situation. (e) shows the possibility of parallel or antiparallel coupling of F magnetic moments with the AF ones that may be pinned or rotating types. If AF magnetic moments pinned to AF sub-lattice, this will contribute to EB-effect, If not, for rotating type of spins will follow the magnetization of F magnetic moments and leads to increase of the coercivity of F-layer. (f) shows the interaction of the F magnetic moments inside F-layer with intrinsic ferromagnetic exchange coupling.

tribute predominantly to the coercivity and to a smaller extent to the EB-effect, (unidirectional anisotropy). In addition, inside the F, a strong ferromagnetic exchange coupling exists (labelled as (f) in Fig. 3.2).

Note that the above description and Fig. 3.2 is to categorize different types of magnetic moments that can exist in an F/AF system, and to point out their role for the EB-effect, but does not attempt to explain the mechanisms by which these moments and a net unidirectionality arises. For the latter various models such as Meiklejohn and Bean model [7, 8, 21], Mauri Model

[23], Malozemoff Random Field Model [26, 27, 28], Takano model [17, 18], Domain State Model [31], and Spin Glass Model [32] etc. have been proposed (see Chapter 1). The most widely accepted models to explain the EB-effect are the domain state and the spin glass model. An elaborated interpretation of our experimental data in this chapter and Chapter 4 will reveal that most experimental aspects can be explained by a suitable combination of these two models.

3.2 Overview on Neutron and X-ray Dichroism Method

In the past decade, many different experimental techniques have been used or were developed to measure the density and location of the different types of uncompensated magnetic moments and study their role for the EB-effect. Reflectometry experiments using polarized neutrons [46, 45] or circularly polarized x rays [47, 48] as probes have been used to access these uncompensated magnetic moment subsystems and to map out their thickness distribution.

Spin polarized neutrons are the ideal probe to study the orientation and size of atomic magnetic moments in single crystals. Magnetization depth profile can be studied as a function of the applied field in a reflectometry set-up. Then the measured data must be fitted to a proposed model depth profiles.

The dichroic absorption of circularly/linearly polarized x-rays (XMCD, XMLD) allows element-specific magnetometry of F and AF magnetic moments [11]. Magnetic depth profiles can be deduced from fitting experimental XMCD reflectometry data to proposed model structures. X-ray based experiments require in addition specifying magneto-optical constants of the atomic species carrying the moment in the AF [48] to determine relative orientation of the uncompensated magnetic moment of the various AF subsystems and the F moments. Recent results have also stressed the influence on the x-ray magnetic linear dichroism (XMLD) signals of the orientation of AF moments relative to the crystallographic axis [49, 50]. Again the application of a magnetic field is possible for x-ray in/x-ray out type of experiments. Note that the application of stronger field is no longer possible if the x-ray absorption is detected by the emission of secondary electrons and accordingly this hinders a direct distinction between pinned and rotating type of uncompensated magnetic moments. In fact, only a small part of the net moment induced locally by the F in the AF consists of pinned uncompensated moments [51], which are difficult to isolate from the rest with present-day reflectometry techniques sensitivities [52]. Note also that XMD methods, that measure the absorption-generated secondary electrons (PEEM), are very surface sensitive technique. The top layer must be thin enough for the photoelectrons (generated by core excitations) to reach the detectors, so the bulk information for the sample is hardly obtained in this method.

XMCD/LD methods can also be used for imaging magnetic structures. Ohldag *et al.* [11] have used an XMCD/LD PEEM to image the colinear alignment of F domains with AF domains, in a Co(F)/NiO(AF) exchange bias thin film samples. In addition pinned magnetic moments have been found to exist in a chemically mixed Co-Ni-alloy oxide interfacial layer. Eimuller *et al.* [20] and Offi *et al.* [52] also have revealed the induced ferromagnetic moments at the F-AF interface by PEEM using XMCD. Most authors image F moments and some of uncompensated moments of AF, most of these seem to rotate with the F. The amount of pinned uncompensated moments can only be roughly estimated. Blackburn *et al.* [51] have identified a thin (0.5 nm) layer containing uncompensated Co magnetization at the interface of a polycrystalline (F) - CoO (AF) by using x-ray resonant reflectometry. He found majority of the magnetization follows the

external field and estimated $\approx 10\%$ of the magnetization in this interfacial layer is pinned and antiparallel to the cooling field used when the biasing the sample.

To date, PEEM microscopes have not attained a lateral resolution on the length scale of grain sizes of typical polycrystalline AF materials, used in technological applications. In contrast to PEEM, MFM can be used even in strong magnetic fields of several Teslas, can easily be applied at various temperatures, and can obtain a higher lateral resolution down to tens of nanometers or better. This allows to follow the evolution of F-domains in applied fields. However, MFM does not directly probe the magnetization of the sample; instead MFM maps a signal related to the magnetic stray field emanating from the sample independent from the sources of the field. So it is thus not element-specific and can not directly distinguish between different sources of the stray field. However, applied uniform fields do not give rise to contrast. Likewise, no contrast is expected for a F film of uniform thickness and magnetization, or close to the center very wide (vis-à-vis the film thickness) domains, because the stray field is negligible. Such films would be “transparent” to the MFM. Hence, the distribution of uncompensated magnetic moments located at (even) hidden layers can be accessible by high-resolution quantitative MFM and the interpretation of the data is also possible after careful analysis.

3.3 How to Image p-UCS by MFM

As indicated in Fig. 3.2, uncompensated magnetic moments of different nature exist inside the F and AF. Their density and spatial distribution need to be accessed, and their roles for the EB effect and mechanisms leading to a unidirectional anisotropy need to be understood. A key instrument in our lab is a home-built low temperature ultra-high vacuum magnetic force microscope (LT-MFM). MFM maps the stray fields emanating from the surface of a magnetic sample with high spatial resolution. The magnetic stray fields are generated by a divergence of the distribution of the magnetic moments located inside the F, AF or at the F/AF interface. Magnetic fields can penetrate through non-magnetic (and magnetic) layers. MFM can therefore access magnetic moment distributions inside of a sample but cannot a priori distinguish different sources of the field.

3.3.1 First MFM experiments on Exchange Biased Samples

The first MFM experiments on exchange biased samples were performed by our research group by Kappenberger *et al.* [13]. In these experiments, a pattern of pinned uncompensated moments imprinted into the AF by the F-domain pattern of the adjacent F-layer were imaged. A $\text{Co}([\text{Co}(0.4\text{nm})/\text{Pt}(0.7\text{nm})]_4\text{Co}(0.6\text{nm})\text{CoO}(1\text{nm}))_{10}$ multilayer F/AF sample with multiple F/AF interfaces and a sufficiently large F-thickness was fabricated. The F thickness of 44 nm lead to a F-stripe domain pattern with an average domain width 83 nm after having applied a demagnetizing oscillating in-plane magnetic field. The sample was zero-field cooled from room temperature to 7.5 K. Fig. 3.3 shows the MFM frequency shift (Δf) contrast generated by the stray field of F-stripe domain pattern ($\Delta f_F(D_F, M_F)$) and that arising from the imprinted uncompensated magnetic moments pattern ($\Delta f_{AF}(D_{AF}, m_{AF}^{p,r-uc})$). Note that Δf_F and Δf_{AF} stand for frequency shifts caused by stray fields emanating from the F and AF layer, respectively. D_F and D_{AF} stand for the dependence of the Δf -signal on the domain state of the F with a magnetization M_F , and the imprinted pattern of uncompensated moments in the AF

m_{AF} . The indices “ p ” and “ r ” distinguish between the pinned and rotating uncompensated moments. After zero-field cooling the strong observed AF-contrast is dominated by the contribution of the F-domains, i.e. $\Delta f_{zero-field} \approx \Delta f_F(D_F, M_F)$. In the work of Kappenberger *et al.* [13], saturating fields were applied to wipe out the F-domains. A flat F-layer of constant thickness and homogeneous magnetization does no longer generate a stray field. The F-layer becomes invisible or transparent for the MFM. Any stray field pattern then detected by the MFM arises from other sources. After saturation of the F-layer(s) in a 850 mT field (Fig. 3.3

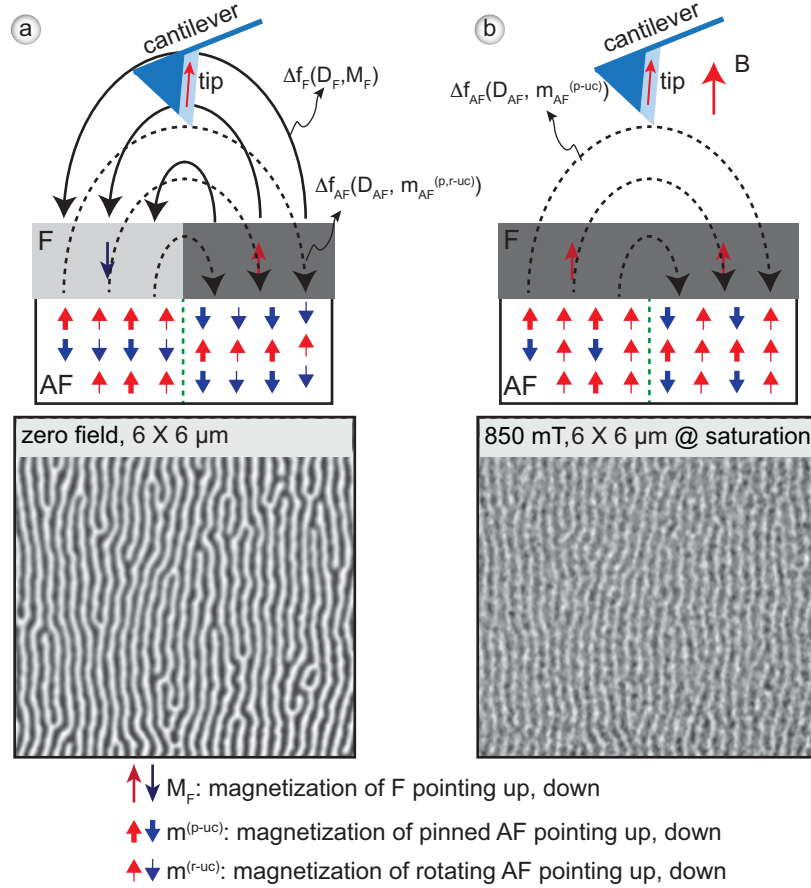


Figure 3.3: Measurement of the contrast arising from the hidden layers, (a) MFM image of the F-stripe domain pattern after zero-field cooling and (b) after 850 mT applied field to saturate the F-layer magnetization giving the contrast only due to the pinned uncompensated moments of AF, $\Delta f_{AF}(D_{AF}, m_{AF}^{p-uc})$.

(b)), a granular stripe domain pattern with a 30 times weaker contrast remained visible. This pattern that persisted even in fields up to 7 T was attributed to the imprinted pattern of pinned uncompensated moment of AF ($\Delta f_{AF}(D_{AF}, m_{AF}^{p-uc})$). The contrast of the pattern visible after saturation is inverted compared to the initial F-domain image obtained after zero field cooling. The field was applied parallel to the tip magnetization. The observed contrast inversion is thus caused by local antiparallel alignment of the uncompensated moments of AF and the moments

of F domain pattern.

In conclusion the separation of the two sources for magnetic stray field was possible by saturating the magnetization of the F-layer and thereby suppressing its contribution to the measured MFM contrast.

3.3.2 Separation of Van der Waal's and Magnetic Forces

As discussed in Chapter 2 all our MFM data are acquired in an operation mode that scans the tip parallel to the average sample slope. A reduction of the average tip-sample distance allows the detection of the higher spatial frequency components of the stray field, that decay more rapidly with increasing distance from the surface (this is mathematically described by the distance loss factor in Eqn. 2.9). The best resolution is obtained if the average tip-sample distance is reduced as much as possible but contact with the higher features on the sample does not yet occur. MFM imaging of such small average tip-sample distances will however be affected by an increased topography-induced variation of the local van der Waals force. If a sample generates only a weak magnetic stray field, this topography induced contrast can even dominate the magnetic contrast.

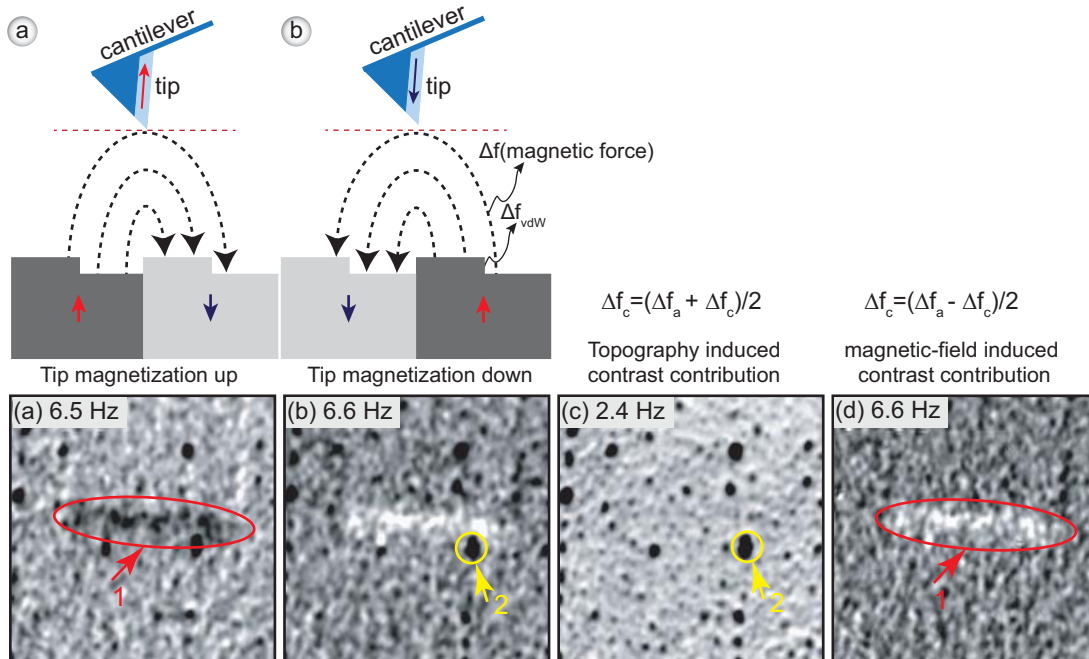


Figure 3.4: Separation of Van der Waal's and Magnetic Forces: (a) and (b) shows the MFM contrast taken with opposite tip magnetization at the area of the sample with the same tip-sample surface distance. (c) one half of the sum of the MFM images in (b) and (c) gives the topography-induced contrast. (d) one half of the difference of the MFM images in (b) and (c) gives the magnetic field generated contrast.

Kappenberger *at al.* [12] developed two methods to separate magnetic and topographical contrast contributions. Here only one method, that will later be applied in a modified form

is discussed: the sample is imaged twice with opposite magnetization of the tip but otherwise identical operation parameters. An example of the resulting images is shown in Fig. 3.4 (a) and (b). The reversal of the tip magnetization also reverses the part of the images contrast that arises from the magnetic field (see the area 1 in Fig. 3.4), but not the topography-induced contrast contribution (see the feature at position 2). Note that in our case we use low magnetic moment tips and map a high-anisotropy recording material. The tip stray field then does not modify the magnetization of the sample as was the case in the experiments published by Foss *et al.* [53].

In our case, one half of the sum of the data shown in Fig. 3.4 (a) and (b) reflects the contrast contribution of the topography Fig. 3.4 (c), while one half of the difference shows the magnetic field generated signal only in Fig. 3.4 (d).

Note that similar to the van der Waals forces, electrostatic forces would lead to a topography-induced contribution to the MFM contrast. In our experiments, this electrostatic contribution is minimized by a compensation of the contact potential before MFM imaging is performed.

3.3.3 Design of EB-sample for high-resolution MFM imaging

High resolution MFM imaging requires a small tip-sample distance during MFM data acquisition. In the case of EB-samples, the distance between the tip and the location of the imprinted pinned uncompensated moments must be minimized. This requires the F/AF or AF/F interface to be close to the surface of the sample. Thus either the F (in case of the F/AF sample) or the AF (for the AF/F sample) must be as thin as possible. In our case we use CoO as an AF-layer. The CoO is obtained by oxidizing a 1 nm thick Co layer at ambient conditions. Thus top of the layer will be fully oxidized but the lower strata of the CoO layer may suffer from incomplete oxidation. In order to couple the F-layer to a fully oxidized CoO layer, we deposited the F-layer onto the AF-layer. Hence, the F-layer thickness must remain small.

The sample structure is $\text{SiO}_2/\text{Pt}(5\text{nm})/\text{Co}_{0.8}\text{Cr}_{0.2}\text{O}(1.5\text{nm})/[\text{Co}(0.3\text{nm})/\text{Pt}(0.7\text{nm})]_4\text{Co}(0.3\text{nm})/\text{Pt}(2\text{nm})$, i.e. an F/AF bilayer. Note that the Cr was co-deposited with the Co to enhance the EB effect (see chapter 4). The structure of the sample is as depicted schematically in Fig. 3.5 (a). The ferromagnetic CoPt-multilayer exhibits a perpendicular magnetic anisotropy. Vibrating sample magnetometry (VSM) results revealed coercive fields of $\mu_0 H_c^+ = +296.3\text{ mT}$, $\mu_0 H_c^- = -592.7\text{ mT}$ and exchange bias-field $\mu_0 H_{eb} = -296.4\text{ mT}$ after cooling the sample to 8.3 K in a 1 T field. Microscopically, the as grown domain structure of the sample was studied by MFM after zero-field cooling the sample to 8.3 K (well below the Néel temperature of the sample, $T_N = 291\text{ K}$) (Fig. 3.5 (b)). In image Fig. 3.5 (b) two down bubble domains with a down-magnetization are visible (marked by blue \otimes) are apparent inside a larger up domain (marked by red \odot). The large domain size and the small F-layer thickness result in a strong stray field gradient at the domain wall but only a weak stray field in the domain center. Accordingly there is a pronounced black/white contrast only near the domain walls, i.e., *domain wall contrast*. Inside the domains a granular contrast and some isolated darker areas are visible (yellow circles in Fig. 3.5 (b), also in Fig. 3.6 (a-k)). The granularity and the darker areas mainly stem from the topography of the sample, which gives rise to variations in the van der Waals force. Then granular features remain visible after the F layer has been saturated (Fig. 3.6 (c) and (e)).

The F domains imprint a corresponding pattern of uncompensated moments into the AF [13] (schematically shown in Fig. 3.6 (b)). A part of these denoted with m_{AF}^{r-uc} rotate with the local F-magnetization in an applied field, while another remains pinned (denoted by m_{AF}^{p-uc}). The MFM

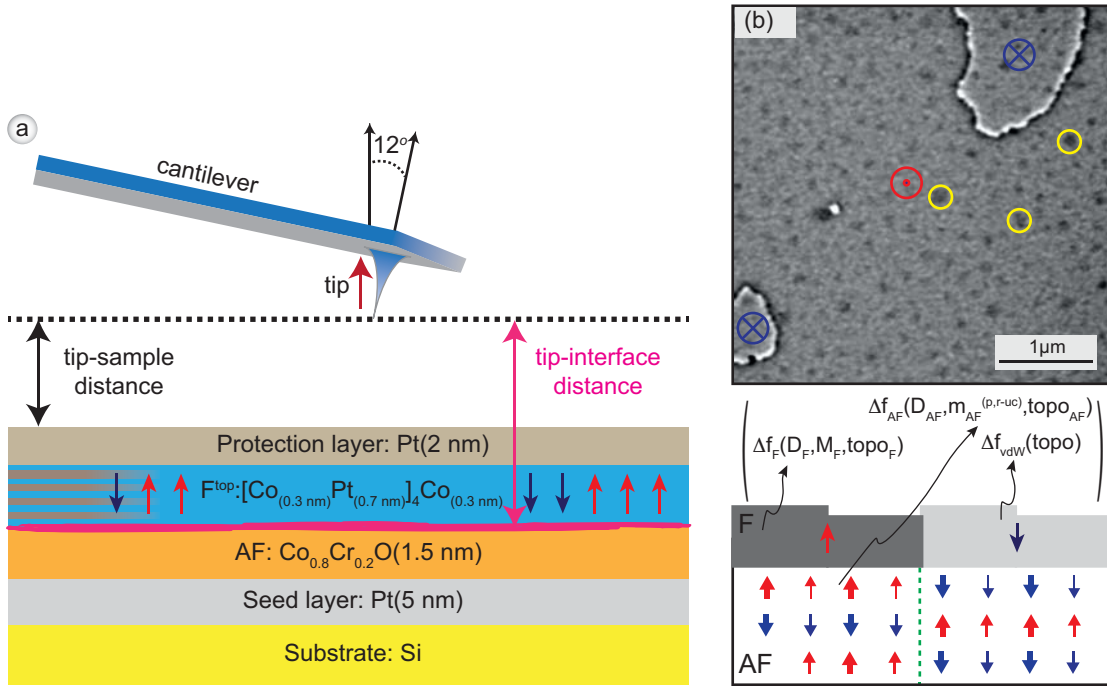


Figure 3.5: Schematic structure of the sample to keep the measurement surface closer to the sample surface so that the contrast due to solely pinned uncompensated AF moments can be visible by our MFM. Single F layer is Pt(5nm)/AF/F/Pt(2nm) with AF as 1.5 nm $\text{Co}_{0.8}\text{Cr}_{0.2}\text{O}$, F as 4 repeated $[\text{Co}(0.3\text{nm})/\text{Pt}(0.7\text{nm})]_4/\text{Co}(0.3\text{nm})$. (b) MFM image of the single F layer sample with micron-sized domains. The contrast of (b) is generated by the F layer ($\Delta f_F(D_F, M_F, \text{topo}_F)$), pinned and rotating uncompensated moments of AF layer ($\Delta f_{AF}(D_{AF}, m_{AF}^{r-uc}, \text{topo}_{AF})$) and the topography-induced vdW force ($\Delta f_{vdW}(\text{topo})$).

contrast in Fig. 3.6 (a) is given by $\Delta f = \Delta f_F(D_F, M_F, \text{topo}_F) + \Delta f_{AF}(D_{AF}, m_{AF}^{r-uc}, \text{topo}_{AF}) + \Delta f_{AF}(D_{AF}, m_{AF}^{p-uc}, \text{topo}_{AF}) + \Delta f_{vdW}(\text{topo})$ where the first term describes the contrast generated by the F-layer, the second and the third terms describe the contrast due to the rotating and pinned magnetic moments of the AF, and the last term describes the van der Waals-induced contrast arising from the topography of the sample. Note that the contrast generated by F-layer depends on the geometry of the F-domains D_F , and the magnetization M_F , but also on variations of the F-layer thickness and roughness (D_F, topo_F). Note that also a spatial variation of M_F inside the domains would generate a contrast. The latter can however be neglected as shown by a simulation presented in section 3.3.5. Also by simulations, we will find that the contrast contributions mediated by the magnetic field arising from the spatial variations of F-layer thickness and roughness (symbolically denoted by D_F, topo_F) are dominated by the topography-induced variation of the van der Waals forces ($\Delta f_{vdW}(\text{topo})$).

If a field of +1 T is applied, the F-layer is saturated Fig. 3.6 (d). Note that a positive field is applied parallel to the tip magnetization, such that the tip magnetization remains in its saturated state. The observed MFM contrast (Fig. 3.6 (c)) is given by $\Delta f = \Delta f_F^{+1T}(\text{Sat}_F, M_F, \text{topo}_F) + \Delta f_{AF}^{+1T}(\text{Sat}_{AF}, m_{AF}^{r-uc}, \text{topo}_{AF}) + \Delta f_{AF}^{+1T}(D_{AF}, m_{AF}^{p-uc}, \text{topo}_{AF}) + \Delta f_{vdW}(\text{topo})$ where the first

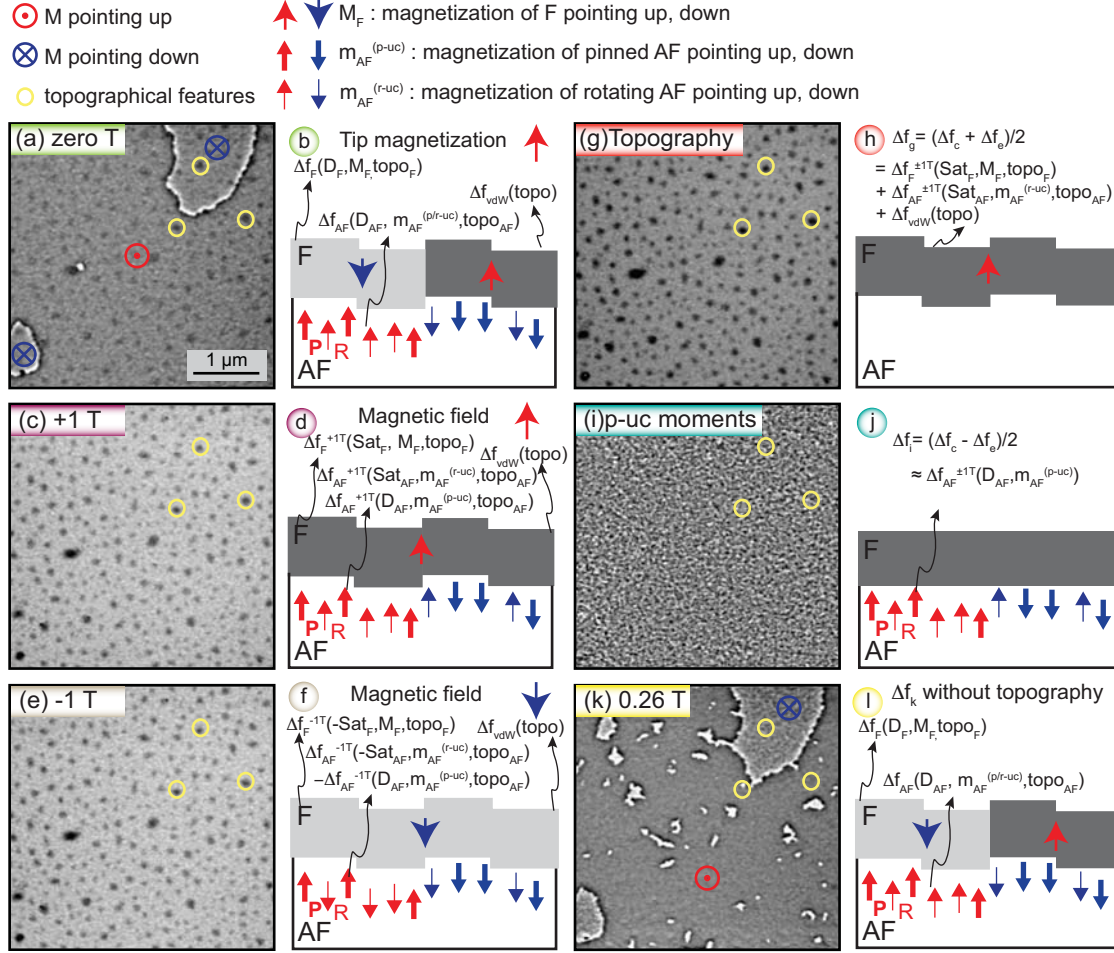


Figure 3.6: (a) after zero-field cooling to 8.3 K; (b) MFM contrast is generated by the F layer, pinned and rotating uncompensated moments of AF layer, and the topography-induced vdW force. Note that the contrast generated by F-layer depends on the geometry of the F-domains D_F . Yellow circles in (a), (c), (e), (g), (i) and (k) indicate some topographical features. (c) saturation of the F layer in 1 T, field applied parallel to tip magnetization; (d) Note that now the contrast arises from the saturated F-layer, and notice further that the frequency shift generated by the rotating moments changed, from $\Delta f_{AF}(D_{AF}, m_{AF}^{r-uc}, topo_{AF})$ at 0 mT to $\Delta f_{AF}^{+1T}(Sat_{AF}, m_{AF}^{r-uc}, topo_{AF})$ in a field of 1 T. The distribution of the pinned AF moments (m_{AF}^{p-uc}) does not change with the applied field. (e) saturation in -1 T, field applied antiparallel to tip magnetization; (f) Note that the contrast generated by the imprinted pinned uncompensated AF moments now reversed, because the magnetization of the tip has reversed. (g) is semi sum of the MFM image taken in +1 T and -1 T; (h) shows the contrast contribution of the MFM image (g). (i) is semi difference of the MFM image taken in +1 T and -1 T; (j) the contrast generated by the pinned AF moments only. (k) recovery of (a) at +0.26 T after (e).

term arises from the saturated F-layer, the second and third terms stem from the AF uncompensated moments and the last term from the topo-induced vdW force. Note that the latter

does not depend on the magnetic state of the sample. Further, note that the uncompensated AF moments that rotate with the applied field do no longer reflect the imprinted domain structure. Instead these m_{AF}^{r-uc} will be distributed rather homogeneously, possibly with density variations on the scale of AF grains. Note that the frequency shift generated by the rotating moments changed, from $\Delta f_{AF}(D_{AF}, m_{AF}^{r-uc}, topo_{AF})$ at 0 mT to $\Delta f_{AF}^{+1T}(Sat_{AF}, m_{AF}^{r-uc}, topo_{AF})$ in a field of 1 T. By definition the distribution of the pinned AF moments (m_{AF}^{p-uc}) does not change with the applied field [12]. Consequently the frequency shift term containing the pinned AF moments, m_{AF}^{p-uc} , the third term does not change.

From this and from our earlier work [12] we would expect that the imprinted pattern of uncompensated moments would become visible in the MFM image acquired in the MFM image acquired in 1 T with a saturated F-layer. However Fig. 3.6 (c) does not show the imprinted pattern of pinned uncompensated AF moments. The term $\Delta f_{AF}^{+1T}(D_{AF}, m_{AF}^{p-uc}, topo_{AF})$ is dominated by the other terms. The pattern of dark spots (a few of them are marked by the yellow circles) is identical to that observed in Fig. 3.6 (a), and later attributed to the topography-induced variations of the van der Waals force. Further contributions to the contrast may arise from a F-layer that is not completely flat or has a non-constant thickness. This would generate a stray field and a corresponding frequency shift contrast, $\Delta f_F(Sat_F, M_F, topo_F)$, even if the F-layer is saturated. A discussion in section 3.3.5 however shows that this contrast contribution can be neglected compared to $\Delta f_{vdW}(topo)$. Fig. 3.6 (d) summarizes all contrast contributions.

To distinguish the pinned AF moments from other sources of the contrast, the field was lowered to -1 T, saturating the F-layer and the tip magnetization in the negative direction. Again the topographical features dominate the contrast in Fig. 3.6 (e). Fig. 3.6 (f) schematically depicts the different contrast contributions. Note that the contrast generated by the imprinted pinned uncompensated AF moments reverses, because the magnetization of the tip has reversed, but the pinned uncompensated AF moments did not change their direction. Hence 1 T: $\Delta f_{AF}^{+1T}(D_{AF}, m_{AF}^{p-uc}, topo_{AF}) \rightarrow -1 \text{ T}: \Delta f_{AF}^{-1T}(D_{AF}, m_{AF}^{p-uc}, topo_{AF}) = -\Delta f_{AF}^{+1T}(D_{AF}, m_{AF}^{p-uc}, topo_{AF})$, while $\Delta f_F^{+1T}(Sat_F, M_F, topo_F) = \Delta f_F^{-1T}(Sat_F, M_F, topo_F)$, $\Delta f_{AF}^{+1T}(Sat_{AF}, m_{AF}^{r-uc}, topo_{AF}) = \Delta f_{AF}^{-1T}(Sat_{AF}, m_{AF}^{r-uc}, topo_{AF})$, and $\Delta f_{vdW}(topo)$ do not depend on the field. The corresponding MFM images, $\pm 1 \text{ T}$ are obtained at the same tip-sample distance of $z = 10 \pm 3 \text{ nm}$. The semi-sum of the data shown in Fig. 3.6 (g) and (h) is then caused by $\Delta f_{vdW}(topo)$, $\Delta f_F^{\pm 1T}(Sat_F, M_F, topo_F)$ and $\Delta f_{AF}^{\pm 1T}(Sat_{AF}, m_{AF}^{r-uc}, topo_{AF})$ (Fig. 3.6 (h)). As will be discussed in section 3.3.5, the topography-induced variations of the van der Waals force generated frequency shift, $\Delta f_{vdW}(topo)$, dominated the magnetic field mediated frequency shift terms. Hence, the latter two terms can be neglected. The contrast of Fig. 3.6 (g) then arises from the $\Delta f_{vdW}(topo)$.

Conversely, one half of the difference shows the contrast generated by the pinned AF moments (Fig. 3.6 (i) and (j)) only. The only term left in semi difference is that caused by the pinned AF moments $\Delta f_{AF}^{\pm 1T}(D_{AF}, m_{AF}^{p-uc}, topo_{AF})$. The thickness of the AF layer is only 1.5 nm. TEM revealed that its topography and variation of thickness remain smaller than 0.5 nm. All pinned AF moments are thus contained in a 1.5 nm thick layer with a roughness and thickness variation negligible in comparison to the tip-sample distance of 10 nm. Hence, $\Delta f_{AF}^{\pm 1T}(D_{AF}, m_{AF}^{p-uc}, topo_{AF}) = \Delta f_{AF}^{\pm 1T}(D_{AF}, m_{AF}^{p-uc})$. Surprisingly the semi-difference image (Fig. 3.6 (i)) shows a granular structure that neither resembles the topographical features visible in Fig. 3.6 (g) nor the granularity appearing inside the domains (Fig. 3.6 (a)), but an imprinted pattern of pinned uncompensated moments is not visible. Nevertheless such a pattern must exist. As the domain structure of the MFM image (Fig. 3.6 (k)) taken in a field of +0.26 T after saturation in -1 T

shows: The two large down bubble domains that were imaged after zero-field cooling reappeared at exactly the same locations, proving that a pattern of uncompensated moments that governs domain nucleation and growth must exist, albeit remain undetectable by MFM.

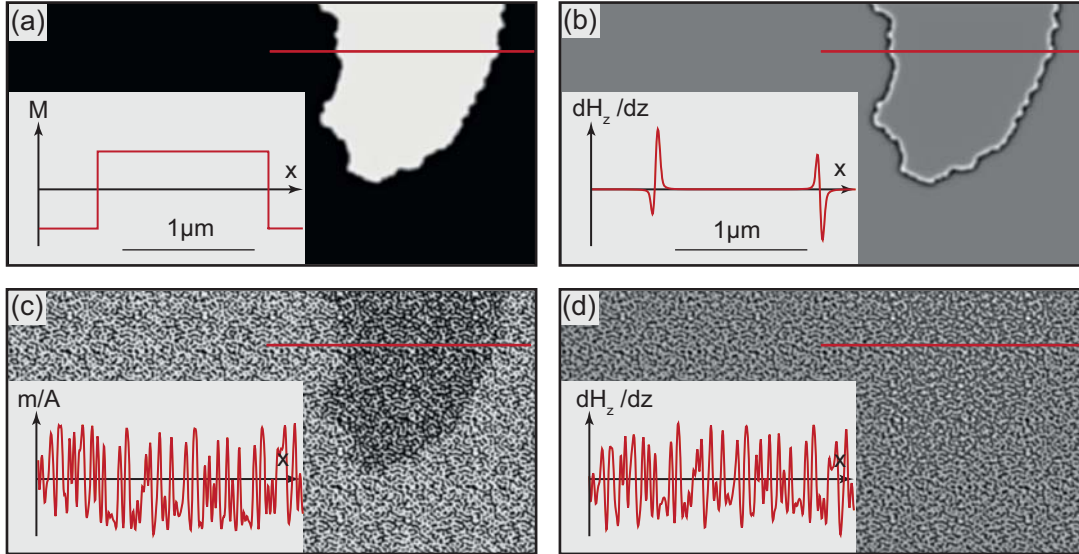


Figure 3.7: (a) model F-domain pattern. (b) domain wall contrast in calculated dH_z/dz -pattern. (c) model UCS pattern. (d) corresponding dH_z/dz -pattern.

In order to explore why the pinned uncompensated moment pattern is not visible in the MFM image Fig. 3.6 (i), we analyze the measurement in the upper of the image shown in Fig. 3.6 (a) in more detail. Fig. 3.7 (a) shows a bi-valued up-down model magnetization pattern reflecting the measured bubble domain and the corresponding dH_z/dz pattern, in Fig. 3.7 (b). As expected from the thickness loss factor $[1 - \exp(-kh)]$ in Eqn. 2.8 (see section 2.2), domains with a size much larger than the film thickness generate a stray field (H_z) and stray field derivative (dH_z/dz) only near the domain walls (Fig. 3.7 (b)). The distance from the surface was 16.9 nm. From our earlier work [13] we know that the imprinted pattern of pinned AF moments reflect the F-domain state present during the zero field cooling, but pinned uncompensated moment pattern shows a pronounced granularity.

On a length scale of grain size, about 10 nm, we modelled the pinned uncompensated moment pattern as follows: 1. a pattern identical to Fig. 3.7 (a) with an amplitude corresponding to $\pm 20\%$ of the magnetic moment density of a fully uncompensated CoO monolayer, 2. a random up/down granular magnetic moment distribution with an amplitude of $\pm 100\%$ of a CoO monolayer (Fig. 3.7 (c)). Fig. 3.7 (d) the corresponding dH_z/dz -pattern generated from that magnetic moment distribution pattern. The stray field derivative pattern arising from such a granular magnetic moment pattern is obviously granular too. The domain wall contrast nicely visible for a non-granular up/down magnetization pattern is now no longer visible but is discriminated by local stray field variations arising from the strong local variations of the magnetic moment density. Hence, the pinned AF moments is not or only barely visible Fig. 3.7 (d). Note that with prior knowledge of the domain wall position, a trained eye may still spot the domain wall in Fig. 3.7 (d), and possibly-with some good will, also in experimental data (Fig. 3.6

(i)). However note, although the imprinted pattern of pinned uncompensated moments is not visible in the MFM image displayed in Fig. 3.6 (i), the magnetization process is still governed by the pinned uncompensated AF moments: In a positive field of 0.26 T applied after saturating of +1 T and that of -1 T, a domain pattern closely resembling the initial one appears in Fig. 3.6 (k).

In conclusion we find that the successful imaging of an imprinted pattern of pinned uncompensated moments by MFM requires a suitably small domain size leading to an MFM image showing up/down domains (*domain contrast*), instead of an up/down contrast only near the domain walls (*domain wall contrast*).

3.3.4 Engineering the domain size [1]

The average size domain size for a magnetic thin film with perpendicular magnetic anisotropy is governed by the interplay of stray field energy and domain wall energy. The former decreases while the latter increases with decreasing domain size because more walls per unit area is required. Simple models for the domain size are for example described in [54]. In practice the domain size may however depend on weak magnetic field present during film fabrication or on the magnetic field history of the sample. For our CoPt-multilayer thin films we find that the domain size decreases from several microns to a few hundred nanometers at a critical thickness. Such a large film thickness is at odds with the constraint from high resolution MFM imaging that the F-layer be thin, to allow keeping the tip-to-F/AF-interface distance small. Providing that the F-layer ($F^{(top)}$) thickness small, but still engineer a suitably small domain pattern, a sample with a second much thicker F-layer ($F^{(bottom)}$) below the AF-layer is fabricated. Here we use a multilayer with a 10 CoPt repeats for $F^{(bottom)}$ layer. Fig. 3.8 (a) schematically represents the double F-layer sample with the basic structure as $F^{(bottom)}/S^{(dec)}/AF/F^{(top)}$. The two F-layers have a total thickness of 15 nm which sets the domain size to a few hundreds of nanometers. We chose an image with a size of $1\mu\text{m} \times 1\mu\text{m}$ and 256×256 pixels for a pixel size of $3.9\text{ nm} \times 3.9\text{ nm}$ sufficient for the best lateral resolution of about 10 nm achievable by our MFM. Hence, a domain width between 250 nm and 100 nm would allow for 4 to 10 domains within $1\mu\text{m}$ -sized image (Fig. 3.8 (b)). The 2.2 nm thick Cu layer, $S^{(dec)}$ breaks the magnetic exchange between the thick, $F^{(bottom)}$ layer and the AF-layer. Hence only $F^{(top)}$ is coupled to AF-layer.

Vibrating sample magnetometry measurements performed at room temperature reveal that both F-layers switch together (red loop in Fig. 3.9 with a coercive field $\mu_0 H_c(300\text{ K}) = \pm 9\text{ mT}$ and a saturation field $\mu_0 H_{sat}(300\text{ K}) = \pm 110\text{ mT}$). This is expected, because a reversal domain nucleating in $F^{(bottom)}$ layer will generate a stray field that locally adds to the applied external field facilitating nucleation of corresponding reversal domain in the $F^{(top)}$ layer. A distinctly different behavior is obtained after field cooling to 8.3 K in 2 T (black loop in Fig. 3.9). A major part of the magnetization still switches symmetrically with a coercive field $\mu_0 H_c(8.3\text{ K}) = \pm 54\text{ mT}$. This proves that the thick $F^{(bottom)}$ layer shows no exchange bias, i.e. that the 2.2 nm Cu layer, breaks the magnetic exchange interaction between the $F^{(bottom)}$ and the AF. A minor part of the magnetization switches asymmetrically at -405 mT and +156 mT. Thus the $F^{(top)}$ layer shows an exchange bias field of $\mu_0 H_{eb} = -124.5\text{ mT}$. From the magnetic moments and the sample area a magnetization of $M_{top} = 555564.0\text{ A/m}$ and $M_{bottom} = 529340.0\text{ A/m}$ is calculated for $F^{(top)}$ and $F^{(bottom)}$ layers, respectively. From the magnetization of $F^{(top)}$, an unidirectional exchange anisotropy is calculated as $A_{eb} = \mu_0 H_{eb} \cdot M_{top} \cdot t_{top} = 0.297 \cdot 10^{-3}\text{ J/m}^2$. Clearly, only the $F^{(top)}$ layer shows an EB-effect but both F-layers are expected to govern the size of F-domains.

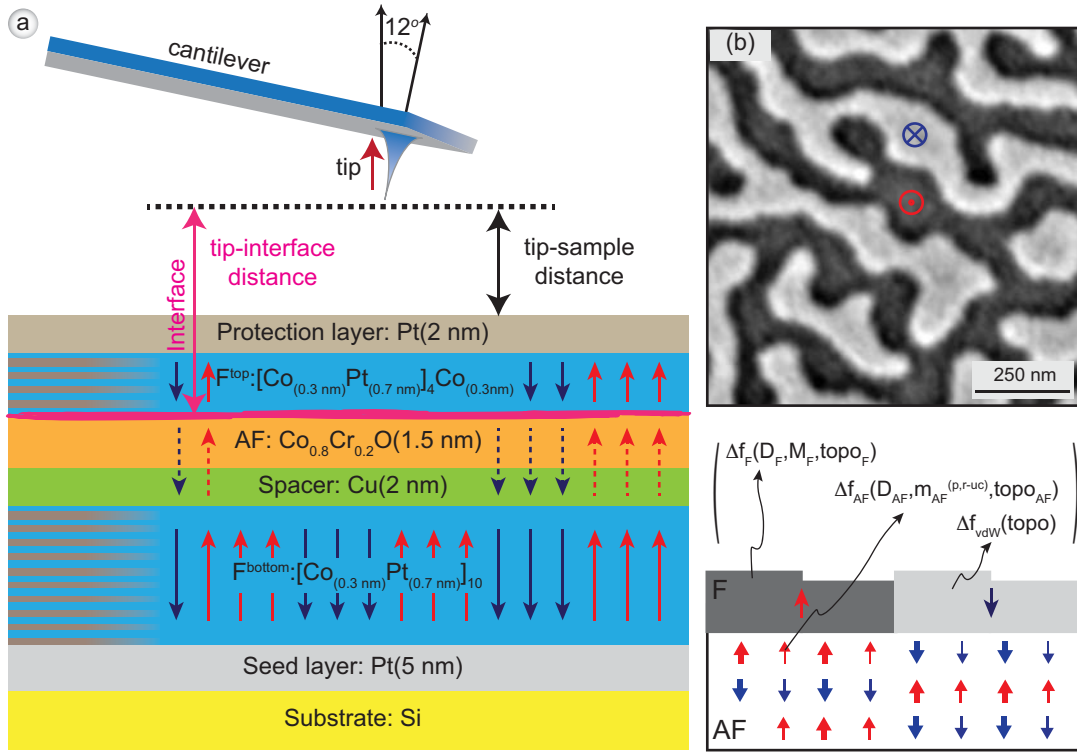


Figure 3.8: Schematic structure of the sample to keep the measurement surface closer to the sample surface so that the contrast due to solely pinned uncompensated AF moments can be visible by our MFM. Double F layer is Pt(5nm) $F^{(bottom)}$ /AF/ $F^{(top)}$ /Pt(2nm) with AF as 1.5 nm $\text{Co}_{0.8}\text{Cr}_{0.2}\text{O}$, $F^{(top)}$ as 4 repeated $[\text{Co}(0.3\text{nm})/\text{Pt}(0.7\text{nm})]_4/\text{Co}(0.3\text{nm})$. (b) MFM image of the double F layer sample with a few hundred nanometer-sized domains. The contrast of (b) is generated by the F layer ($\Delta f_F(D_F, M_F, topo_F)$), pinned and rotating uncompensated moments of AF-layer ($\Delta f_{AF}(D_{AF}, m_{AF}^{r-uc}, topo_{AF})$) and the topography-induced vdW force ($\Delta f_{vdW}(topo)$).

Fig. 3.9 (a) (or Fig. 3.8 (b)) shows the $1\mu\text{m} \times 1\mu\text{m}$ sized MFM image of the ferromagnetic domain pattern acquired after zero-field cooling the sample in its as-grown state to 8.3 K. In contrast to single F layer (Fig. 3.5(a)), the domains of the double F layer sample generate a pronounced *domain contrast*. Note that the size of MFM image, Fig. 3.5(a) is $4\mu\text{m} \times 4\mu\text{m}$ while that of Fig. 3.9 (a) $1\mu\text{m} \times 1\mu\text{m}$. In Fig. 3.9 (a) the measured contrast arises from the up/down domains penetrating both F-layers. The total frequency shift contrast of the image is 25 Hz. The domain pattern remained unchanged after the application of a field of 90 mT (b), which is considerably higher than the coercive field of the $F^{(bottom)}$ as determined from the M(H)-loop. This enhancement of the coercive field (compared to that of the uniformly magnetized sample) arises from stray field of the exchange-bias stabilized domains of the $F^{(top)}$. These provide a local magnetic field parallel to the local magnetization of the $F^{(bottom)}$ and hence stabilize the domain structure of the $F^{(bottom)}$. In the magnetometry experiment performed to measure the M(H)-loop displayed in Fig. 3.9, the magnetization process of the $F^{(bottom)}$ layer was measured with $F^{(top)}$ layer remained uniformly magnetized. There is thus no stray field emanating from

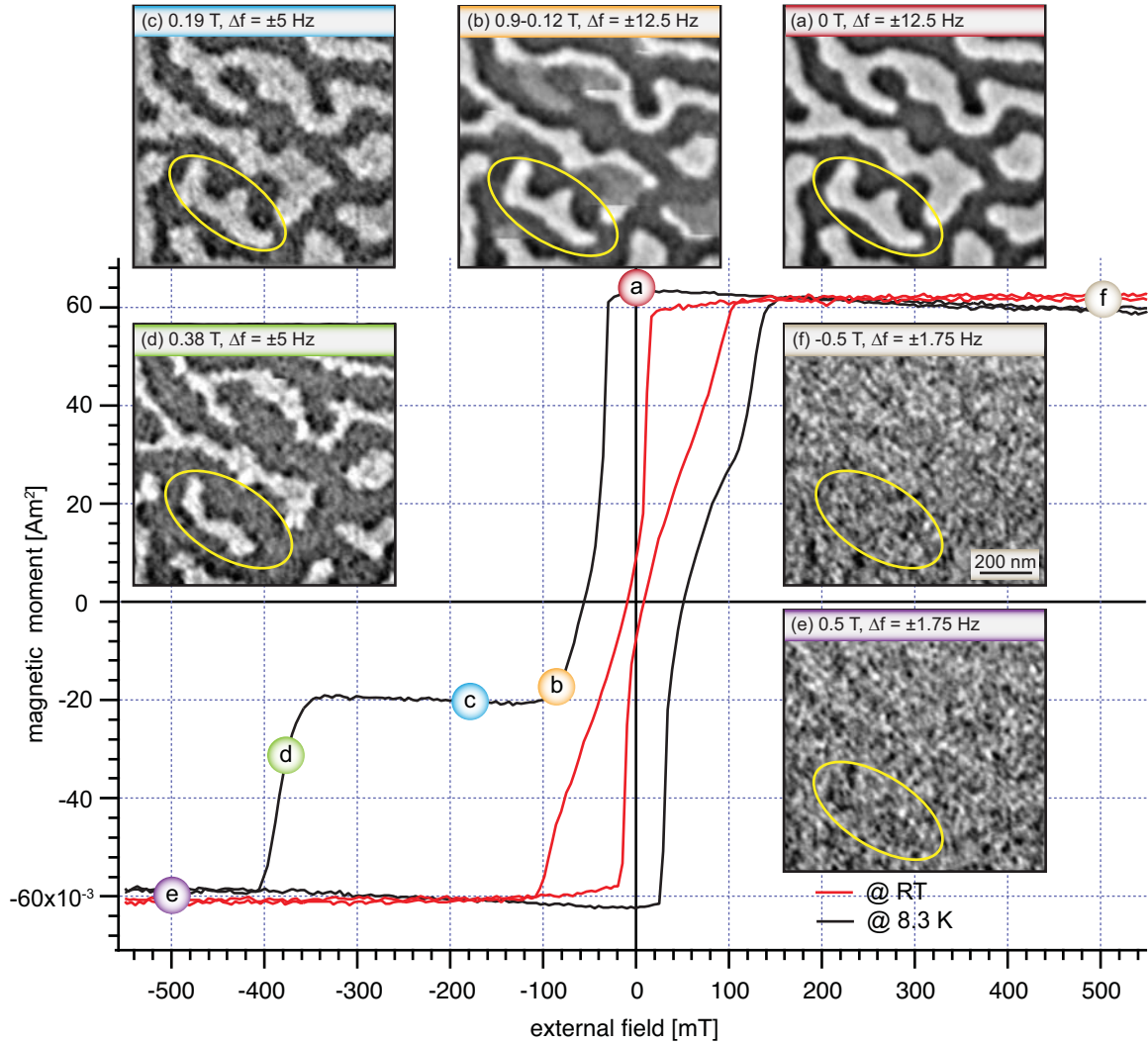


Figure 3.9: Vibrating sample magnetometry loops recorded at room temperature (red) and after field cooling in 2 T to 8.3 K (black). At low temperatures, the two F-layers switch independently. $F^{(bottom)}$ switches symmetrically in lower fields while $F^{(top)}$ shows an EB field, $\mu_0 H_{eb} = -124.5$ mT. $1 \mu\text{m} \times 1 \mu\text{m}$ MFM data from double F-layer sample's domain contrast (a) after zero-field cooling to 8.3 K, (b) after the 0.09-0.12 T, (c) after 0.19 T, (d) after 0.38 T, (e) after 0.5 mT, (f) and after -0.5 T.

the $F^{(top)}$ layer that stabilizes the domain in the $F^{(bottom)}$ layer. During the acquisition of Fig. 3.9 (b) the field was raised from 90 mT (bottom of image) to 120 mT (top of image). A noticeable part of the domains of the $F^{(bottom)}$ with a magnetization opposite to the applied field vanish or retract to the location of the domain walls of the exchange-bias stabilized $F^{(top)}$. At 190 mT (c), $F^{(bottom)}$ is saturated but the shape of domain pattern of the top F-layer still reflects the initial domain pattern of (a). The Δf -signal is however reduced from 25 Hz to 10 Hz. This reduced magnetic contrast makes the topography-induced spatial variations of the van der Waals force

more apparent. This leads to a well visible granularity on a 10-20 nm length scale corresponding well with the grain size of the sample. It is noteworthy that after the acquisition of the data for this image, the tip-sample distance was determined to be 9.3 nm. At 380 mT (d) the width of the white domains at $F^{(top)}$ shrinks considerably and at 430 mT most of the white domains are at erased. Note that the latter field corresponds to the (negative) coercive field of M(H)-loop.

At ± 0.5 T all domains have vanished and both $F^{(bottom)}$ and $F^{(top)}$ are saturated. At a field of ± 0.5 T the magnetization of the tip and sample are both parallel to the external field. Fig. 3.9 (e) and (f) are dominated by a granular contrast of about 3.5 Hz with a length-scale of about 20 nm. At a first glance, the initial domain pattern of the F-layers (a) is hardly visible. However, the trained eye may still observe, for example, the letter-F-shaped domain in (e) and (f) marked by the yellow ellipses. However, different from our earlier work mentioned in section 3.3.1, the contrast in (e) and (f) is clearly dominated by granular features that make the (inverted) initial domain pattern almost invisible. To distinguish the pinned AF moments from other source of contrast, the same procedure as in section 3.3.3 is applied (Fig. 3.10). Again, MFM data of the sample saturated in positive field (+0.5 T, Fig. 3.10 (c)) and in negative field (-0.5 T, Fig. 3.10 (e)) was acquired. The schematic figures (Fig. 3.10 (b), (d), (f)) show the various contributions to the measured MFM contrast in different external fields. As discussed in section 3.3.2, we calculate the semi-difference and semi-sum of the data acquired in ± 0.5 T (Fig. 3.10 (c) and (e)), to obtain the contrast caused by the imprinted pattern of uncompensated moments (Fig. 3.10 (i)) and contrast contributions of the topography, rotating uncompensated moments, variations of the magnetization, thickness and roughness of the F-layer(s) (Fig. 3.10 (g)). As in our earlier work [12, 13, 15, 19], the imprinted moments align antiparallel to the F moments. Note that Fig. 3.10 (a) is dominated by the frequency shift arising from the F-domains, $\Delta f_F(D_F, M_F, topo_F)$, but the contributions of the other terms, $\Delta f_{AF}(D_{AF}, m_{AF}^{p-uc}, topo_{AF})$, $\Delta f_{AF}(D_{AF}, m_{AF}^{r-uc}, topo_{AF})$ and $\Delta f_{vdW}(topo)$ need to be estimated. The term caused by the imprinted pinned uncompensated moments ($\Delta f_{AF}(D_{AF}, m_{AF}^{p-uc}, topo_{AF})$) is known from Fig. 3.10 (i) and hence can be subtracted. A subtraction of the data shown in Fig. 3.10 (g) and Fig. 3.10 (i) from Fig. 3.10 (a) reveals that:

$$\begin{aligned}
& data(\text{Fig. 3.10(a)}) - data(\text{Fig. 3.10(g)}) - data(\text{Fig. 3.10(i)}) \\
&= data(\text{Fig. 3.10(a)}) - [data(\text{Fig. 3.10(c)}) + data(\text{Fig. 3.10(e)})]/2 \\
&- [data(\text{Fig. 3.10(c)}) - data(\text{Fig. 3.10(e)})]/2 \\
&= data(\text{Fig. 3.10(a)}) - data(\text{Fig. 3.10(c)}) \\
&= [\Delta f_F(D_F, M_F, topo_F) + \Delta f_{AF}(D_{AF}, m_{AF}^{p-uc}, topo_{AF}) + \Delta f_{AF}(D_{AF}, m_{AF}^{r-uc}, topo_{AF}) \\
&+ \Delta f_{vdW}(topo)] - [\Delta f_F^{0.5T}(Sat_F, M_F, topo_F) + \Delta f_{AF}^{0.5T}(Sat_{AF}, m_{AF}^{r-uc}, topo_{AF}) + \Delta f_{vdW}(topo)] \\
&- [\Delta f_{AF}^{0.5T}(D_{AF}, m_{AF}^{p-uc}, topo_{AF})] \\
&= \Delta f_F(D_F, M_F, topo_F) - \Delta f_F^{0.5T}(Sat_F, M_F, topo_F) + \Delta f_{AF}(D_{AF}, m_{AF}^{r-uc}, topo_{AF}) \\
&- \Delta f_{AF}(Sat_{AF}, m_{AF}^{r-uc}, topo_{AF}).
\end{aligned}$$

where we have used that $\Delta f_{AF}(D_{AF}, m_{AF}^{p-uc}, topo_{AF}) = \Delta f_{AF}^{0.5T}(D_{AF}, m_{AF}^{p-uc}, topo_{AF})$ because the imprinted pattern of uncompensated moments do not depend on the field, and that $\Delta f_{vdW}(topo)$ does not depend on the external field. Further $\Delta f_{AF}(Sat_{AF}, m_{AF}^{r-uc}) \approx 0$, because in saturation the distribution of the rotating magnetic moments of the AF varies as a sub-grain scale, and hence generates only very weak fields with a spatial wavelengths smaller than 20 nm (the grain size). Hence their contribution to the MFM contrast can be neglected. The contribution of the

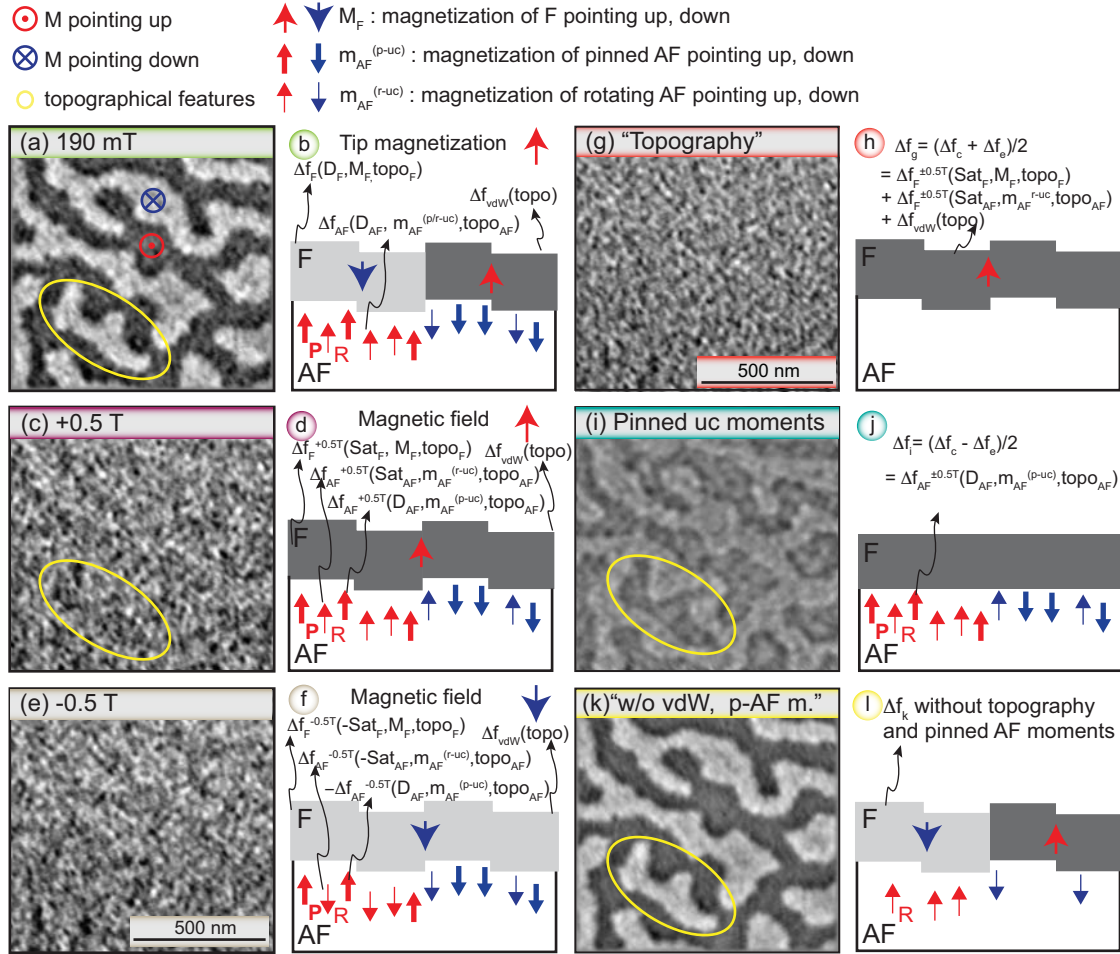


Figure 3.10: (a) after zero-field cooling to 8.3 K; (b) MFM contrast is generated by the F-layer, pinned and rotating uncompensated moments of AF-layer, and the topography-induced vdW force. Note that the contrast generated by F-layer depends on the geometry of the F-domains D_F . (c) saturation of the F-layer in 0.5 T, field applied parallel to tip magnetization; (d) Note that the contrast now arises from the saturated F-layer, and notice further that the frequency shift generated by the rotating moments changed, from $\Delta f_{AF}(D_{AF}, m_{AF}^{r-uc}, topo_{AF})$ to $\Delta f_{AF}^{+0.5T}(Sat_{AF}, m_{AF}^{r-uc}, topo_{AF})$ at saturation. The distribution of the pinned AF moments (m_{AF}^{p-uc}) does not change with the applied field. (e) saturation in -0.5 T, field applied antiparallel to tip magnetization; (f) Note that the contrast generated by the imprinted pinned uncompensated AF moments now reversed, because the magnetization of the tip has reversed. (g) is semi sum of the MFM image taken in +0.5 T and -0.5 T; (h) shows the contrast contributions of the MFM image (g) schematically. (i) is semi difference of the MFM image taken in +0.5 T and -0.5 T; (j) the contrast generated by the pinned AF moments only. (k) is the subtraction (g) and (i) from (a) with a less granular contrast.

term $\Delta f_{AF}(D_{AF}, m_{AF}^{r-uc}, topo_{AF})$, i.e. that caused by the pattern of uncompensated moments imprinted by the F domains that however rotate with the F magnetization in a local field,

cannot be neglected. However, magnetic moments of the AF will be detected as an (slightly) enhanced magnetic moment of the F in a magnetometry experiment. Hence instead of measuring M_F , the (non-element specific) magnetometer will measure $M_F^{enhanced} = M_F + V_{AF} \cdot m_{AF}^{r-uc}$. Consequently Fig. 3.10 (k) shows contrast generated by $\Delta f_F(D_F, M_F^{enhanced}) + [\Delta f_F(D_F, topo_F) - \Delta f_F^{0.5T}(Sat_F, topo_F)]$. Note that the contribution of the topography-induced variation of the vdW-force, $\Delta f_{vdW}(topo)$ is no longer contained in Fig. 3.10 (k). The size terms in []-brackets arising from the roughness of the F-layer(s) and variations of its thickness and magnetization will be estimated in the following section 3.3.5. The effect of the terms arising from the topology of the F-layer(s) is visible in Fig. 3.10 (k) in form of a granularity with a very weak contrast showing up particularly in the white domains. This proves that the more pronounced granularity visible in Fig. 3.10 (a) is predominantly caused by $\Delta f_{vdW}(topo)$ and small-scale spatial variations of $\Delta f_{AF}(D_{AF}, m_{AF}^{p-uc}, topo_{AF})$.

3.3.5 Analysis of the Topography Induced Magnetic and Non-magnetic contrast

The MFM data presented in section 3.3.4 were acquired at a tip-sample distance of 9 nm to maximize the lateral resolution. This tip-sample distance is only about a factor of 2-3 larger than the typical topography of our samples. As the frequency shift versus distance data presented in Fig. 2.4 shows, a variation of the tip-sample distance by even ± 1 nm will cause a frequency shift variation of ± 0.79 Hz. Thus the topography-induced variations van der Waals force are expected to be the dominant source for the contrast visible in Fig. 3.10 (g). Contributions of magnetic origin can be estimated once the tip-transfer function is determined (see section 2.4). Contrast

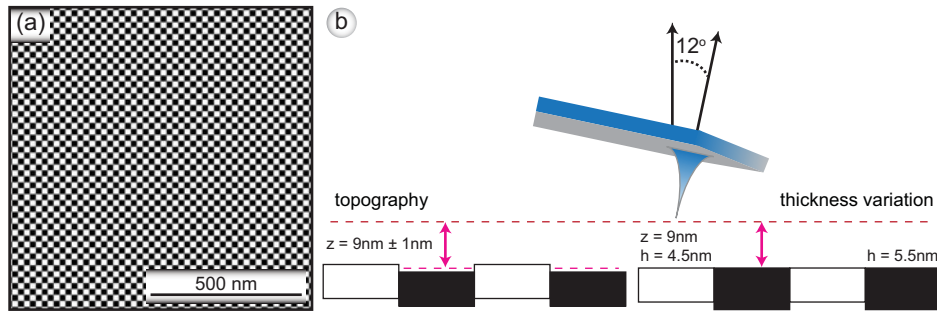


Figure 3.11: Model calculation (a) a checker-board pattern created with a feature size of 5×5 pixels corresponding to $19.53\text{ nm} \times 19.53\text{ nm}$ is used for the model calculations. (b) roughness and thickness variations of F-layers.

contributions arising from magnetic fields generated by topological variations of the saturated F-layer(s) can be estimated from stray field calculations performed on model structures. Assuming that the topological variations have a length scale corresponding to the size of the grains (10-20 nm), a checker-board pattern with a feature size of 5×5 pixels corresponding to $19.53\text{ nm} \times 19.53\text{ nm}$ is used for the model calculations (Fig. 3.11 (a)). The roughness and thickness variations determined by transmission electron microscopy (TEM). The roughness is smaller than $\pm 2\text{ nm}$ and the thickness variations remain below $\pm 0.5\text{ nm}$. The F corresponding model patterns are shown in Fig. 3.11 (b). We find a contrast of $\pm 0.26\text{ Hz} (\pm 0.13\text{ Hz})$ and $\pm 0.52\text{ Hz} (\pm 0.01\text{ Hz})$

for a roughness of ± 2 nm and a thickness variation of ± 0.5 nm of the top(bottom) F-layer, respectively. A variation of saturation magnetization of F^{top} of ± 16.2 % leads to a contrast of ± 0.043 Hz and for F^{bottom} leads to the ± 0.010 Hz. Note that such a magnetization variation also serve as a model to calculate a largest thinkable upper limit for spatial variations of rotating uncompensated moments. If the magnetic moments of responsible for the ± 16.2 % variation of the magnetization of F^{top} are projected into one plane, a magnetic moment areal density of $4.5 \times 10^{-4} \text{ Am}^2/\text{m}^2$ is obtained. This corresponds to ± 1 monolayer of uncompensated Co spins in CoO. The term $\Delta f_{AF}(Sat_{AF}, m_{AF}^{r-uc}, topo_{AF})$ can thus be neglected safely. The magnetic contrast generated by the variation of the topography or saturation magnetization of the F-layer is thus considerably smaller than the contrast caused by variations of vdW force. Table 3.1 summarizes result of model calculations. Hence we can conclude that the contrast of the data shown in Fig. 3.10 (d) is dominated by topography-induced variations of the vdW force.

thickness with ± 0.5 nm	roughness with ± 2 nm	magnetization ± 10 %	vdW force with ± 1 nm
± 0.52 Hz F^{top}	± 0.26 Hz	± 0.026 Hz	± 0.79 Hz
± 0.01 Hz F^{bottom}	± 0.13 Hz	± 0.006 Hz	± 0.79 Hz

Table 3.1: contrast induced by the variations of topography, thickness and magnetization variation of F^{top} and F^{bottom} . The last column gives the contrast due to ± 1 nm topography-induced vdW force.

3.3.6 Areal density of the pinned uncompensated AF moments

In chapter 2 MFM image formation is discussed in detail. It has been shown that the MFM contrast generated by the stray field (derivative) emanating from a pattern of F-domains or pinned AF moments is best calculated in a 2d Fourier Space (k_x, k_y, z) . For this the instrument calibration function $ICF(\mathbf{k})$, or more specifically that a-priori unknown part of it, the transfer function describing the tip-equivalent magnetic charge $q_{tip}(\mathbf{k})$ must be determined. Conversely, once the

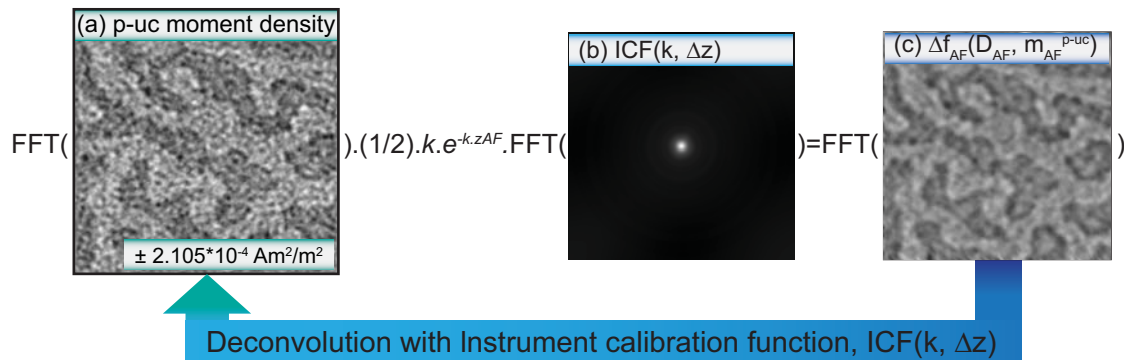


Figure 3.12: (a) pattern of uncompensated magnetic moments per unit area, as obtained from the deconvolution of the frequency shift pattern generated by the pinned uncompensated AF moments, $\Delta f_{AF}(D_{AF}, m_{AF}^{p-uc})$.

ICF(\mathbf{k}) is known, the z component of the projected areal density of the pinned uncompensated moments can be extracted from the measured frequency shift, $\Delta f_{AF}(D_{AF}, m_{AF}^{p-uc})$ (Fig. 3.12). Hence, using the Eqns. 2.11, 2.6, 2.4, and the instrument calibration function ICF($k, \Delta z$) (determined as described in section 2.4), the z component of the projected areal density of the pinned uncompensated moments in Fourier Space can be calculated from

$$\frac{m_z^{AF}(k)}{A} = -\frac{\Delta f^{AF}(k, z_0)}{\text{LCF}^2(k) \cdot k^2 \cdot \exp[-k(z_0 + \Delta z)] \cdot \text{ICF}(k)}, \quad (3.1)$$

where $\Delta f^{AF}(k, z_0)$ is the Fourier transform of the frequency shift image shown in Fig. 3.12 (c). For numerical reasons we did not perform a simple division as indicated in Eqn. 3.1 but used a Tikanov deconvolution procedure. Fig. 3.12 (a) shows the pattern of the pinned uncompensated AF moments per unit area.

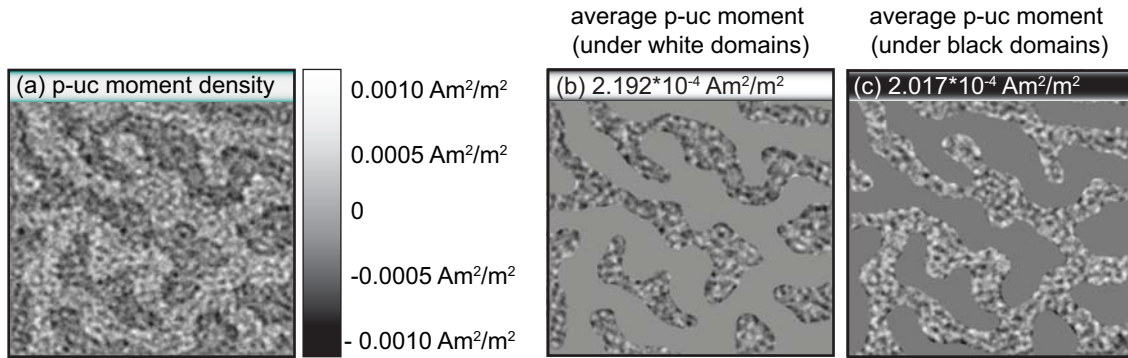


Figure 3.13: Calculation of the average pinned AF moment density: a) is the pinned uncompensated moment distribution deconvolved from the contrast of pinned uncompensated AF moments. In b) and c) the masks are used to calculate the uncompensated moment density under white and black domains, respectively.

In order to calculate the average uncompensated moments under within down(white) and up(black) domains, a mask based on the magnetization pattern of F-domain is used. In order to avoid artifacts and positioning errors that may occur near the domain walls, the width of the acceptance area of the up/down mask is reduced artificially by a few pixels. The result of the application of the up/down masks are shown in Fig. 3.13 (b) and (c), and the calculated values of pinned uncompensated moments are $-2.192 \cdot 10^{-4} \text{ Am}^2/\text{m}^2$ and $+2.017 \cdot 10^{-4} \text{ Am}^2/\text{m}^2$, respectively. The asymmetry between the calculated values under each domain arises from an asymmetry or arbitrary offset of the up/down frequency shift pattern. Note that the absolute value of the Δf pattern is ill-defined, because the vdW force generates a negative frequency shift offset. We usually represent our data showing an 50/50 % up/down Δf -contrast by subtraction of the average frequency shift. A small inequality of the up/down domain areas then leads to a corresponding inequality of the up/down magnetic moment density. Assuming that the two values must be the same we find an average magnetic moment density $\pm 2.105 \cdot 10^{-4} \text{ Am}^2/\text{m}^2$. The numerical quality of the deconvolved $\frac{m_z^{AF}(k)}{A}$ -pattern (Fig. 3.13 (a)) can be judged from the difference pattern calculated from the $\Delta f_{AF}(D_{AF}, m_{AF}^{p-uc})$ -image, Fig. 3.10 (i) (or Fig. 3.14 (c))

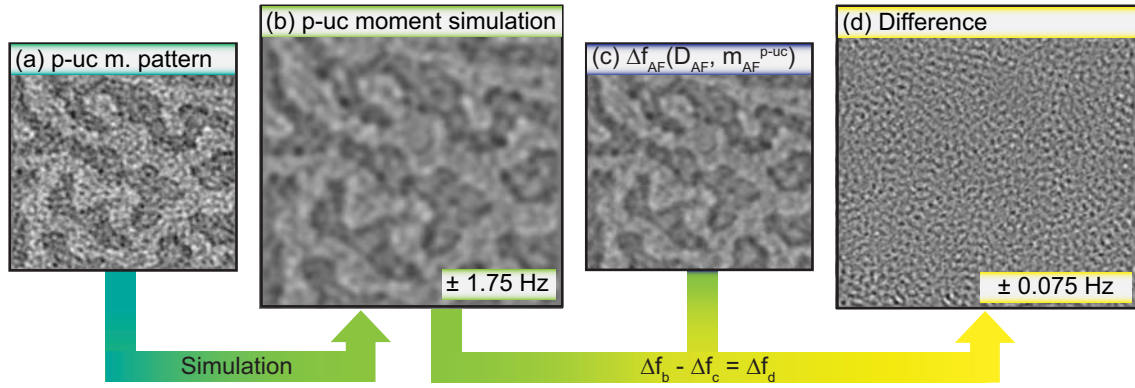


Figure 3.14: Simulation of the uncompensated moment pattern (a), compare (b) to Fig. 3.10 (e) which is the contrast due to the pinned uncompensated moments in AF layer or at the interface. d) is the difference of the simulated pattern (b) and pinned uncompensated AF contrast (c) , note the scale is 1/10

and the corresponding image (Fig. 3.14 (b)) calculated from the deconvolved uncompensated moment pattern $\frac{m_z^{AF}(x,y)}{A}$, Fig. 3.14 (a). The difference image is depicted in Fig. 3.14 (d) has a peak-to-peak contrast of 150 mHz, i.e. 1/10 of the pinned magnetic moment contrast (Fig. 3.14 (c)). This indicates that the local values of the $\frac{m_z^{AF}(x,y)}{A}$ -pattern could be evaluated with a precision about $\pm 10\%$. Note also that tip-calibration and deconvolution procedure depend on the precision of the determination of the tip-sample distance, that is about ± 0.5 nm. For an average domain size of 233.9 ± 15 nm a distance error of 1 nm generate an error of $E_D = 1 - \exp(-k \cdot 1 \text{ nm}) = 0.0269(2.7\%)$, which can be neglected.

An alternative method to estimate the average pinned uncompensated moment areal density (but not the local values) is to compare, the average up/down frequency shift contrast of the MFM images of the F-domains, (Fig. 3.10 (a)) and the imprinted pinned uncompensated moment pattern, (Fig. 3.10 (i)). In this method, the calibration of the response of the tip, i.e. a determination of the $ICF(k, \Delta z)$ is not required. From Eqns. 2.9, 2.6 and 2.11, the average areal density of the pinned uncompensated moment for a given $k = \frac{2\pi}{\lambda}$ becomes:

$$\frac{\overline{m_z^{AF}(k)}}{A} = M^F \cdot \frac{[1 - \exp(-k \cdot h)]}{k} \cdot \frac{\overline{\Delta f^{AF}(k, z_0)}}{\overline{\Delta f^F(k, z_0)}}. \quad (3.2)$$

Note that the average wavelength λ can be determined from the average domain size. From counting the number of domain walls for each line in x and y direction of the 256×256 pixels image, we find $\bar{\lambda} = 233.9 \pm 15$ nm. To determine the average contrast $\overline{\Delta f^F}$ and $\overline{\Delta f^{AF}}$ data of the F-domains and the pattern of pinned uncompensated AF moments, respectively, the local contrast values are averaged separately for the up/down domains. Using the values (see Fig. 3.15) $\overline{\Delta f^F} = \pm 2.25$ Hz and $\overline{\Delta f^{AF}} = \pm 0.214$ Hz in the Eqn. 3.2 reveals an average magnetic moment density $\frac{\overline{m_z^{AF}(k)}}{A} = 2.318 \cdot 10^{-4} \text{ Am}^2/\text{m}^2$. This values is in good agreement with $\frac{\overline{m_z^{AF}(k)}}{A} = \pm 2.105 \cdot 10^{-4} \text{ Am}^2/\text{m}^2$ found via averaging the $\Delta f_{AF}(D_{AF}, m_{AF}^{p-uc})$ -data deconvolved by the instrument calibration function.

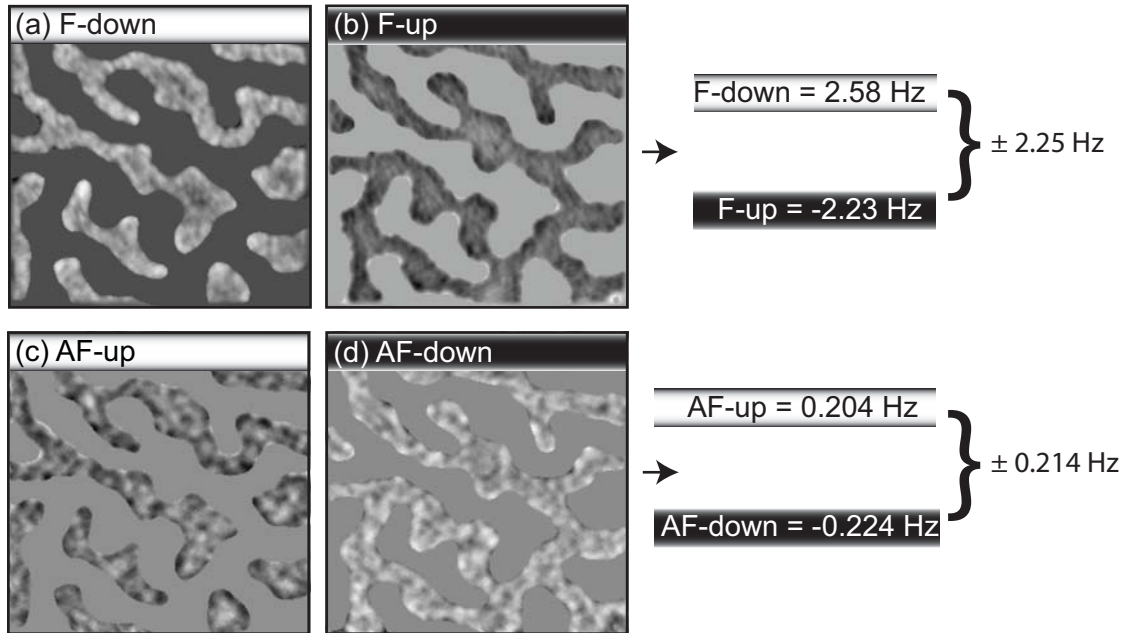


Figure 3.15: In a) and b) the masks are inserted for the calculation of the average contrast of up-down (white-black) domains for the F layer. In c) and d) the same masks are used for up/down pinned uncompensated moments of the AF layer.

The z -component magnetic moment density of a fully uncompensated CoO [111] -plane is $4.48 \cdot 10^{-4} \text{ Am}^2/\text{m}^2$ based on $+3.8\mu_B$ per Co^{2+} . We find that the averaged pinned areal moment density corresponds to $\pm 46.98 \%$ of a monolayer of fully uncompensated moments, and local values that are 5 times higher. Note that with the 20%Cr, added and driven to grain grain boundaries, we find an about 1.45 amplification of the uncompensated moment density. Compared to a sample with Cr (see Chapter 4), we estimate the $p\text{-uc}$ for an AF without Cr would give: 28.47 % - 27.64 %, which agrees very well with Schmid's results [19].

3.4 Discussions and Conclusions

Magnetic force microscopy measures the magnetic field emanating from all magnetic moment distributions in a closer vicinity of the sample surface. MFM cannot directly distinguish different field sources. It misses the element-specificity of x-ray methods. However, MFM can be operated even in strong magnetic fields (in contrast for example to XMCD-PEEM). From data acquired on suitably designed exchange-bias samples in different external fields, different sources for the measured contrast can be deconvolved. In particular the stray field arising from patterns of imprinted uncompensated spins can be imaged with a spatial resolution down to 10nm. Using deconvolution techniques, these patterns can be analysed quantitatively in terms of magnetic moments per unit area with a sensitivity of about 1% of a fully uncompensated monolayer of AF moments. In this respect the MFM method used in this thesis is far superior than to-dates x-ray methods as citations from present literature indicates:

- Ohldag *et al.* Phys. Rev. Lett. 91 (2003) 017203 [16] “we find that only 4% of the interface layer contains pinned spins. We believe that the tiny fraction of uncompensated pinned spins is the very reason that has impeded”.
- Offi *et al.* Phys. Rev. B 67 (2003) 094419 [52] “Part of the induced net moment measured in Fe and Mn could consist of uncompensated AFM spins. However, due to the rather low magnetic signal, it is quite difficult to distinguish the part strongly coupled to the AFM lattice spins, giving rise to the exchange bias effect”.
- Tieg *et al.* Appl. Phys. Lett. 96 (2010) 072503 [55] “We also tried to image the uncompensated moments in the IrMn layer by soft x-ray holography but we could not observe any magnetic contrast at the Mn L_3 edge. This can be understood by the small amount of uncompensated AFM moments, ... and the strong background intensity in the transmission spectra, which result in the vanishing Mn XMCD signal”.

The density of pinned uncompensated magnetic moments found in our work seems rather high ($\pm 10\%$). Such a high density of uncompensated moments can not be explained by simple mechanisms such as Meiklejohn and Bean model, Malozemoff Random Field model and Takano model etc. (see sections 1.1,1.4,1.5). The high density of pinned uncompensated magnetic moments in our work points towards strongly disordered F/AF interface with a high defect density leading to spin-glass like state (see section 1.6) of the F/AF interface. Possibly, grain boundaries in our polycrystalline materials provide a low-energy spatial location for domain walls in the AF, and allowing a further enhancement of the magnetic moment density (as domain state model in section 1.5). It is further noteworthy that for Co/CoO and for Co/MnIr F/AF systems we find that the pinned uncompensated moments align antiparallel to the F moments. This is in agreement with newer XMCD reflectometry work [51].

In order to generate an exchange bias effect, the following required but possibly not sufficient conditions must be fulfilled: Firstly the existence of uncompensated magnetic moments that remain pinned to a magnetically stable AF lattice, and secondly, the exchange coupling of the pinned uncompensated magnetic moments with the F moments. The coupling between the pinned uncompensated moments and the F moments depends on details of the exchange interaction and can thus be ferromagnetic or antiferromagnetic.

There is a general tendency that ferromagnetic coupling is stronger than antiferromagnetic coupling (this is the reason that Néel temperature (T_N) of typical AF material is below the Curie temperature, T_C of typical F materials). In order to fulfill both conditions for exchange bias we conclude that a weaker antiferromagnetic coupling between the F moments and the pinned AF moments may be necessary condition for these AF moments to remained locked (pinned) to the AF lattice (Fig. 3.16 (a) and (b)). If a strong ferromagnetic coupling between the F moments and the uncompensated moments would exist, the weaker presumably antiferromagnetic exchange of the latter moments to the AF lattice would be broken, when the F magnetization is reversed. The uncompensated moments would then rotate with the F magnetization (Fig. 3.16 (c) and (d)). It is noteworthy that in our work we always found antiferromagnetic coupling between the F moments and the pinned uncompensated moments for both types of AF materials used (CoO, MnIr) for samples grown at Hitachi HGST, Almaden, CA by E. Fullertons group and by our group at EMPA. Further recent XMCD reflectometry work [51] assessing the depth distribution of the pinned and rotating uncompensated moments found that the former moments couple antiferromagnetically and the latter ferromagnetically with the F moments. These observation

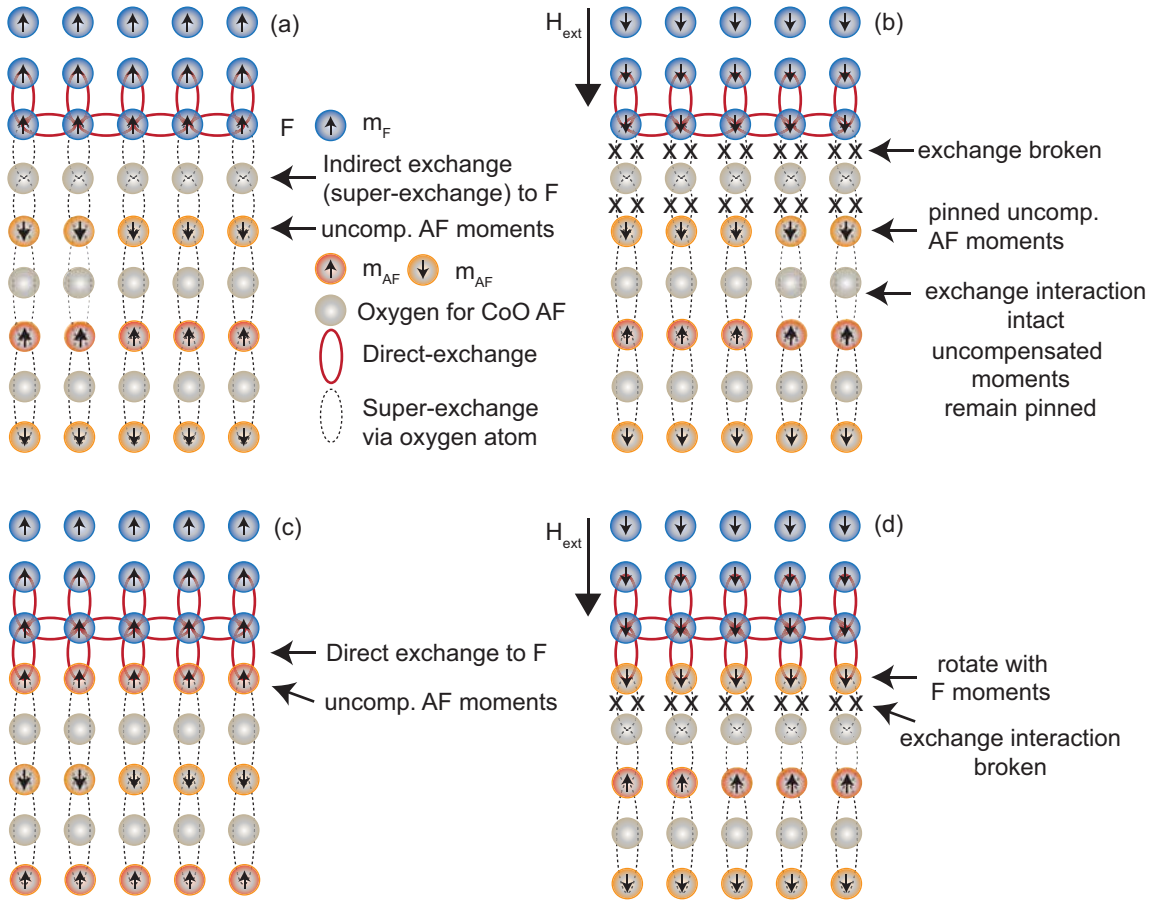


Figure 3.16: coupling via another atom; (a) a weaker antiferromagnetic coupling between the F moments and the pinned AF moments, (b) the uncompensated AF moments remain locked as the reversal of the F magnetization. (c) Direct coupling of the F moments with the uncompensated moments, (d) reversal of the F magnetization breaks the coupling of F moments with the uncompensated moments, thus the latter rotates with the former.

also supports our argument depicted in Fig. 3.16. Considering a conventional ferromagnetic domain wall that is never atomically sharp but extends many lattice spacings, the “breaking of the exchange” at a F/AF interface may not be atomically sharp, but a smoother rotation over some lattice spacings may occur, to reduce the overall loss of exchange energy. However even in this more elaborated model of horizontal partial domain walls, the strongest local rotation would occur at the point of the exchange interaction. Hence again an AF-exchange between the F moments and the pinned uncompensated moments are favorable. For the formation of the horizontal walls see also the chapter 5.

Chapter 4

Enhancement of the Exchange Bias

In chapter 3 we discussed in more detail how exchange bias requires a net coupling between the F moments the AF- layer. The latter is ultimately governed by the density of pinned uncompensated moments. Earlier work by Schmid *et al.* [15] established a first direct proof of this assumption in perpendicular systems. It follows that an enhancement of the exchange bias could be achieved by increasing the interfacial AF uncompensated moment density. Whereas most earlier work [30, 56] explores the usefulness of engineering defects in the AF as a strategy for increasing the UCS density, in this chapter we address the problem of coupling frustration at the scale of individual AF grains.

4.1 Coupling frustration at F/AF interfaces and exchange bias

Recent theoretical work (cf. Chapter 1) has sought to ascertain the relation between the moment configuration at the F/AF interface and the exchange field. In particular, Radu’s model [32] (cf. section 1.6) advances the notion of a “frustrated” spin system at the F/AF interface. Frustration implies a reduction of the net exchange coupling between the pinned uncompensated AF moments and the F moments.

At the smallest scales the origin of frustration can be found in the magnetic order in the AF. Indeed, if two adjacent interfacial AF spins of the opposite sub-lattice couple to the F, the antiferromagnetic coupling between the AF spins and between AF and F spins cannot be realized simultaneously. Therefore fully compensated interfaces are frustrated at scales of single lattice constants. Even fully uncompensated AF interfaces, which expose spins of one same sub-lattice to coupling with the F, can be frustrated. This happens at the slightly larger scale that characterizes the departure from an atomically flat interface and the existence of steps in it. In such cases the F/AF interface comprises stepped surfaces of opposing AF-sub-lattices, themselves uncompensated. But the antiparallel coupling to the F cannot be realized simultaneously in all steps, hence the frustration. Imperfections in the AF order, arising from chemical intermixing, deviations from stoichiometry, structural inhomogeneities, low coordination, etc. can partly lift the frustration. This is tantamount to increasing the number of net directional coupling or uncompensated AF spins. Insight into the relation between frustration and exchange bias is provided in recent work by Schmid *at al* [15]. In Fig. 4.1 we reproduce results from that work to illustrate how areas comparable to the width of one or a few grains in the film can parallel F/AF coupling. Specifically, Figures 4.1(b)-(d) show an overlay of the contours of the F-domains from

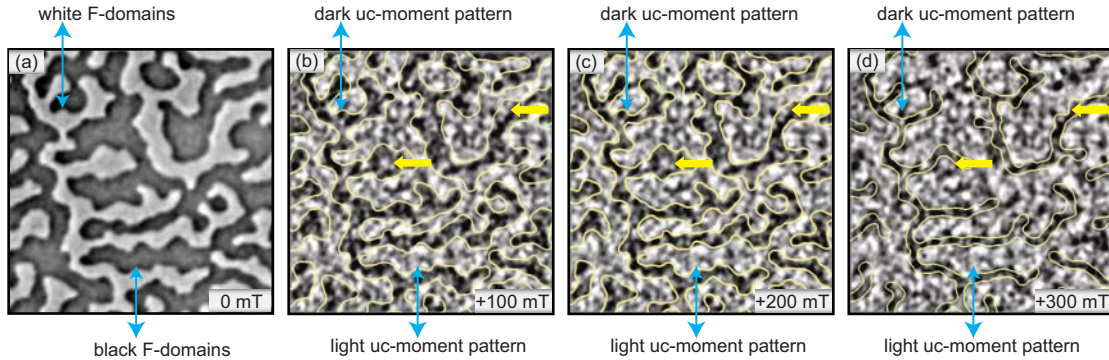


Figure 4.1: MFM images of the as-grown CoO/CoPt-singlelayer sample: The $2 \times 2 \mu\text{m}^2$ sized MFM image is taken in 0 mT (a). (b)-(d) show the AFM-contrast observed in +300 mT, when the FM layer is saturated. The contour lines of the FM domains in 0 mT (a), +100 mT and +200 mT were overlaid to the AFM-contrast and are shown in (b)-(d), respectively. In (b)-(d), the contrast arising from the uncompensated moment is dark(light) under the white(black) F-domains, i.e. antiparallel coupling. However, in some isolated locations (anti-biasing regions) the contrast is light(dark) under white(black) F-domains, i.e. parallel coupling. By increasing the field from 0 mT \rightarrow +100 mT \rightarrow +200 mT, the “white” F-domains show the tendency to retract from locations with positive coupling (anti-biasing regions, marked by yellow arrows), and the average AF-contrast below these domains (see (d)) becomes more negative.

Fig. 4.1 (a) (and as well as for higher applied fields, not shown) with the local areal density of pinned uncompensated AF spins. The latter was measured with a lateral resolution of 10 nm. We can see that F-domains magnetized antiparallel to the applied field (“white” in Fig. 4.1 (a)) shrink, and in so doing retreat to areas where the F/AF coupling is more predominantly antiparallel (deeper “black” contrast). By quantifying the average areal density of pinned uncompensated spins over the area of the retreating domains Schmid *et al* found a relation between the exchange-field and the latter. More precisely, the exchange field was found to be roughly proportional to the average density of *antiparallel* coupling F/AF pinned uncompensated spins. One can see the “isolated” areas of the film where the F/AF coupling is parallel, that is “white” areas underneath “white” F-domains (see the yellow arrows in Fig. 4.1 (b)-(d)). They reduce the net areal density of pinned uncompensated spins under the white domains, which retreat from these areas first. With the understanding provided by Schmid *et al* [15] we can therefore view the parallel coupling areas as *anti-biasing*.

4.1.1 Frustration from exchange-coupled AF-grains

Notice that the pinned uncompensated spin density is not uniform (Fig. 4.1). Moreover, taking into account the typical grain size of our CoO layer, about 20 nm, the anti-biasing areas extend over interface areas of a few AF grains. Therefore, the F/AF coupling frustration that gives rise to this anti-biasing spans more than a single grain, involving the grain boundaries.

Figure 4.2 illustrates the situation envisioned. When the AF-grains are not exchange coupled, or only weakly so, they can adopt an order which is largely determined by those grains’ F/AF

interface, Fig. 4.2 (b). In contrast, inter-granular coupling could lead to the situation where total F/AF coupling energy of one grain could be exceeded by the energy of coupling to neighboring AF grains. That case is outlined in Fig. 4.2 (a), where we can appreciate how as a result the coupling between F/AF in the left grain is anti-biasing. In an alternative view weakly coupled or decoupled AF grains facilitate the formation of domain walls inside the AF (see section 1.5).

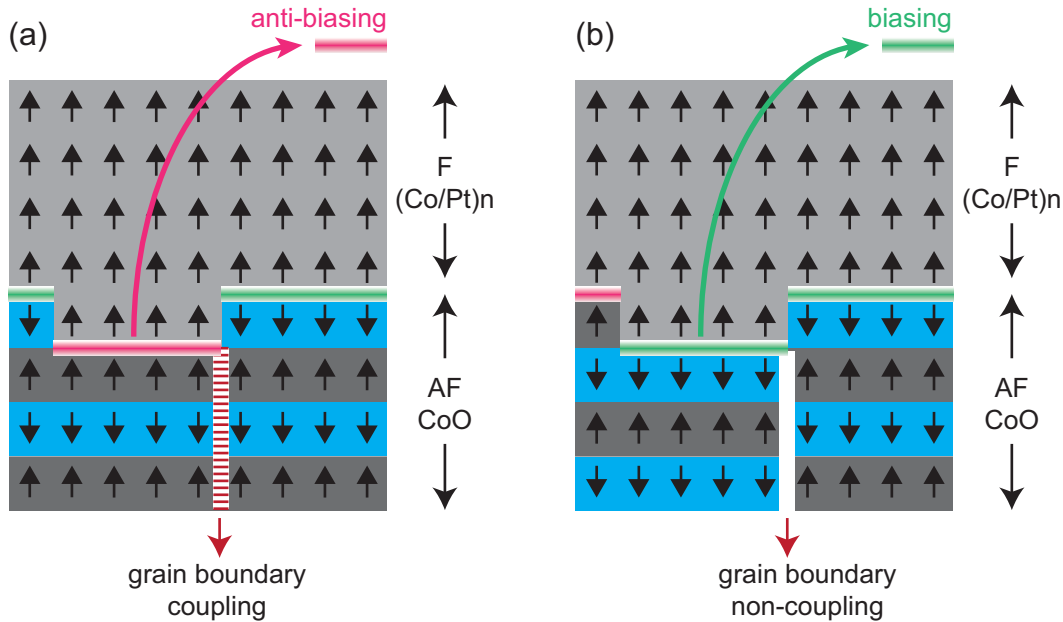


Figure 4.2: Schematic of a F/AF coupling frustration spanning the interface area of multiple AF grains. (a) Fully uncompensated AF interfaces have steps, leading to intra-grain frustration. Due to exchange coupling to neighboring grains the F/AF interface area of one grain may have an overall parallel coupling, i.e. have an anti-biasing contribution to the total coupling. (b) Removing the inter-grain coupling allows each AF grain to minimize the total F/AF coupling energy independently. The net coupling over the F/AF interface of a given grain is therefore anti-parallel, i.e. biasing.

These concepts suggest that a possible strategy for increasing the number of uncompensated pinned spins is to decouple the AF grains, Fig. 4.2 (b).

4.2 Exchange-decoupling Antiferromagnet Grains

A CoO-based exchange-biased system is well suited to exploring the hypothesis of frustration reduction by AF-grain decoupling, because CoO films can be fabricated by oxidizing metallic Co films. Thus, prior to oxidation we can utilize grain boundary engineering techniques originally developed for Co-alloy magnetic recording media. With particularly beneficial consequences for the signal to noise ratio in such media [57], Cr additions to Co were found to segregate to grain boundary upon annealing at 150°C [58, 59, 60]. Various mechanisms [61, 62, 63, 58, 64, 60, 65, 59, 66] then cause the magnetic decoupling of the Co grains.

For our experiments post-annealing oxidation can be used to produce CoO films with Cr_2O_3 grain boundaries, which exchange decouple the CoO grains. Metallic ferromagnetic layers deposited on this oxide film complete the exchange-bias structure.

We prepared exchange-bias structures of the form: $\text{Si}/\text{Pt}_{(5\text{nm})}/[\text{Co}_{0.3\text{nm}}\text{Pt}_{0.7\text{nm}}]_{10}/\text{Cu}(2.2\text{nm})/[\text{Co}_{(1-x)}\text{Cr}_{(x)}\text{O}]_{(\approx 1.5\text{nm})}/[\text{Co}_{0.3\text{nm}}\text{Pt}_{0.7\text{nm}}]_4/\text{Pt}_{(2\text{nm})}$ where $x = 0 - 20\%$ ¹. A schematic of the films is found in Fig. 4.3. Following the design guidelines of Joshi *at al* [1] we choose a thick lower ferromagnetic layer to co-determine the stable domain size in the upper layer, for later MFM studies of the film (see section 3.3.4). This allows exchange coupling a thin film to the CoO antiferromagnet, in turn enabling high resolution measurements which necessitate a small tip to sample distance. The bottom ferromagnet is decoupled from the antiferromagnet by a thin Cu film.

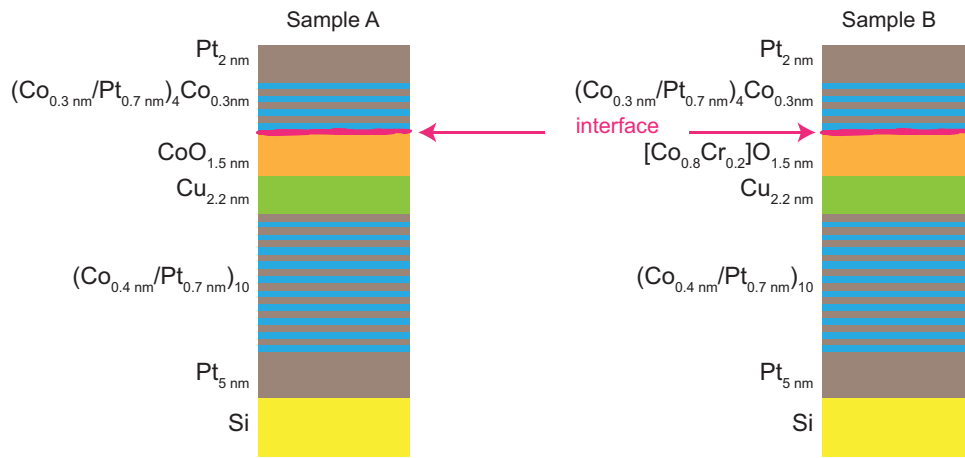


Figure 4.3: Schematic layout of the multilayers of the exchange biased samples used. Both samples have the structure $\text{Si}/\text{Pt}/[\text{CoPt}]_{10}/\text{Cu}/[\text{Co}_{1-x}\text{Cr}_x\text{O}]/[\text{CoPt}]_4/\text{Pt}$. Sample A corresponds to $x = 0$, and sample B corresponds to $x = 20\%$.

The first step in the fabrication process included DC magnetron sputter deposition at RT on native oxide from (001) Si of $\text{Si}/\text{Pt}_{(5\text{nm})}/[\text{Co}_{0.3\text{nm}}\text{Pt}_{0.7\text{nm}}]_{10}/\text{Cu}(2.2\text{nm})/[\text{Co}_{(1-x)}\text{Cr}_{(x)}]_{(1.5\text{nm})}$. Next, the films were annealed in-situ at 150°C to drive Cr to the grain boundaries of the upper Co-layer. A control sample was also fabricated that skipped this step. A subsequent exposure to ambient air for 10 minutes led to the oxidation of the Co-Cr layer, resulting in an antiferromagnet with different degrees of inter-granular coupling. In a fourth step the remaining multilayer structure was magnetron sputtered directly onto the oxidized layer.

The structures were characterized magnetically with VSM at different temperatures. In the following we discuss the results obtained.

4.2.1 Magnetometry of EB-samples with AF grain decoupling

Figure 4.4 (a) shows hysteresis loops of a structure “Sample A, $\text{Si}/\text{Pt}_{(5\text{nm})}/[\text{Co}_{0.3\text{nm}}\text{Pt}_{0.7\text{nm}}]_{10}/\text{Cu}(2.2\text{nm})/\text{CoO}_{(\approx 1.5\text{nm})}/[\text{Co}_{0.3\text{nm}}\text{Pt}_{0.7\text{nm}}]_4/\text{Pt}_{(2\text{nm})}$ ”. At room temperature (red curve in Fig. 4.4

¹ x given in volume concentration.

Layer	$\mu_0 H_c^-$	$\mu_0 H_c^+$	$\mu_0 H_c = \frac{1}{2}\mu_0(H_c^- + H_c^+)$	$\mu_0 H_{eb} = \frac{1}{2}\mu_0(H_c^- - H_c^+)$
Sample-A, Top	-395 mT	220 mT	307.5 mT	87.5 mT
Sample-A, Bottom	-54 mT	54 mT	54 mT	0
Sample-B, Top	-405 mT	156 mT	280.5 mT	124.5 mT
Sample-B, Bottom	-54 mT	54 mT	54 mT	0

Table 4.1: 7.9 K switching fields for 2 T field-cooled samples A (no Cr in the CoO) and B (CoO grain decoupling with CrO).

(a)) the loop looks like typical perpendicular magnetization hysteresis. It is symmetric in the field, i.e. it has no exchange bias, consistent with fact that the Néel temperature of CoO is below room temperature ($T_N \approx 290\text{K}$) [9]. Likewise, structure “Sample B, Si/Pt_(5nm)/[Co_{0.3nm}Pt_{0.7nm}]₁₀/Cu(2.2nm)/[Co_{0.8}Cr_{0.2}O]_(≈1.5nm)/[Co_{0.3nm}Pt_{0.7nm}]₄/Pt_(2nm)” shows no exchange bias at room temperature (red curve in Fig. 4.4 (b)). In both samples the thick lower and thin upper ferromagnetic layers switch at roughly the same field level, and the coercivity is $H_c \simeq 10\text{mT}$.

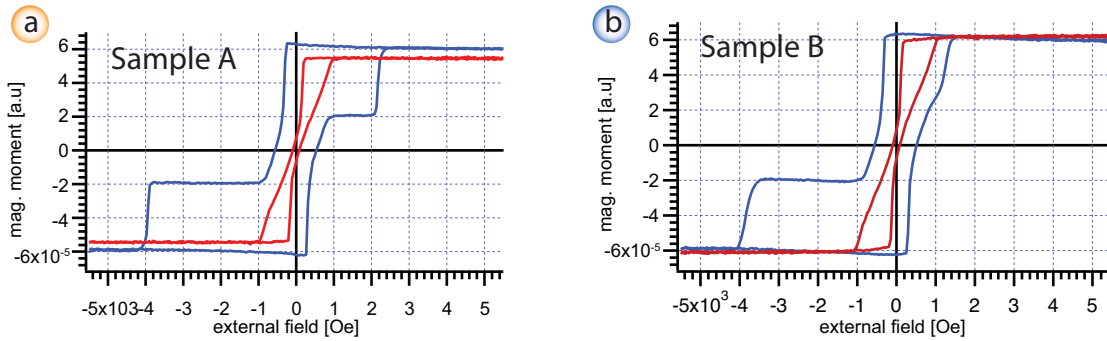


Figure 4.4: Magnetometry of exchange bias samples at room temperature and 7.9 K. (a) sample A (CoO antiferromagnet). (b) Sample B (grain-boundary engineered CoO).

At 7.9 K measurements performed after cooling in an applied field are given in the blue curves of Figures 4.4 (a) and (b). Having been taken below the blocking temperature $T_B < T_N$, the loops are not symmetric. Two reversal processes of different amplitude are seen to occur in each sample at different field levels. A first switch is apparent at low fields. This is the reversal of the thick bottom layer, and has a correspondingly larger amplitude. As expected, given that it is decoupled from the antiferromagnet by the Cu spacer, this switch is symmetric in the field, i.e. there is no exchange bias, regardless of the temperature.

The other switching event occurs at a larger field and is laterally shifted to negative fields. This is the exchange biased loop of the thin upper layer, which is coupled to the antiferromagnet.

An account of the switching fields of both loops can be seen in Table 4.1. Focusing on the top ferromagnetic layer in the samples, i.e. the one coupled to the antiferromagnet, it is clear that sample B has a smaller coercivity and a larger exchange bias. As control experiment, a sample comprising a Cr-oxide interface between F and AF was fabricated, which shows no exchange

bias upon field cooling. Likewise if the Co-Cr alloy layer is not annealed prior to oxidation its exchange bias does not differ noticeably from that of a structure lacking Cr in the AF. These observations indicate that the annealing effectively drives Cr to the grain boundaries, where it decouples the Co grains. The subsequent oxidation process modifies the exchange bias behavior not by coupling to Cr-oxide but in the intended fashion, through decoupling the AF grains.

4.2.2 Microscopic consequences of inter-grain decoupling: MFM results

In the context of our discussion at the beginning of this chapter the increased exchange bias of sample B vis-à-vis sample A, but also the smaller coercivity in the former, have a microscopic origin that can be accessed with MFM. Leaning on the work by Schmid *at al* [15] we follow the evolution of zero-field cooled ferromagnetic domains in an applied field.

$1\mu\text{m} \times 1\mu\text{m}$ -images obtained after cooling in zero field to 8.3 K (Figures 4.5) allow us to compare sample B and sample A with a resolution comparable to the grain size in the material. Maze patterns of perpendicular magnetization are found for both sample A and sample B. We analyze their evolution in different applied fields below. For convenience, we have subtracted the topography-induced contrast from the images in Fig. 4.5, following the procedure outlined in section 3.3.2. All measurements were carried out at a tip-sample distance of 17 nm.

Figures 4.5 (a) show the domain pattern at +150 mT applied field, where the “+” sign indicates the field and the magnetization over the dark domains is aligned parallel for both sample A and B, respectively. Recalling the hysteresis loops at 8.3 K (Fig 4.4, blue curves), we see that at fields greater than 150 mT the bottom layer is aligned with the field, i.e. saturated. Consequently the observed pattern corresponds to the magnetization of the upper layer. Thus an applied positive field of +150 mT already has the dark upper layer domains stably aligned. The light upper layer domains on the other hand, see a field applied opposite to its magnetization direction, but feel the stabilizing effect of antiparallel coupling to pinned uncompensated moment pointing in the “+” direction.

Figures 4.5 shows the evolution of the domains in fields increasing from +150 mT to +500 mT. In the case of sample A, the width of the white domains shrinks considerably in a field of 300 mT. At 325 mT the white domains break-up into smaller pieces, some of which remain stable up to 350 mT.

Sample B shows a similar behavior, i.e. a narrowing of the domains followed by the breaking-up into smaller pieces. However the breaking-up and extinction of the white domains occur in much higher fields, namely 375 mT and 395 mT compared to 300 mT and 350 mT for sample A.

Recovery of the original domain structure of the top ferromagnet after saturation can be seen in Fig. 4.6. This phenomenon has been noted before Kappenberger *at al.* [13], but comparing sample A with B, we can gain further insight into the importance of the local coupling in the stabilization of ferromagnetic domains. Figure 4.6 (d) is an almost flawless match to Fig. 4.6 (c), whereas Fig. 4.6 (b) matches (a) in most but not all domain features.

These observations are consistent with our understanding of the role of inter-granular AF-coupling in the level of F/AF coupling frustration. In this view, broader anti-biasing F/AF interface areas in sample A mean a shallower energy minimum for a given domain configuration -such as the initial one - as well as a multiplicity of similarly stable domain structures. Consequently, the shape of the domain structure at a given field level returning from saturation is not uniquely determined, and we see some discrepancies between Fig. 4.6 (a) and (c).

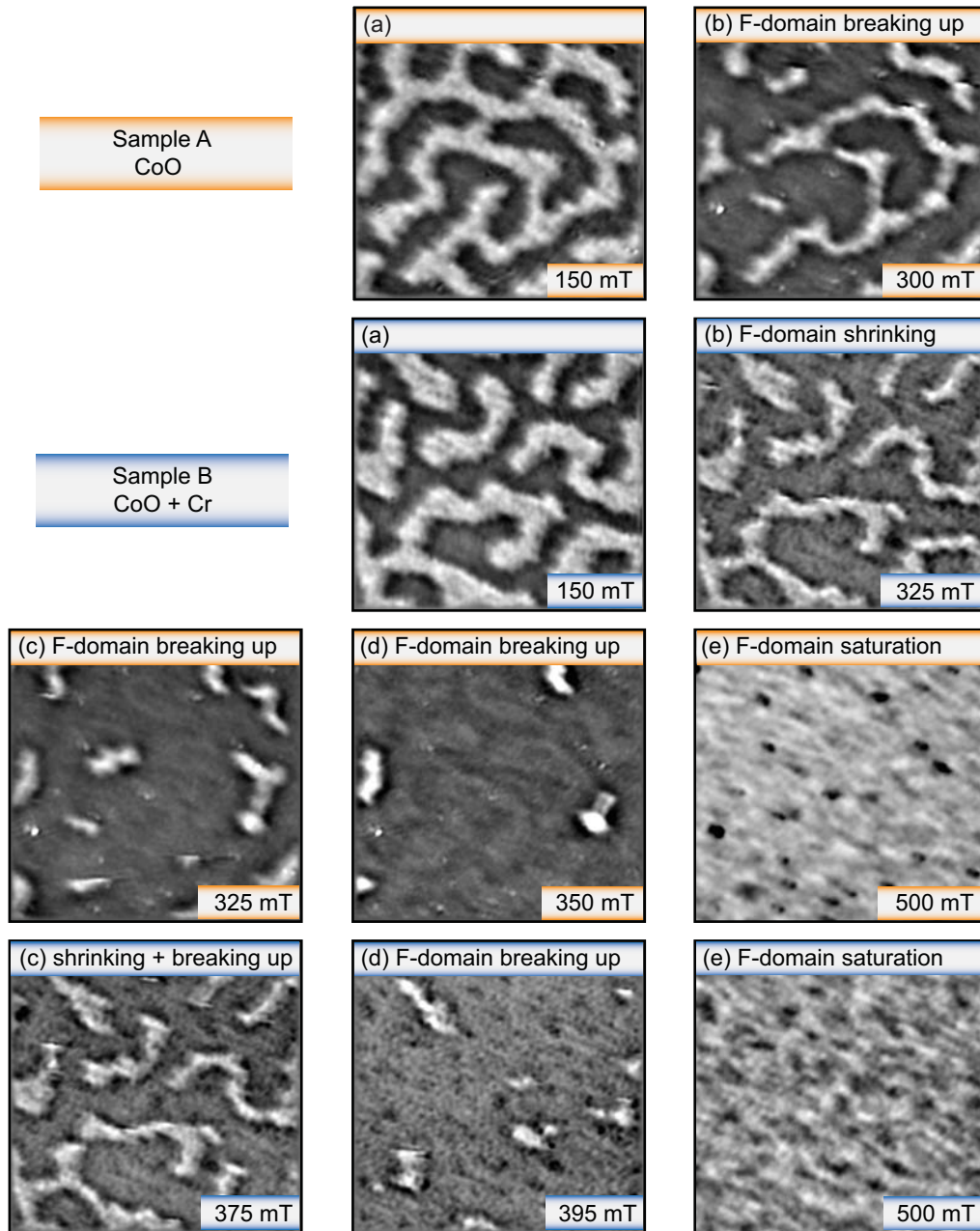


Figure 4.5: MFM measurements of $1 \times 1 \mu\text{m}^2$ areas of sample A and B. The measurements were taken up to saturation, and record first the shrinking of the light domains, then their break up, then their disappearance. For sample B these processes occur at higher applied fields.

4.2.3 Pinned uncompensated spin distribution in AF with decoupled grains

Magnetometry (Fig. 4.4) revealed that the decoupling of the AF grains enhance the EB-field by 42% while the coercivity was reduced by 10%. The evaluation of the F-domains in applied field

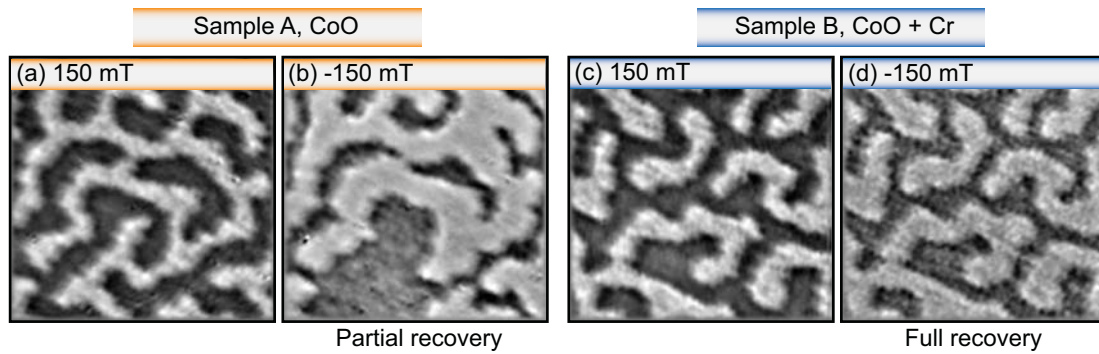


Figure 4.6: MFM study of the recovery of the initial domains' structure after saturation. (a) Initial top-layer (coercivity of bottom layer is smaller than 150 mT) domain configuration in sample A. (b) Partial recovery at -150 mT (negative saturation of the bottom ferromagnet). (c) Initial top-layer domain configuration in sample B. (d) Near perfect recovery at -150 mT.

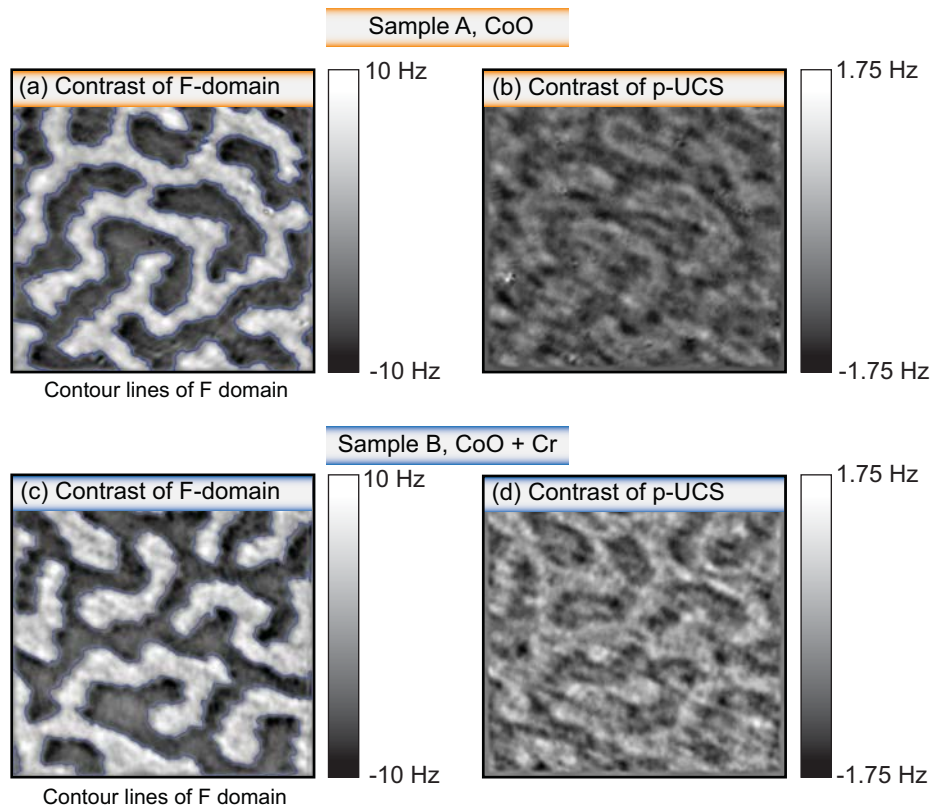


Figure 4.7: Calculation of the local density pinned AF moment for samples A and B. In (a) and (c), contrast generated by the F-domain pattern of the upper F-layer, and in (b) and (d) by the imprinted pinned uncompensated moments.

confirms these findings qualitatively. We can put the above observations in quantitative terms by computing the local density of pinned uncompensated spins for samples A and B. Here we use the method, discussed in section 3.3.6 for which the calibration of the tip response is not required.

The frequency shift image arising from the imprinted pinned uncompensated moments are calculated from the semi-difference of MFM data recorded in positive and negative saturation (see section 3.3.2). Fig. 4.7 shows the frequency shift patterns generated by the F-domain pattern of the upper F-layer (Fig. 4.7 (a) and (c)), and by the imprinted pinned uncompensated moments (Fig. 4.7 (b) and (d)) for sample A and B respectively.

The average areal density of the pinned uncompensated moment (but not the local values) is found by comparing the average up/down frequency shift contrast of the MFM images of the F-domains (Fig. 4.7 (a)), and the imprinted pinned uncompensated pattern (Fig. 4.7 (b)). Using Eqn. 3.2 and the average k -values from the average domain sizes $k = \frac{2\pi}{\lambda}$ with $\lambda_{SampleA} = 230.05$ nm and $\lambda_{SampleB} = 232.4$ nm. We find the average pinned uncompensated moment density 1.661×10^{-4} Am²/m² for sample A and 2.353×10^{-4} Am²/m² sample B, respectively. The increase of the average pinned UCS density of 41.7% corresponds well to the increase of 42% of the EB-field determined from magnetometry. Fig. 4.8 shows the imprinted pinned UCS

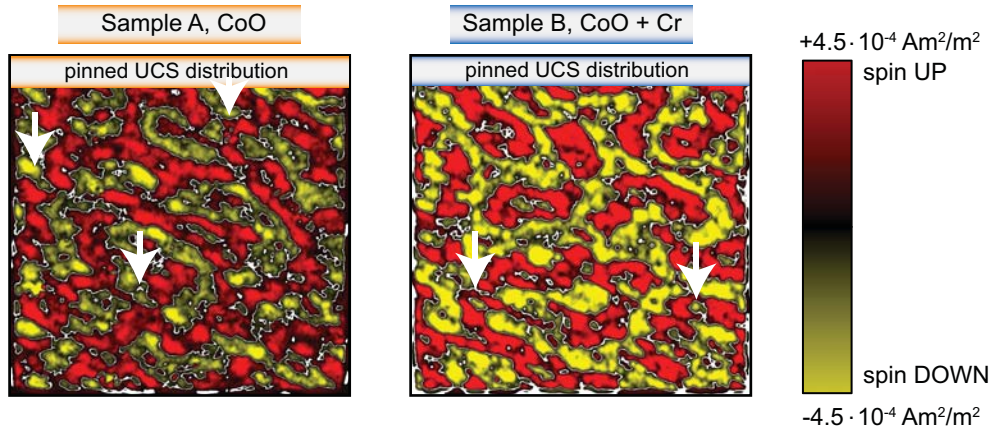


Figure 4.8: Imprinted pinned UCS is color coded in shades of red and yellow for each orientation.

color coded to represent $\pm 36.91\%$ and $\pm 46.98\%$ of a monolayer of UCS for sample A and B. The map of sample B is clearly more homogeneous. This indicates that part of the frustration arising from inter-granular coupling in the AF-layer and consequently less anti-biasing areas exist. It is also interesting that when the interrupted domains is compared with structure of uncompensated spin density pattern, the zones of rupture is looks like the areas corresponding to the anti-biasing areas in the uncompensated moment distribution (white arrows in Fig. 4.8).

4.3 Conclusions

As indicated in many models for the EB-effect frustration plays an important role in EB systems. Based on our prior results on the domain evolution over a pattern of pinned uncompensated spins, that revealed locations with an anti-biasing effect, we concluded that inter-granular coupling

inside the AF-layer may contribute part of the frustration. Consequently the breaking of the intergranular exchange is expected to improve the EB-effect. In order to test this hypothesis, we have used grain-boundary engineering techniques often used to exchange-decouple grains in ferromagnetic data storage media, to decouple grains in the AF-layer. A macroscopic increase of the exchange bias field by 42% and a decrease of the coercive field by 10% was observed. MFM was again used to for the microscopic analysis of the domain evolution and to image and quantify the patterns of imprinted pinned UCS. In the sample with the decoupled AF-grains, an increase of the averaged pinned UCS density of 41% was found, which agrees well with the 42% increase of EB field found by magnetometry. Moreover, the pattern of imprinted UCS was considerably more homogeneous explaining the more robust and reproducible domain evolution in applied fields.

Chapter 5

Giant Exchange Bias: beyond 1 Tesla

A fundamental cause for this weakness of the coupling between ferro- and antiferromagnet and the EB-effect arising from it is coupling frustration at the F/AF interface. It arises because interfacial AF atoms of opposite magnetic moment couple to the F moment orientation parallel and antiparallel respectively: Due to crystallographic orientation of the interface, topography [17], reconstruction or chemical intermixing occurring at the interface [67] the oppositely magnetized AF sub-lattices largely compensate each other's coupling across the interface. A microscopic study of the interface moment orientation in relation to F domain evolution showed that the effective coupling is roughly proportional [15] to a small [68] number of uncompensated AF moments which are pinned (see Chapter 4). Defects have been engineered in the AF to slightly increase this number [30, 56, 69] and the effect of breaking the intergranular exchange in the AF-layer on the EB-effect has been studied (see Chapter 4), but to-date EB fields remain far below intrinsic, atomic-scale exchange coupling fields.

In this chapter, we will demonstrate that much stronger EB-effect and exchange coupling is obtained, when the antiferromagnet is replaced by a rare-earth ferrimagnet. Amorphous rare earth-based ferrimagnets resemble antiferromagnets in that the moments of the constituting rare-earth and transition metal atoms are antiparallel. Their contribution to the total moment is compensated macroscopically at the so-called compensation temperature, T_{comp} . Their orientation at the interface would have a similar degree of compensation as in antiferromagnets. However, the opposite rare-earth and 3d-element moments are expected to couple antiparallel and parallel to the moments of an adjacent ferromagnet, respectively. Frustration-less coupling should result [70], in the sense that the coupling should resemble in its strength what would be expected from fully uncompensated AF interfaces. Hence, a strong EB-effect is expected provided the ferrimagnet does exhibit a sufficiently high coercivity.

5.1 Tb₂₃Fe₇₇ based Thin Film Structures

We fabricated two Tb₂₃Fe₇₇-based thin-film structures: a 40 nm-thick TbFe ferrimagnetic layer (sample 1 in Fig. 5.1) to characterize magnetically the ferrimagnet, and a ferrimagnet-ferromagnet bilayer (sample 2 in Fig. 5.1) to investigate the ferro/ferrimagnet coupling and EB-effect. TbFe-based multilayer structures [71] are prepared by DC magnetron sputter deposition at room temperature, using Ar gas at 1.8×10^{-3} mbar for Co and Pt deposition and 5×10^{-3} mbar for TbFe. The system's base pressure is 10^{-9} mbar. Structural characterization was done with

transmission electron microscopy (TEM). The ferrimagnet composition is altered from the target's composition, and measured by Rutherford backscattering (RBS) to be $\text{Tb}_{23}\text{Fe}_{77}$.

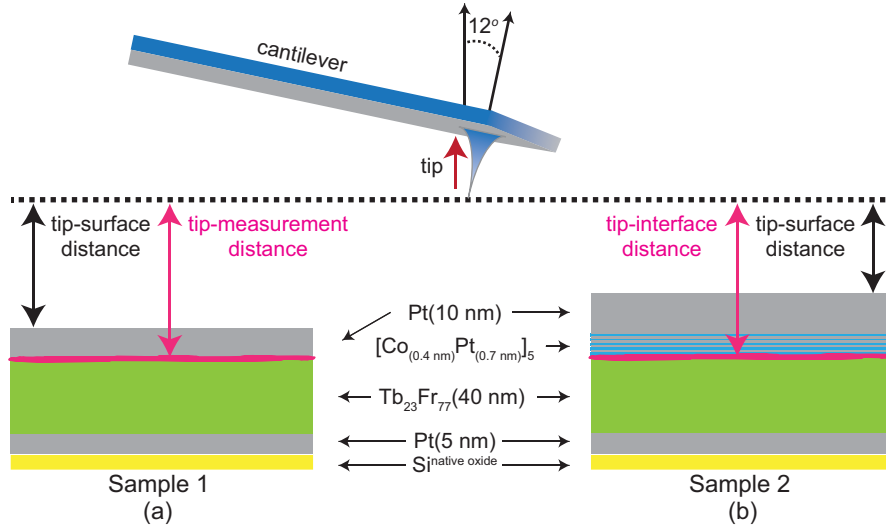


Figure 5.1: Schematic structure of Sample 1 in (a) and Sample 2 in (b).

We designed TbFe/CoPt structure to investigate the microscopic aspects of the magnetization switching in ferrimagnetic/ferromagnetic systems with MFM. The thin Co/Pt multilayer is on top of the ferrimagnet, so we can scan close enough to the ferrimagnet/ferromagnet interface to warrant 20 nm resolution [15, 44, 1].

5.1.1 Macroscopic characterization of $\text{Tb}_{23}\text{Fe}_{77}$ -based thin-film structures

The basic features of the magnetization can be best characterized macroscopically by magnetometry. We use a vibrating sample magnetometer of a Physical Property Measurement System from Quantum Design, with maximum applied field of ± 7 T. For sample 1 Fig. 5.2 shows the remanent magnetic moment areal density, $\tilde{m}_r^{\text{TbFe}}$, and the coercivity $\mu_0 H_c^{\text{TbFe}}$. At low temperatures, the coercivity $\mu_0 H_c^{\text{TbFe}}$ decreases with raising temperature and reaches a minimum of 3 T at 230 K. Above 230 K, the coercivity increases toward its divergence at T_{comp} . Note that the remanence (and also the saturation magnetization) is monotonically decreasing with temperature up until room temperature, as apparent from Fig. 5.2. Extrapolation to zero remanence allows the determination of the compensation temperature T_{comp} to 330 K.

Extrapolating H_c^{TbFe} from higher temperatures to lower ones gives $\mu_0 H_c^{\text{TbFe}}(7.9 \text{ K}) \approx 8.4$ T, which is larger than the maximum field attainable with our magnetometer, 7 T. The inset shows hysteresis loops at 280 K and 50 K that are typical for perpendicular magnetic anisotropy, with a high-field part suggesting that a stratum of the sample may not be fully perpendicular. The relative moment direction and qualitative size of the film's Tb and Fe moments on either extreme of the temperature scale are illustrated schematically at lower right and upper left of the Fig. 5.2. We evaluate H_c^{TbFe} directly from Fig. 5.2, and estimate a lower bound for the uniaxial anisotropy from

$$K_u^{est} = 2\mu_0 M_s^{\text{TbFe}} H_c^{\text{TbFe}}. \quad (5.1)$$

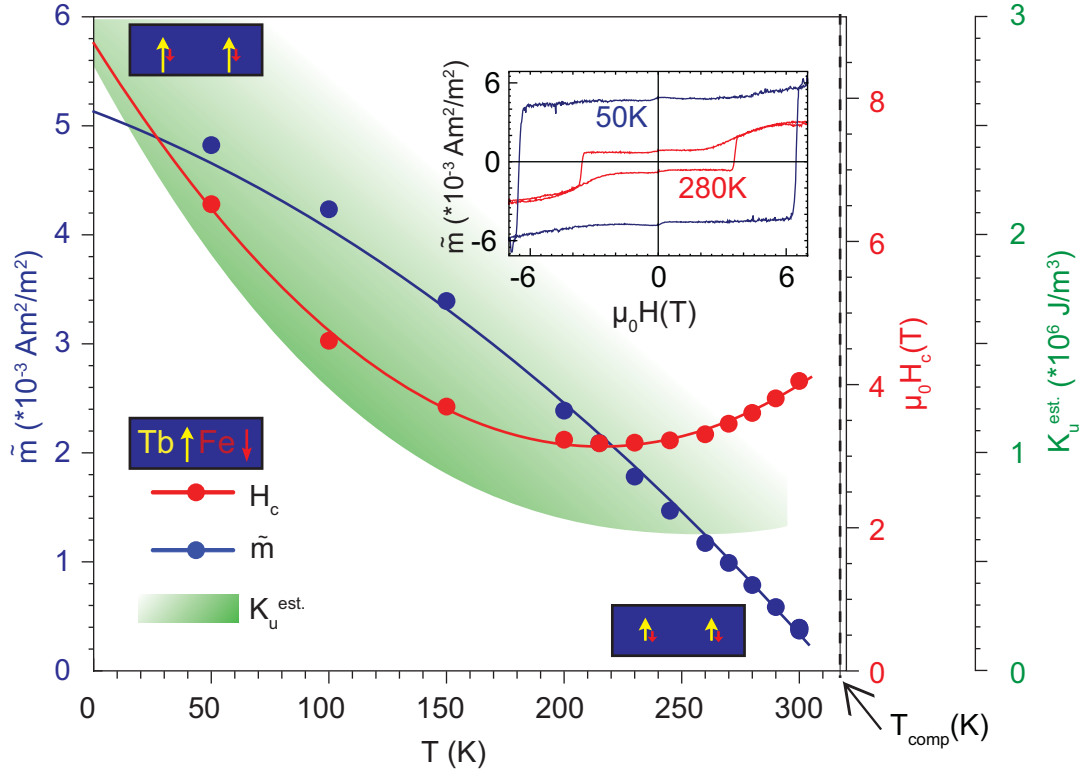


Figure 5.2: Vibrating sample magnetometry results of the ferrimagnet, sample 1. In blue: magnetic moment per unit area, \tilde{m} . Below the compensation temperature $T_{comp} \approx 330 \pm 5$ K, Tb dominates the magnetization. In red: coercivity. Green shaded area: estimated range for the perpendicular anisotropy. Lower right schematic: the film's Tb and Fe moments illustrate the relative moment direction and qualitative size on either extreme of the temperature scale. Inset upper right: Hysteresis loops acquired at 50 K and 280 K.

The range of anisotropies found in this way covers the shaded area in Fig. 5.2, and in particular $K_u^{est}(7.9 \text{ K}) = 2.6 \times 10^6 \text{ J/m}^3$ is consistent with reported room temperature values [72].

Because of the large coercivity of the ferrimagnet, in a structure like sample 2 a coupling between the ferrimagnetic and ferromagnetic layers could lead to a giant unidirectional anisotropy in the latter. We assess this with hysteresis loops from sample 2 after cooling from room temperature to 7.9 K in +7 T, Fig. 5.3. At the selected temperature we carry out the loops by lowering the field from $\mu_0 H = +7$ T down to a minimum field $\mu_0 H_{min}$ and increasing it back to +7 T. $\mu_0 H_{min}$ chosen as $\mu_0 H_{min} > -\mu_0 H_c^{TbFe}$ to avoid switching the ferrimagnet and is determined by temperature dependence of the magnetization of the ferrimagnet (Fig. 5.2). In the 280 K measurement (red curve) we observe a minor hysteresis loop at about +0.7 T. It spans a step in the magnetization matching twice the Co/Pt multilayer saturation magnetization, so we identify the minor loop as the exchange-biased switching of the ferromagnet. Below +0.7 T, and particularly in zero field the Co/Pt magnetization is antiparallel to the net magnetization of the ferrimagnet. This is because below the compensation temperature ($T_{comp} \approx 330$) the Tb moment dominates in the ferrimagnet, Co/Pt couples antiferromagnetically to the Tb moments and ferromagneti-

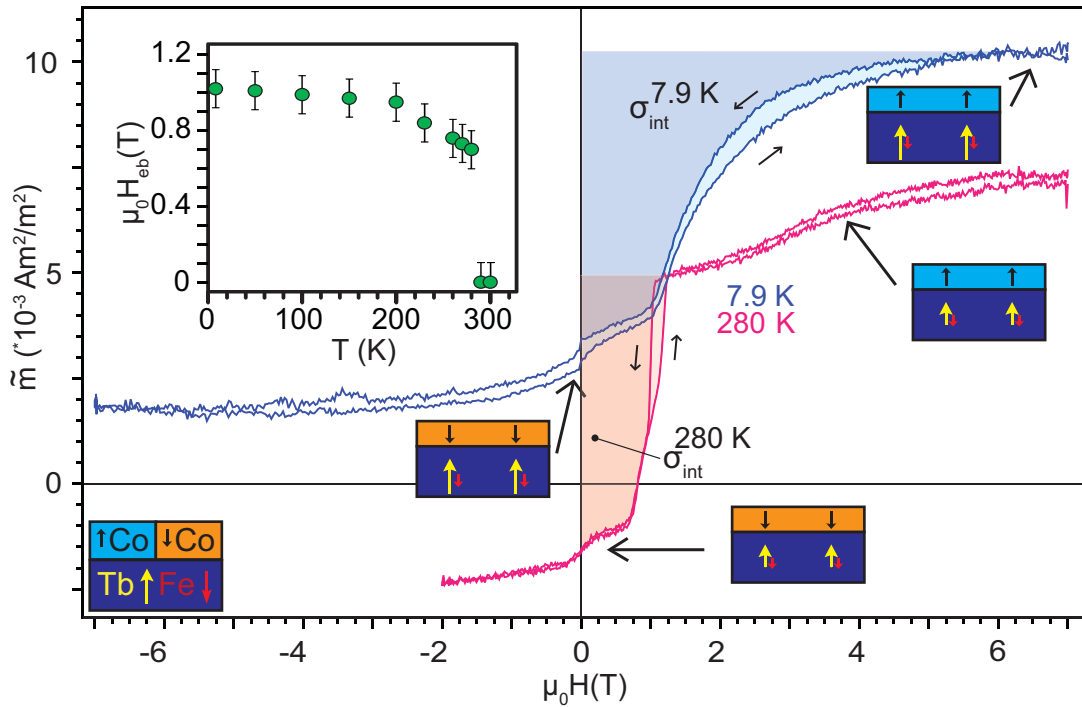


Figure 5.3: Magnetometry of the ferromagnet/ferrimagnet bilayer, sample 2. At applied fields of 1 T the 7.9 K hysteresis loop (blue curve) displays a switching process corresponding to the ferromagnet, which is thus exchange-biased. At 280 K the corresponding exchange-bias amounts to 0.8 T (red curve). The shaded areas represent the energy required in the switching, with the average termed $\sigma_{int}^{7.9 K}$ and $\sigma_{int}^{280 K}$ at 7.9 K and 280 K respectively. Inset diagrams indicate the relative magnetic moment orientation of the different elements in the bilayer. The exchange-bias as a function of temperature, obtained from hysteresis loops such as the ones plotted here is given in the upper left inset

cally to the Fe moments. Additional insight into the origin of the magnetization in this system can be gained from the remanent value of the magnetization. It is negative at 280 K, indicating that the Co/Pt magnetization, oriented in the negative direction, is larger in absolute value than the net magnetization of the ferrimagnet, which is positive, ($-M_{Co} - M_{Fe} + M_{Tb} < 0$). At 7.9 K the magnetization of the ferrimagnet dominates that of the ferromagnet (blue curve in Fig. 5.3), where the remanence is positive, ($-M_{Co} - M_{Fe} + M_{Tb} > 0$). It reflects the substantial increase of the Tb moment at lower temperatures. Small inset bilayer diagrams in Fig. 5.3 illustrate these observations.

Interestingly, at 7.9 K the Co/Pt switching process is shifted laterally to +1.0 T, in what amounts to an exchange-bias increase of 40% vis-à-vis the 280 K result. Between 7.9 K and 280 K we can see the temperature dependence of the exchange-bias in the inset of Fig. 5.3. The values attained are large, but the pronounced increase with decreasing temperature that is commonly observed in antiferromagnet-based exchange-bias systems is absent.

This suggests a difference between the biasing mechanism in antiferromagnet-based and

in ferrimagnet-based systems. In the former a net coupling between the ferromagnet and the antiferromagnet is possible because of uncompensation in the antiferromagnet magnetic moment orientation at the interface, i.e. there exist some uncompensated spins. But the net coupling results in bias only to the extent that these uncompensated spins remain pinned. This is a temperature dependent process, which is believed to be thermally activated [73] – hence the increase of H_{eb} with decreasing T .

In contrast, the coupling between the ferrimagnet and ferromagnet does not depend on the existence of uncompensated spins. Frustration effects should not occur, and the order of the ferrimagnet would therefore not be perturbed (locally) by it. Accordingly, pinning of the ferrimagnet moments should be given by bulk coercivity mechanisms. These we showed in Fig. 5.2 to be large. The observed weak temperature dependence of the exchange-bias effect thus follows from the mechanism that causes it. The inter-layer coupling energy can be estimated from the area enclosed between the loop and the vertical axis of Fig. 5.3: $\sigma_{int}^{280K} = (0.006 \pm 0.001)$ J/m² at 280 K and $\sigma_{int}^{7.9K} = (0.014 \pm 0.001)$ J/m² at 7.9 K. This is considerably higher than the highest coupling energies reported for commonly used antiferromagnetic materials and comparable to the coupling determined in exchange coupled ferrimagnetic bilayers [70], a further indication that the coupling is not frustrated.

One additional characteristic of the exchange-biased loops reveals an important aspect of the coupling between ferrimagnet and ferromagnet. Specifically, the 7.9 K magnetization curve displays a rather gradual completion of the switching process and little hysteresis, reminiscent of magnetization rotation. For a detailed understanding of the process behind the magnetization reversal we recourse to the microscopic information provided at various applied fields by MFM.

5.1.2 Microscopic characterization of $Tb_{23}Fe_{77}$ -based thin-film structures by MFM

We scanned at 7.9 K, in dynamic mode, and at constant average height (35 nm and 30 nm for sample 1 and sample 2 respectively, to have the same tip-ferrimagnet distance for both samples), which is determined at each applied field point separately. This method has a precision better than 0.5 nm over all MFM data taken on both samples (see section 2.4). In all instances of measurements in applied fields, the MFM tip was magnetized parallel to the applied fields.

We measured two sets of 40 quantitative magnetic force microscopy images for a $2 \times 2 \mu\text{m}^2$ area of sample 1 and of sample 2, both cooled as deposited to 7.92 K. Each image are obtained at various applied field levels from 0 T and to 7 T and back to 0 T (Fig. 5.4). The images show a pattern of domains, colored in levels of blue and yellow, which roughly correspond to net magnetic moment areal densities with orientation up and down, respectively, i.e. parallel and antiparallel tip-sample magnetization. The color mapping is the same for all images.

Fig. 5.4 (a–e) are obtained from sample 1 with a pattern typical of perpendicular magnetization domains. Specifically, there exist yellow and blue domains of a comparable size, the shape of which is stable in fields of up to 7 T, the maximum field that we can apply. This is consistent with ferrimagnetic domains with coercivities exceeding 7 T (Fig. 5.2). The contrast is essentially constant.

In contrast to Sample 1, the correspond images (f–j), obtained for sample 2, have several noteworthy aspects:

- A) Despite the magnetization step in Fig. 5.3, sample 2 resembles sample 1 in that there

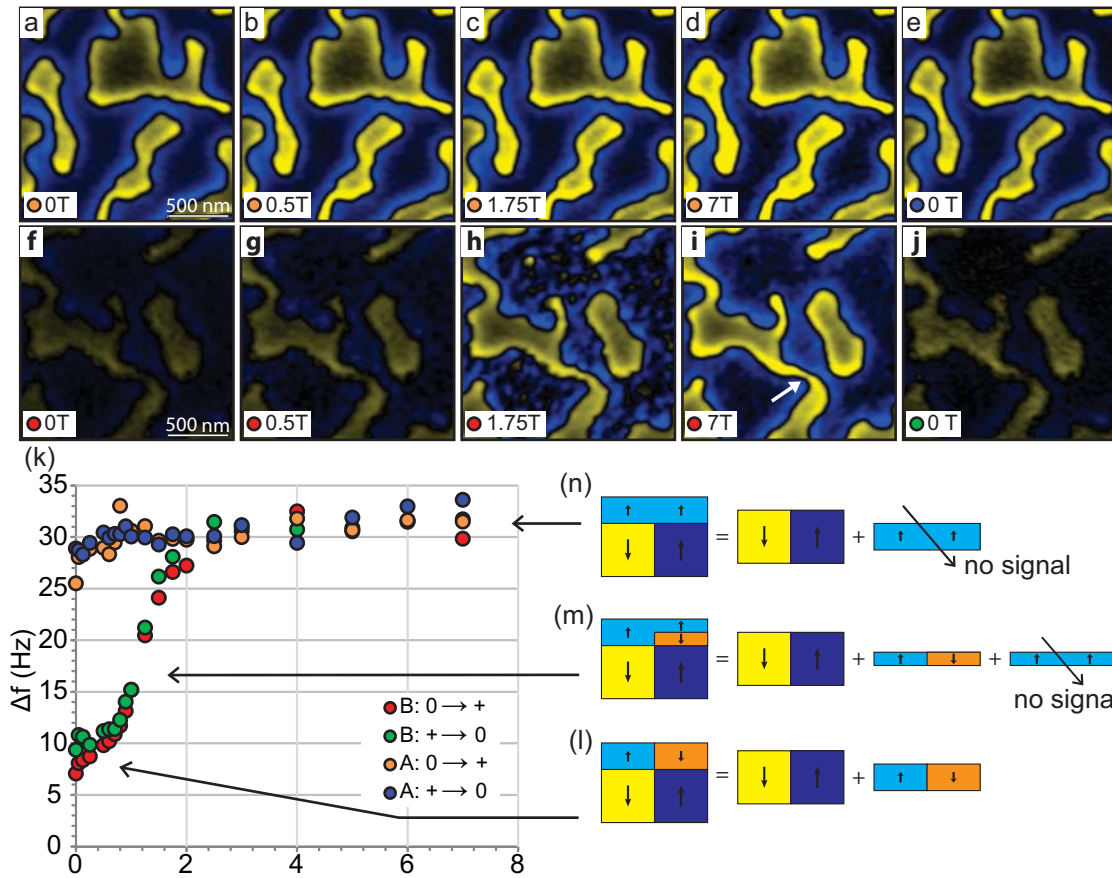


Figure 5.4: Magnetic force microscopy (MFM) characterization RE-ferrimagnet-based exchange bias systems at 7.9 K. (a–e) $2 \times 2 \mu\text{m}^2$ images of sample 1 (ferrimagnet) obtained at 30 nm tip-sample distance at applied fields of 0 T, 0.5 T, 1.75 T and 7 T, with return to 0 T. The shape and contrast of the magnetic domains is essentially constant, indicating that the magnetic structures are stable in applied fields of at least 7 T. (f–j) $2 \times 2 \mu\text{m}^2$ images of sample 2 (ferrimagnet+ferromagnet) obtained at 35 nm tip-sample distance at the same field levels as in (a–e). The initial contrast is much weaker than in (a–e), and increases to these levels for fields $\geq 2\text{T}$. The structures, however, do not change shape as during the magnetization by vertical domain wall motion in perpendicular magnetization systems. (k) Image contrast obtained from the images in (a–j) and other intermediate fields (images not shown). Sample 2 is seen to attain the same contrast level as sample 1 once the ferromagnetic layer has been saturated. The smaller contrast prior to saturation is consistent with the ferromagnet’s antiparallel alignment with the ferrimagnet, which results in a smaller areal density of magnetic moment. (l)–(n) Schematic arrangement of magnetic domains in the bilayer system of sample 2, and the effective portions contributing to the MFM signal. A homogeneously magnetized film layer does not result in stray fields; in particular the saturated ferromagnetic layer is “transparent” to the MFM.

is no lateral (conventional) domain wall motion, which would be clearly visible as an expansion of “blue” and “yellow” areas for increasing and decreasing fields [15], respectively.

The zero-field pattern is almost perfectly retained (see Fig. 5.4 (f-i)), in particular also features as small as 50 nm (indicated by the arrow in Fig. 5.4 (i)).

- B) The image contrast presents three regimes (Fig. 5.4 (k)). First, the contrast of sample 2 in low fields between 0 T and 0.8 T is only 30 % of that of sample 1, but roughly constant (compare the MFM contrast versus field in Fig. 5.4 (k) for sample 1 and sample 2, respectively). Second, for fields between 0.8 T and 3 T the contrast rises continuously for increasing applied magnetic fields, which is recovered upon lowering the field. Having set the tip sample distance to 30.0 ± 0.5 nm for each field level, the contrast of the images can be compared quantitatively, i.e. we can understand the contrast increase to arise from a magnetization pattern that does not change the basic shape but the amplitude. And third, the contrast level obtained in high fields (≈ 3 T to 7 T) remains constant and matches the contrast for sample 1 (see Fig. 5.4 (d-e)).
- C) In decreasing fields the contrast recovers the initial values, apart from a small hysteresis for fields between ≈ 4.5 T and 1.5 T.
- D) In intermediate fields between ≈ 0.8 T and 3 T, a fine sub-domain magnetic structure with dimensions comparable to the 20 nm-wide average Co/Pt grain appears inside the “blue” domains only. Its magnetization is opposite to the applied field, approaching the maximum frequency shift levels at 1.75 T, and disappearing towards to higher fields (7 T). Apart from a small hysteresis this fine structure is mostly reversible (see Fig. 5.5).

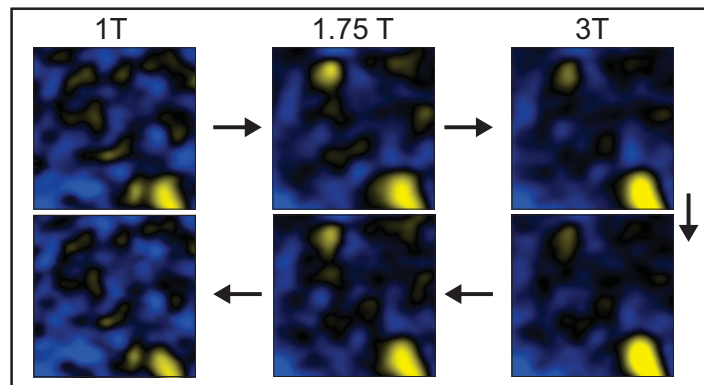


Figure 5.5: MFM of a $500 \text{ nm}^2 \times 500 \text{ nm}^2$ area obtained at 1 T, 1.75 T and 3 T for increasing and then decreasing fields respectively, showing a fine magnetic structure (sample 2).

Point A) confirms that Co/Pt switches with the field by forming an in-plane 180° -domain wall over the “blue” domains, where the CoPt moments were initially antiparallel to the field. Their initial orientation also explains the first regime in B) (see Fig. 5.3 (l)) in terms of a lower net areal magnetic moment density than for sample 1. Consistent with the second regime, as the in-plane domain wall moves toward the TbFe-Co/Pt interface driven by the field (Fig. 5.3 (m)), an increasing fraction of the CoPt-layer saturates, no longer attenuating the stray field of the TbFe-layer (Fig. 5.3 (n)). When Co/Pt is fully saturated it produces no significant stray field, and the MFM picks up only stray field from TbFe. The contrast of sample 2 must then match

that of sample 1, as we see in the third regime. Without going into a detailed description of the in-plane wall structure, we point out that the high-field contrast from sample 2 would depart measurably from the contrast in sample 1 for walls extending more than ≈ 1 nm beyond the interface into the ferrimagnetic or ferromagnetic layer. It does not: A compressed, high-energy wall is formed at the interface. In the 3rd regime therefore, the horizontal wall is circumscribed to the ferromagnet-ferrimagnet interface's immediate vicinity. In accord with C) and driven by the reduction of the large interfacial energy (cf. $\sigma_{int}^{7.9 K}$, $\sigma_{int}^{280 K}$), the wall retracts from the interface when the field is lowered, and is eventually expelled from Co/Pt, retaining the domains' shape.

Because here a marginal change in the magnetization does not imply a corresponding break of the inter-layer coupling in contrast to the results obtained for ferro/antiferromagnet systems (see Chapters 3, 4 and [15]). We must reassess the significance of the energies $\sigma_{int}^{7.9 K}$ and $\sigma_{int}^{280 K}$ calculated from the loops as a lower bound on the coupling energy.

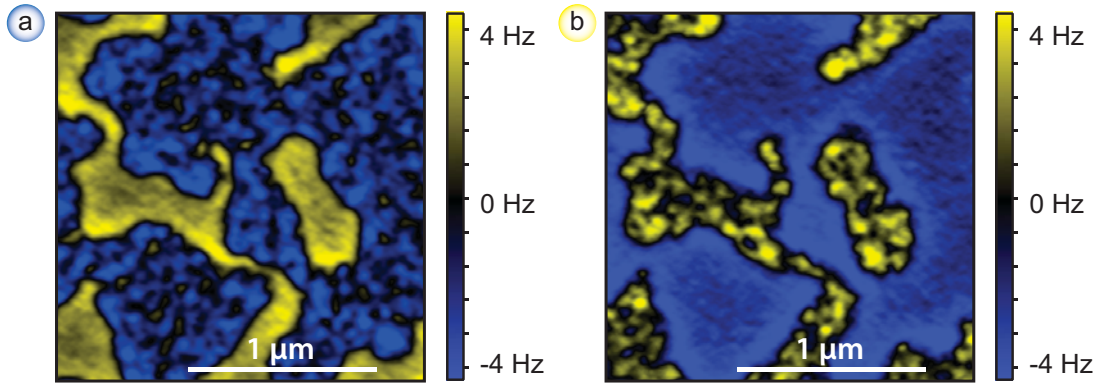


Figure 5.6: Magnetic force microscopy images of the ferrimagnetic/ferromagnetic sample 2. (a) image obtained at +1 T applied field. (b) image obtained at -1 T. The contrast is inverted in (b) to correct a contrast inversion arising from the flipped tip magnetization, and allow a more direct comparison of the images.

The granular sub-domain magnetic structures, point D) deserve a special note (see Fig. 5.5). Their appearance indicates that the formation of the in-plane domain wall and its motion towards the interface is inhomogeneous on the length scale of the grains of the Co/Pt film (see Fig. 5.5). The wall-energy inhomogeneity in Co/Pt may result from its dispersion in grain size, orientation, anisotropy, and inter-granular coupling [74]. Note that these sub-domains appear only inside the blue domain (see Fig. 5.5, and Fig. 5.6 (a)), which has a net magnetization parallel to the tip and hence a Co/Pt magnetization antiparallel to the cooling field and the Tb moment. A sufficiently strong positive field will thus reverse the Co/Pt magnetization only in parts of the sample showing a blue domain. Hence the inhomogeneous propagation of the horizontal domain wall on a length-scale compatible with the grain size of the polycrystalline Co/Pt film, i.e. subdomains are detected in the blue domains only. Fig. 5.6 (a) shows the behavior in negative fields. As expected the Co/Pt magnetization above the yellow domains now shows sub-domains in intermediate fields, while no sub-domains are observed in the blue domains.

5.2 Conclusions

With the above findings in this work, in particular the observation of the formation and propagation of a horizontal domain wall, we suggest that ferro/ferromagnetic bi- or multilayers may also become a viable alternative to contemporary exchange-coupled recording media. It is conceivable to use thin ferromagnetic layers for writing information onto a ferrimagnet via exchange-spring processes. The ferrimagnet provides excellent thermal stability with its high anisotropy and larger thickness, and stable small domains by its relatively low exchange stiffness. The ferromagnetic layer would also amplify the stray fields for the read-head. Note that e.g. by the addition of Co it is possible to increase the compensation and Curie temperature of the TbFe ferrimagnetic films considerably [75]. Conversely, rare-earth ferrimagnets coupled to highly anisotropic ferromagnetic materials could be used for an all-optical recording [76], where the optically driven reversal of the rare-earth could also reverse a highly anisotropic ferromagnetic storage layer via an exchange-spring interaction.

Chapter 6

Conclusions and Outlook

This thesis was devoted to the study of exchange bias system by magnetic force microscopy. My work was inspired by experiments performed within previous thesis of Dr. Iris Schmid and Dr. Peter Kappenberger. Again the MFM work was performed with the UHV LTMFM at the University of Basel, but in contrast to their work all samples studied in my thesis were fabricated at Empa. All samples have been structurally and chemically analyzed and their macroscopic magnetic properties were measured by VSM at Empa. The fabrication of the samples at Empa allowed an optimization of the native domain structure of the sample for subsequent MFM analysis.

Relevant progress was made concerning the understanding of the various contributions of the MFM contrast. From this, the density of pinned uncompensated spins could be determined with high accuracy and other contributions could be ruled out (chapter 3). In all our systems we found a surprisingly high density of imprinted pinned UCS and an antiparallel alignment to the moments of the adjacent ferromagnet. Interestingly our results have been confirmed by XMCD reflectometry and XMCD PEEM experiments, even though earlier experiments with these methods seemed to contradict our findings. The antiferromagnetic coupling between the F-moments and the pinned UCS AF moments may be one of the necessary conditions required for the EB-effect (see final comments in section 3.4). The high density of pinned uncompensated moments seems to be at odds with the weak exchange field, at least if the F/AF interface would be sharp and chemically distinct. So the high density of pinned magnetic moments strongly supports the spin-glass model for the exchange bias effect presumably combined with a domain state which is facilitated by the grain boundaries in our polycrystalline materials. Such a spin-glass state at the F/AF interface could easily explain a high pinned magnetic moment density as well as a weak exchange bias field.

Inspired by the microscopic view on the spatial distribution of the pinned UCS pattern, and the evolution of ferromagnetic domains over this pattern, we came up with a new view on the role of frustration on a length-scale of the size of the grains of the AF. Our hypothesis was that the inter-granular coupling between the AF grains would contribute to the frustration and hence lower the EB effect. Using a strategy well known for magnetically decoupling grains in ferromagnetic polycrystalline materials, we showed that the decoupling of the AF grains enhances the exchange field and lowers the coercivity of the F-layer. Subsequent MFM analysis confirmed that the higher EB field is caused by a stronger and more homogeneous pinned UCS pattern.

This work has further driven us to look for even better solutions to remove frustration. Replacing the antiferromagnet by rare-earth ferrimagnetic materials led to a giant exchange bias effect with exchange fields that can exceed one Tesla! MFM revealed an entirely different magnetization process in exchange bias system that use rare-earth ferrimagnets instead of antiferromagnets. For the first time the formation of high-energy domain walls parallel to the F/ferrimagnet interface could be observed.

Future work will mainly be devote to the continued exploration of exchange bias systems based on rare-earth ferrimagnets. Particular emphasis will be put on the quantitative analysis of the formation and evolution of interfacial domain walls. Further, the potential of these materials for new data storage applications will be explored.

Bibliography

- [1] N. J. Joshi, S. Özer, M. A. Marionni P. G. Sticker, S. Romer, T. V. Ashworth, and H. J. Hug. Engineering the ferromagnetic domain size for optimized imaging the pinned uncompensated spins in exchange-biased samples by magnetic force microscopy. *Appl. Phys. Lett.*, 98(4):082502, 2011.
- [2] Ching Tsang. Magnetics of small magnetoresistive sensors. *J. Appl. Phys.*, 55:2226, 1984.
- [3] C. Tsang, T. Lin, R. E. Fontana, D. E. Heim, V. S. Speriosu, B. A. Gurney, and M. L. Williams. Design, Fabrication and Testing of Spin-Valve Read Heads for High Density Recording. *IEEE Trans. Magn.*, 30(6):3801, 1994.
- [4] D. Lacour, F. Nguyen Van Dau, H. Jaffrés, F. Petroff, and A. Vaurés. Field sensing using the magnetoresistance of IrMn exchange-biased tunnel junctions. *J. Appl. Phys.*, 91:4655, 2002.
- [5] S. S. P. Parkin, K. P. Roche, M. G. Samant, P. M. Rice, and R. B. Beyers. Exchange-biased magnetic tunnel junctions and application to nonvolatile magnetic random access memory. *J. Appl. Phys.*, 85:5828, 1999.
- [6] D.D. Tang, V.S. Speriosu, P.K.Wang, S.Le, and K.K. Kung. Spin-Valve RAM Cell. *IEEE Trans. Magn.*, 31(6):3206, 1995.
- [7] W.H. Meiklejohn and C. P. Bean. New Magnetic Anisotropy. *Phys. Rev.*, 105(3):904–914, 1957.
- [8] W.H. Meiklejohn. Exchange anisotropy - A review. *J. Appl. Phys*, 33:1328, 1962.
- [9] J. Nogues and I. K. Schuller. Exchange Bias. *Journal of MMM.*, 192:203–232, 1999.
- [10] Kentaro Takano and A. E. Berkowitz. Exchange anisotropy * A review. *J. Magn. Magn. Matter.*, 200:552, 1999.
- [11] H. Ohldag, T. J. Regan, J. Stöhr, A. Scholl, F. Nolting, J. Lüning, C. Stamm, S. Anders, and R. L. White. Spectroscopic Identification and Direct Imaging of Interfacial Magnetic Spins. *Phys. Rev. Lett.*, 87(24):247201–4, 2001.
- [12] P. Kappenberger, I. Schmid, and H. J. Hug. Investigation of the exchange bias effect by quantitative magnetic force microscopy. *Adv. Eng. Mater.*, 7(5):332–338, 2005.

- [13] P. Kappenberger, J. B. Kortright, O. Hellwig, Y. Pellmont, S. Martin, Eric E. Fullerton, and H. J. Hug. Direct Imaging and Determination of the Uncompensated Spin Density in Exchange-Biased CoO/CoPt Multilayers. *Physical Review Letters*, 91(26):267202, 2003.
- [14] J. Keller, B. Beschoten, P. Miltenyi, and G. Güntherodt. Domain state model for exchange bias: II. Experiments. *Phys. Rev. B*, (1):014431.
- [15] I. Schmid, M. A. Marionni, and H. J. Hug. Exchange Bias and Domain Evolution at 10 nm Scales. *Phys. Rev. Lett.*, 105:197201, 2010.
- [16] H. Ohldag, F. Nolting, A. Scholl, E. Arenholz, S. Maat, A. T. Young, M. Carey, and J. Stöhr. Correlation between exchange bias and pinned interfacial spins. *Phys. Rev. Lett.*, 91(1):017203, 2003.
- [17] K. Takano, R. H. Kodama, W. Cao, G. Thomas, and A. E. Berkowitz. Interfacial uncompensated antiferromagnetic spins: Role in unidirectional anisotropy in polycrystalline Ni₈₁Fe₁₉ bilayers. *Phys. Rev. Lett.*, 79(6):1130–1133, 1997.
- [18] K. Takano, A. E. Berkowitz, R. H. Kodama, W. Cao, and G. Thomas. Role of interfacial uncompensated antiferromagnetic spins in unidirectional anisotropy in Ni₈₁Fe₁₉ /CoO bilayers. *J. Appl. Phys.*, 83(11):6888, 1998.
- [19] I. Schmid, P. Kappenberger, S. Romer, M. A. Marionni, and H. J. Hug. The role of uncompensated spin in exchange biasing. *Europhys. Lett.*, 81:17 001, 2008.
- [20] T. Eimüller, T. Kato, T. Mizuno, S. Tsunashima, C. Quitmann, T. Ramsvik, S. Iwata, and G. Schütz. Uncompensated spins in a micro-patterned CoFeB/MnIr exchange bias system. *Appl. Phys. Lett.*, (12):2310.
- [21] W.H. Meiklejohn and C. P. Bean. New Magnetic Anisotropy. *Phys. Rev.*, 102:1413–1414, 1956.
- [22] L.Néel. *Ann. Phys.*, 2:61, 1967.
- [23] D. Mauri, H. C. Siegmann, P. S. Bagus, and E. Kay. Simple model for thin ferromagnetic films exchange coupled to an antiferromagnetic substrate. *J. Appl. Phys.*, 62:3047, 1987.
- [24] N. C. Koon. Calculations of Exchange Bias in Thin Films with Ferromagnetic/Antiferromagnetic Interfaces. *Phys. Rev. Lett.*, 78(25):4865, 1997.
- [25] M. Kiwi, J. Mejia-Lopez, R. D. Portugal, and R. Ramirez. Exchange bias model for Fe/FeF₂: Role of domains in the ferromagnet. *Europhys. Lett.*, 48(5):573–579, 1999.
- [26] A. P. Malozemoff. Random-field model of exchange anisotropy at rough ferromagnetic-antiferromagnetic interfaces. *Phys. Rev. B*, 35(7):3679, 1987.
- [27] A. P. Malozemoff. Mechanisms of Exchange Anisotropy. *J. Appl. Phys.*, 63:3874, 1988.
- [28] A. P. Malozemoff. Heisenberg-to-Ising crossover in a random-field model with uniaxial anisotropy. *Phys. Rev. B*, 37:7673, 1988.

- [29] U. Nowak and K. D. Usadel. Structure of domains in random Ising magnets. *Phys. Rev. B*, 46:8329, 1992.
- [30] P. Miltenyi, M. Gierlings, J. Keller, B. Beschoten, G. Güntherodt, U. Nowak, and K. D. Usadel. Diluted Antiferromagnets in Exchange Bias: Proof of the Domain state Model. *Phys. Rev. Lett.*, 84(18):4225, 2000.
- [31] U. Nowak, K. D. Usadel, J. Keller, P. Miltenyi, B. Beschoten, and G. Güntherodt. Domain state model for exchange bias. I. Theory. *Phys. Rev. B*, 66:014430, 2002.
- [32] F. Radu. PhD thesis, Ruhr University - Bochum, Title = Fundamental aspects of exchange bias effect, Year = 2005.
- [33] F. Radu, K. Theis-Brohl, A. Westphalen, and H. Zabel. Quantitative description of the azimuthal dependence of the exchange bias effect. *J. Phys. Condens. Matter*, 18:29–36, 2006.
- [34] H. J. Hug, B. Stiefel, P.J.A. van Schendel, A. Moser, S. Martin, and H.-J. Güntherodt. A low temperature ultrahigh vacuum scanning force microscope. *Rev. Sci. Instrum.*, 70(9):3625–3640, 1999.
- [35] H. J. Hug, A. Moser, T. Jung, O. Fritz, A. Wadas, I. Parashikov, and H.-J. Güntherodt. Low temperature magnetic force microscopy. *Rev. Sci. Instrum.*, 64(10):2920, 1993.
- [36] P. Kappenberger. Exchange bias effect and hard disk media studied by means of quantitative magnetic force microscopy, 2005.
- [37] N. Pilet. The relation Between Magnetic Hysteresis and the Micromagnetic State: Explored by Quantitative Magnetic Force Microscopy, 2006.
- [38] I. Schmid. *The Role of Uncompensated Spins in Exchange Biased Systems*. PhD thesis, Basel University, Basel, 2006.
- [39] C. F. Quate G. Binnig and Ch. Gerber. Low temperature magnetic force microscopy. *Phys. Rev. Lett.*, 56:930, 1986.
- [40] J. J. Saenz, N. Garcia, P. Grütter, E. Meyer, H. Heinzelmann, R. Wiesendanger, L. Rosenthaler, H. R. Hidber, and H.-J. Güntherodt. *Magnetic domain structure by measuring magnetic forces*. 1975.
- [41] D. Rugar, H. J. Mamin, and P. Guethner. Improved fiber-optic interferometer for atomic force microscopy. *Applied Physics Letters*, 55(25):2588, 1989.
- [42] Ch. Loppacher. Nichtkontakt-Rasterkraftmikroskopie mit digitalem Phasenregelkreis, 2000.
- [43] Ch. Loppacher, M. Bammerlin, E. Battiston, M. Guggisberg, D. Müller, H. R. Hidber, R. Lüthi, E. Meyer, and H.-J. Güntherodt. Fast digital electronics for application in dynamic force microscopy using high-Q cantilevers. *Appl. Phys. A*, 66:215, 1998.

- [44] P. J. A. van Schendel, H. J. Hug, B. Stiefel, S. Martin, and H.-J. Güntherodt. A method for the calibration of magnetic force microscopy tips. *Journal of Applied Physics*, 88(1):435–445, 2000.
- [45] M. R. Fitzsimmons, B. J. Kirby, S. Roy, Zhi-Pan Li, I. V. Roshchin, S. K. Sinha, and Ivan K. Schuller. Pinned magnetization in the antiferromagnet and ferromagnet of an exchange bias system. *Phys. Rev. B.*, (1):214412.
- [46] S. Roy, M. R. Fitzsimmons, S. Park, M. Dom. O. Petravic, I. V. Roshchin, Zhi-Pan Li, X. Batlle, R. Morales, A. Misra, X. Zhang, K. Chesnel, J. B. Kortright, S. K. Sinha, and Ivan K. Schuller. Magnetization profile in the MnIr/CoFe exchange bias. *Phys. Rev. Lett.*, page 047201.
- [47] S. Doi, N. Awaji, K. Nomura, T. Hirono, T. Nakamura, and H. Kimura. Magnetization profile in the MnIr/CoFe exchange bias. *Appl. Phys. Lett.*, page 232504.
- [48] E. Goering S. Brück:2008, G. Schütz. Uncompensated moments in the MnPd/Fe exchange bias system. *Phys. Rev. Lett.*, page 126402.
- [49] E. Arenholz, G. van der Laan, R. V. Chopdekar, and Y. Suzuki. Anisotropic x-ray magnetic linear dichroism at the Fe $L_{2,3}$ edges in Fe_3O_4 . *Phys. Rev. B.*, page 094407.
- [50] R. Abrudan, J. Miguel, M. Bernien, C. Tieg, M. Piantek, J. Kirschner, and W. Kuch. Structural and magnetic properties of epitaxial Fe/CoO bilayers on Ag(001). *Phys. Rev. B.*, page 014411.
- [51] E. Blackburn, C. Sanchez-Hanke, S. Roy, D. J. Smith, J. I. Hong, K. T. Chan, A. E. Berkowitz, and S. K. Sinha. Pinned Co moments in a polycrystalline permalloy/CoO exchange-biased bilayer. *Phys. Rev. B.*, 78:180408, 2008.
- [52] F. Offi, W. Kuch, L. I. Chelaru, K. Fukumoto, M. Kotsugi, and J. Kirschner. Induced Fe and Mn magnetic moments in Co-FeMn bilayers on Cu(001). *Phys. Rev. B.*, page 094419.
- [53] S. Foss, R. Proksch, E. D. Dahlberg, B. Moskowitz, and B. Walsh. Localized micromagnetic perturbation of domain walls in magnetite using a magnetic force microscope. *Appl. Phys. Lett.*, (22):3426.
- [54] J. M. D. Coey. *Magnetism and Magnetic Materials*. 2011.
- [55] C. Tieg, E. Jimenez, J. Camarero, J. Vogel, and C. Arm. Imaging and quantifying perpendicular exchange biased systems by soft x-ray holography and spectroscopy. *Appl. Phys. Lett.*, 96:072503, 2010.
- [56] Jung-Il Hong, Titus Leo, David J. Smith, and Ami E. Berkowitz. Enhancing Exchange Bias with Diluted Antiferromagnets. *Phys. Rev. Lett.*, 96:117204, 2006.
- [57] M. F. Doemer, T. Yogi, D. S. Parker, and T. Nguyen. Composition Effects in High Density CoPtCr Media. *IEEE Trans. Magn.*, 29(6):3667, 1993.
- [58] G. Choe. Effect of film morphology on grain boundary segregation induced magnetic properties in heat treated CoCrPt/Cr films. *IEEE Trans. Magn.*, 31(6):2809, 1995.

- [59] K. Tang, M. E. Schabes, C. A. Ross, R. Ranjan L. He, T. Yamashita, and R. Sinclair. Magnetic clusters, intergranular exchange interaction and their microstructural basis in thin film longitudinal media. *IEEE Trans. Magn.*, 33(5):4274, 1997.
- [60] B.G.Demczyk. Oxidation behavior of annealed CoCr thin films. *J. Vac. Sci. Technology A*, 11(4):1458, 1993.
- [61] A. Kohn, J. Dean, A. Kovacs, A. Zeltser, M. J. Carey, D. Geiger, G. Hrkac, T. Schrefl, and D. Allwood. Exchange-bias in amorphous ferromagnetic and polycrystalline antiferromagnetic bilayers: Structural study and micromagnetic modeling. *J. Appl. Phys.*, 109:083924, 2011.
- [62] W. Grooger, K. M. Krishnan, R. A. Ristau, T. Thomson, S. D. Harkness, and R. Ranjan. Quantitative measurement of Cr segregation in $\text{Co}_{0.8-x}\text{Cr}_x\text{Pt}_{0.1}\text{B}_{0.1}$ recording media by scatter diagram analysis. *Appl. Phys. Lett.*, 80(7):1165, 2002.
- [63] G. Choe, M. Zheng, E. N. Abarra, B. G. Demczyk, J. N. Zhou, B. R. Acharya, and K.E. Johnson. High-performance CoPtCrO perpendicular media: optimizing exchange coupling and anisotropy orientation dispersion. *Journal of MMM.*, 287(7):159–166, 2005.
- [64] D. E. Laughlin, N. T. Nuhfer, S. Park, H. Yuan, and J. G. Zhu. Topology and elemental distribution in Co alloy:oxide perpendicular media. *J. Appl. Phys.*, 105:07B739, 2009.
- [65] J. M. MacLaren and S. D. Willoughby. First principles studies of intergrain exchange coupling. *J. Appl. Phys.*, 91(10):8147, 2002.
- [66] S. Y. Hong and T. D. Lee. Enhancement of magnetic properties in CoCrPt longitudinal recording media by $\text{Cr}_{75}\text{Ti}_{25}/\text{CoTi}$ bilayer. *J. Appl. Phys.*, 85(8):4298, 1999.
- [67] F. Allegretti, G. Parteder, M.G. Ramsey, S. Surnev, and F.P. Netzer. The formation of sharp NiO(100)–cobalt interfaces. *Surface Science*, 601:L73–L76, 2007.
- [68] M. Ali, C. H. Marrows, B. J. Hickey, F. Offi, J. Wang, L. I. Chelaru, M. Kotsugi, and W. Kuch. Suppression of magnetization ripple by exchange bias. *Phys. Rev. B*, 79:064415, 2009.
- [69] Dinesh Martien, Kentaro Takano, A. E. Berkowitz, and David J. Smith. Increasing the exchange-bias field of $\text{Ni}_{0.5}\text{Co}_{0.5}\text{O}$ films by microstructural control. *Appl. Phys. Lett.*, 74:1314, 1999.
- [70] C. C. Lin, C. H. Lai, R. F. Jiang, and H.-P. D. Shieh. High interfacial exchange energy in TbFeCo exchange-bias films. *J. Appl. Phys.*, 93:6832–6834, 2003.
- [71] T. Kobayashi, H. Tsuji, S. Tsunashima, and S. Uchiyama. Magnetization Process of Exchange-Coupled Ferrimagnetic Double-Layered Films. *Jpn. J. Appl. Phys.*, 20:2089–2095, 1981.
- [72] R. B. van Dover, M. Hong, E. M. Gyorgy, J. F. Dillon, and S. D. Alibiston. *J. Appl. Phys.*, page 3897–3899.

- [73] X. Portier, A. K. Petford-Long, A. de Morais, N. W. Owen, and H. Laidler. Magnetization reversal processes in exchange-biased systems. *J. Appl. Phys.*, 87:6412, 2000.
- [74] S. M. Watson, T. Hauet, J. A. Borchers, S. Mangin, and E. E. Fullerton. Interfacial magnetic domain wall formation in perpendicular-anisotropy exchange-spring films. *Appl. Phys. Lett.*, 92:202507, 2008.
- [75] Y. Mimura, N. Imamura, T. Kobayashi, A. Okada, and Y. Koshiro. Magnetic properties of amorphous alloy films of Fe with Gd, Tb, Dy, Ho, or Er. *J. Appl. Phys.*, 49:1208–1215, 1978.
- [76] C. D. Stanciu, F. Hansteen, A. V. Kimel, A. Kirilyuk, A. Tsukamoto, A. Itoh, and Th. Rasing. All-Optical Magnetic Recording with Circularly Polarized Light. *Phys. Rev. Lett.*, page 047601.

List of Figures

1.1	Phenomenological model of exchange bias for an F/AF bilayer. Indicated places in the hysteresis loop shows the corresponding magnetic moment configuration. In (a) the magnetic moment configuration at a temperature which is higher than T_N and smaller than T_C . AF-layer is in paramagnetic state while F-layer is ordered. (b) is the state after cooling the system below T_N , assuming a ferromagnetic coupling of AF and F moments at the interface due to the uncompensated moments at the interface. (c) Reversing the field starts to rotate the F moments but not the AF's. (d) the F magnetization has been completely reversed. (e) Reverse back the field into original direction will start to rotate F moments at smaller field. This appears as a shift in the field axis of the M-H loop.	4
1.2	Schematics diagram of angles and vectors involved in Meiklejohn and Bean model. Note that the F and AF anisotropy axis (K_F and K_{AF}) are assumed to be collinear and that the AF sub-lattice magnetization M_{AF} has two opposite directions. . .	5
1.3	Mauri-Siegmann model of exchange bias. F film of thickness t_F is separated by and interface of thickness ξ from a thick AF. The uniaxial anisotropy of the AF is along z , and there is parallel coupling between the uncompensated interfacial moments and the F moments. The external field is applied at an angle β with respect to z and the F moments are aligned parallel to H . Near the interface the AF axis may rotate and form a domain wall. The rotation of the AF axis is given by $\alpha \leq \beta$, and depends on the magnetocrystalline anisotropy of AF [23].	6
1.4	Schematic view of the vertical domain wall in AF layer (a), it appears as energetically favourable state of F/AF systems with rough interfaces. (b) schematic side view of the F/AF bilayer with a ferromagnetic wall driven by an applied field H .	7
1.5	Schematic of Takano model: (a) shows a schematic of the interface cross section of an AF grain. \vec{n} is the film normal, and \vec{p} is the normal to the parallel [111] spin planes of AF. (b) shows a topographical representation of the interfacial plane as shown in (a) with a sampling region representing a model crystallite. (c) shows the elliptical "islands" of monoatomic layer thickness which were superimposed on the spin map to simulate roughness. Note that adding one atomic layer reverses the direction of the underlying spin.	9
1.6	Sketch of the model with one F layer, and three diluted AF layers in (a). The dots mark defects. (b) shows the schematic illustration of the Imry-Ma argument.	10

1.7	Schematic view of the F/AF moment arrangement in the spin glass model. At the interface between the F and AF layers, the AF anisotropy is assumed to be the reduced. It has two types of AF uncompensated moments which are frozen and rotatable ones.	11
2.1	Schematics of the LTSFM UHV system. In (a) the microscope and preparation chamber seen on the left and right, respectively. (b) the cryostat, and (c) the scanning force microscope.	14
2.2	Schematic diagram of the LTSFM scanning and data acquisition. Cantilever is driven on resonance f_0 and amplitude A by a piezoelectric. Deflection of the cantilever is detected by Fabry-Perot interferometer.	15
2.3	Schematics of a magnetic tip over a sample with a large/small domains with up/down magnetization. q_{tip} depends on the spatial wavelengths of the field. . .	16
2.4	The actual tip-sample distance $z_{measured}$ can be determined from the dependence of the A_{exc} -signal on the tip-sample distance z . (a) shows the dependence of the frequency shift on the tip-sample distance travel (bottom z-scale). (b) shows the dependence of the excitation signal on the tip-sample distance. At a tip-sample distance smaller than a critical tip-sample distance $z_{critical}$ the excitation signal increases rapidly. This point in the tip-sample distance is used to define the zero-point of the absolute z-scale shown at the top axis of (b) and also (a). For imaging the tip is retracted 9 nm from this point (a). A topography induced local variation of the tip-sample distance of ± 2.2 nm would then cause a variation of the frequency shift of ± 1.75 Hz.	19
2.5	(a) MFM contrast caused by the up/down domains of the F-layer only. The contributions of the topography and the AF have been removed. (b) Note that the transitions from up-to-down domains (see red arrow) running along the x-direction show a characteristic dark shadow that is not visible in the corresponding down-to-up transitions in (c) (see yellow arrow). This asymmetry is not visible for domain walls (transition) running along the x-direction. The asymmetry of walls along the y-direction is caused by the canting of the cantilever along this direction by 12° , i.e. by the lever-canting function, LCF(\mathbf{k}) (Eqn. 2.6). The <i>decanted</i> data is shown in (d). The cross-sections (b) and (e) clearly reveal the effect of the <i>decanting</i> procedure. Now the walls running along the x- and y-direction (Fig 2.5 (e) and (f)) are symmetrical.	20
2.6	Procedure to create a Magnetization pattern and to calibrate an MFM tip: (a) $1\mu\text{m}\times 1\mu\text{m}$ MFM images acquired after zero-field cooling at 8.3 K. (b) is the calculation of the decanted image with the image is more closer and thickness loss partially removed. (c) shows the magnetization pattern which is determined by a discrimination process. (d) shows the stray field gradient is calculated from the magnetization pattern. (e) is the tip-transfer function which is calculated by dividing the FFT of the acquired image (a) by the FFT of the stray field gradient (d).	21

- 2.7 (a) ICF_{tf} , (b) the $ICF_{tf-circ-averaged}$. Test of the calibration functions: (c), and (d) are the simulated images by using ICF_{tf} and $ICF_{tf-circ-averaged}$, respectively. (e) is $1\mu m \times 1\mu m$ MFM images acquired after zero-field cooling at 8.3 K. (f) and (g) are the differences of the simulated images from the acquired image, (e). 22
- 2.8 Simulation of the different sized patterns (a), (b), and (c) are the square pattern with a 10, 20 and 40 nm size. (e), (f), and (g) are the simulations of the pattern by using the non-averaged tip transfer function, ICF_{tf} (Fig. 2.8 (d)). Also (i), (j), and (k) are the simulations of the square patterns by using circularly averaged tip-transfer function, $ICF_{tf-circ.averaged}$, (Fig. 2.8 (h)). 23
- 3.1 Schematic diagram showing the F/AF moment directions and distributions at the ideal F/AF interface. The m_F describe the distribution of magnetic moments, in ferromagnetic layer that are aligned co-linear and parallel. At the interface they coupled to the sub-lattice of AF, m_{AF} (yellow moments). All the sub-lattice of AF (yellow and orange moments of AF) are also aligned co-linear but antiparallel to have a zero net magnetic moment. The F and AF-layers have an atomically smooth interface, so that the interfacial AF moment plane is a fully uncompensated. Such an ideal interface would then generate a strong unidirectional anisotropy of the F-layer and leads to an EB-effect. 26
- 3.2 Schematic diagram of the sample showing the magnetic moments directions and distributions at the realistic F/AF interface. There is an interface region due the atomically rough surface and the chemically inter-mixed F/AF-layer. For simplicity all the magnetic moments aligned co-linear. Bubbles show the different possibility of the interaction that can be occurred at the interface or in F/AF. Magnetic moments of F labelled as $m_F^{p,r-uc}$ and that of AF for each sub-lattice as $m_{AF}^{p,r-uc}$. Here, “uc” used for uncompensated, “p” for pinned and “r” for rotating type of magnetic moments. When the magnetic moments of two AF sub-lattices inside AF couples as depicted in (a) that gives no net magnetization. Defects existed inside AF (b) leads to net magnetization that may pinned to one of the AF sub-lattice or in a paramagnetic state. There is an intermixing of F and AF magnetic moments near or at the interface as depicted in (c) and (d). Former case may also behave as a defective AF as in (b) situation. (e) shows the possibility of parallel or antiparallel coupling of F magnetic moments with the AF ones that may be pinned or rotating types. If AF magnetic moments pinned to AF sub-lattice, this will contribute to EB-effect, If not, for rotating type of spins will follow the magnetization of F magnetic moments and leads to increase of the coercivity of F-layer. (f) shows the interaction of the F magnetic moments inside F-layer with intrinsic ferromagnetic exchange coupling. 27
- 3.3 Measurement of the contrast arising from the hidden layers, (a) MFM image of the F-stripe domain pattern after zero-field cooling and (b) after 850 mT applied field to saturate the F-layer magnetization giving the contrast only due to the pinned uncompensated moments of AF, $\Delta f_{AF}(D_{AF}, m_{AF}^{p-uc})$ 30

- 3.4 Separation of Van der Waal's and Magnetic Forces: (a) and (b) shows the MFM contrast taken with opposite tip magnetization at the area of the sample with the same tip-sample surface distance. (c) one half of the sum of the MFM images in (b) and (c) gives the topography-induced contrast. (d) one half of the difference of the MFM images in (b) and (c) gives the magnetic field generated contrast. 31
- 3.5 Schematic structure of the sample to keep the measurement surface closer to the sample surface so that the contrast due to solely pinned uncompensated AF moments can be visible by our MFM. Single F layer is Pt(5nm)/AF/F/Pt(2nm) with AF as 1.5 nm $\text{Co}_{0.8}\text{Cr}_{0.2}\text{O}$, F as 4 repeated $[\text{Co}(0.3\text{nm})/\text{Pt}(0.7\text{nm})]_4/\text{Co}(0.3\text{nm})$. (b) MFM image of the single F layer sample with micron-sized domains. The contrast of (b) is generated by the F layer ($\Delta f_F(D_F, M_F, \text{topo}_F)$), pinned and rotating uncompensated moments of AF layer ($\Delta f_{AF}(D_{AF}, m_{AF}^{r-uc}, \text{topo}_{AF})$) and the topography-induced vdW force ($\Delta f_{vdW}(\text{topo})$). 33
- 3.6 (a) after zero-field cooling to 8.3 K; (b) MFM contrast is generated by the F layer, pinned and rotating uncompensated moments of AF layer, and the topography-induced vdW force. Note that the contrast generated by F-layer depends on the geometry of the F-domains D_F . Yellow circles in (a), (c), (e), (g), (i) and (k) indicates some topographical features. (c) saturation of the F layer in 1 T, field applied parallel to tip magnetization; (d) Note that now the arises from the saturated F-layer, and notice further that the frequency shift generated by the rotating moments changed, from $\Delta f_{AF}(D_{AF}, m_{AF}^{r-uc}, \text{topo}_{AF})$ at 0 mT to $\Delta f_{AF}^{+1T}(\text{Sat}_{AF}, m_{AF}^{r-uc}, \text{topo}_{AF})$ in a field of 1 T. The distribution of the pinned AF moments (m_{AF}^{p-uc}) does not change with the applied field. (e) saturation in -1 T, field applied antiparallel to tip magnetization; (f) Note that the contrast generated by the imprinted pinned uncompensated AF moments now reversed, because the magnetization of the tip has reversed. (g) is semi sum of the MFM image taken in +1 T and -1 T; (h) shows the contrast contribution of the MFM image (g). (i) is semi difference of the MFM image taken in +1 T and -1 T; (j) the contrast generated by the pinned AF moments only. (k) recovery of (a) at +0.26 T after (e). 34
- 3.7 (a) model F-domain pattern. (b) domain wall contrast in calculated dH_z/dz -pattern. (c) model UCS pattern. (d) corresponding dH_z/dz -pattern. 36
- 3.8 Schematic structure of the sample to keep the measurement surface closer to the sample surface so that the contrast due to solely pinned uncompensated AF moments can be visible by our MFM. Double F layer is Pt(5nm) $\text{F}^{(bottom)}$ /AF/ $\text{F}^{(top)}$ /Pt(2nm) with AF as 1.5 nm $\text{Co}_{0.8}\text{Cr}_{0.2}\text{O}$, $\text{F}^{(top)}$ as 4 repeated $[\text{Co}(0.3\text{nm})/\text{Pt}(0.7\text{nm})]_4/\text{Co}(0.3\text{nm})$. (b) MFM image of the double F layer sample with a few hundred nanometer-sized domains. The contrast of (b) is generated by the F layer ($\Delta f_F(D_F, M_F, \text{topo}_F)$), pinned and rotating uncompensated moments of AF-layer ($\Delta f_{AF}(D_{AF}, m_{AF}^{r-uc}, \text{topo}_{AF})$) and the topography-induced vdW force ($\Delta f_{vdW}(\text{topo})$). 38

- 3.9 Vibrating sample magnetometry loops recorded at room temperature (red) and after field cooling in 2 T to 8.3 K (black). At low temperatures, the two F-layers switch independently. $F^{(bottom)}$ switches symmetrically in lower fields while $F^{(top)}$ shows an EB field, $\mu_0 H_{eb} = -124.5$ mT. $1 \mu\text{m} \times 1 \mu\text{m}$ MFM data from double F-layer sample's domain contrast (a) after zero-field cooling to 8.3 K, (b) after the 0.09-0.12 T, (c) after 0.19 T, (d) after 0.38 T, (e) after 0.5 mT, (f) and after -0.5 T. 39
- 3.10 (a) after zero-field cooling to 8.3 K; (b) MFM contrast is generated by the F-layer, pinned and rotating uncompensated moments of AF-layer, and the topography-induced vdW force. Note that the contrast generated by F-layer depends on the geometry of the F-domains D_F . (c) saturation of the F-layer in 0.5 T, field applied parallel to tip magnetization; (d) Note that the contrast now arises from the saturated F-layer, and notice further that the frequency shift generated by the rotating moments changed, from $\Delta f_{AF}(D_{AF}, m_{AF}^{r-uc}, topo_{AF})$ to $\Delta f_{AF}^{+0.5T}(Sat_{AF}, m_{AF}^{r-uc}, topo_{AF})$ at saturation. The distribution of the pinned AF moments (m_{AF}^{p-uc}) does not change with the applied field. (e) saturation in -0.5 T, field applied antiparallel to tip magnetization; (f) Note that the contrast generated by the imprinted pinned uncompensated AF moments now reversed, because the magnetization of the tip has reversed. (g) is semi sum of the MFM image taken in +0.5 T and -0.5 T; (h) shows the contrast contributions of the MFM image (g) schematically. (i) is semi difference of the MFM image taken in +0.5 T and -0.5 T; (j) the contrast generated by the pinned AF moments only. (k) is the subtraction (g) and (i) from (a) with a less granular contrast. 41
- 3.11 Model calculation (a) a checker-board pattern created with a feature size of 5×5 pixels corresponding to $19.53 \text{ nm} \times 19.53 \text{ nm}$ is used for the model calculations. (b) roughness and thickness variations of F-layers. 42
- 3.12 (a) pattern of uncompensated magnetic moments per unit area, as obtained from the deconvolution of the frequency shift pattern generated by the pinned uncompensated AF moments, $\Delta f_{AF}(D_{AF}, m_{AF}^{p-uc})$ 43
- 3.13 Calculation of the average pinned AF moment density: a) is the pinned uncompensated moment distribution deconvolved from the contrast of pinned uncompensated AF moments. In b) and c) the masks are used to calculate the uncompensated moment density under white and black domains, respectively. . . 44
- 3.14 Simulation of the uncompensated moment pattern (a), compare (b) to Fig. 3.10 (e) which is the contrast due to the pinned uncompensated moments in AF layer or at the interface. d) is the difference of the simulated pattern (b) and pinned uncompensated AF contrast (c) , note the scale is 1/10 45
- 3.15 In a) and b) the masks are inserted for the calculation of the average contrast of up-down (white-black) domains for the F layer. In c) and d) the same masks are used for up/down pinned uncompensated moments of the AF layer. 46
- 3.16 coupling via another atom; (a) a weaker antiferromagnetic coupling between the F moments and the pinned AF moments, (b) the uncompensated AF moments remain locked as the reversal of the F magnetization. (c) Direct coupling of the F moments with the uncompensated moments, (d) reversal of the F magnetization breaks the coupling of F moments with the uncompensated moments, thus the latter rotates with the former. 48

4.1	MFM images of the as-grown CoO/CoPt-singlelayer sample: The $2 \times 2 \mu\text{m}^2$ sized MFM image is taken in 0 mT (a). (b)-(d) show the AFM-contrast observed in +300 mT, when the FM layer is saturated. The contour lines of the FM domains in 0 mT (a), +100 mT and +200 mT were overlaid to the AFM-contrast and are shown in (b)-(d), respectively. In (b)-(d), the contrast arising from the uncompensated moment is dark(light) under the white(black) F-domains, i.e. antiparallel coupling. However, in some isolated locations (anti-biasing regions) the contrast is light(dark) under white(black) F-domains, i.e. parallel coupling. By increasing the field from 0 mT \rightarrow +100 mT \rightarrow +200 mT, the “white” F-domains show the tendency to retract from locations with positive coupling (anti-biasing regions, marked by yellow arrows), and the average AF-contrast below these domains (see (d)) becomes more negative.	50
4.2	Schematic of a F/AF coupling frustration spanning the interface area of multiple AF grains. (a) Fully uncompensated AF interfaces have steps, leading to intra-grain frustration. Due to exchange coupling to neighboring grains the F/AF interface area of one grain may have an overall parallel coupling, i.e. have an anti-biasing contribution to the total coupling. (b) Removing the inter-grain coupling allows each AF grain to minimize the total F/AF coupling energy independently. The net coupling over the F/AF interface of a given grain is therefore anti-parallel, i.e. biasing.	51
4.3	Schematic layout of the multilayers of the exchange biased samples used. Both samples have the structure Si/Pt/[CoPt] ₁₀ /Cu/[Co _{1-x} Cr _x O]/[CoPt] ₄ /Pt. Sample A corresponds to $x = 0$, and sample B corresponds to $x = 20\%$	52
4.4	Magnetometry of exchange bias samples at room temperature and 7.9 K. (a) sample A (CoO antiferromagnet. (b) Sample B (grain-boundary engineered CoO).	53
4.5	MFM measurements of $1 \times 1 \mu\text{m}^2$ areas of sample A and B. The measurements were taken up to saturation, and record first the shrinking of the light domains, then their break up, then their disappearance. For sample B these processes occur at higher applied fields.	55
4.6	MFM study of the recovery of the initial domains’ structure after saturation. (a) Initial top-layer (coercivity of bottom layer is smaller than 150 mT) domain configuration in sample A. (b) Partial recovery at -150 mT (negative saturation of the bottom ferromagnet). (c) Initial top-layer domain configuration in sample B. (d) Near perfect recovery at -150 mT.	56
4.7	Calculation of the local density pinned AF moment for samples A and B. In (a) and (c), contrast generated by the F-domain pattern of the upper F-layer, and In (c) and (d) by the imprinted pinned uncompensated moments.	56
4.8	Imprinted pinned UCS is color coded in shades of red and yellow for each orientation.	57
5.1	Schematic structure of Sample 1 in (a) and Sample 2 in (b).	60

- 5.2 Vibrating sample magnetometry results of the ferrimagnet, sample 1. In blue: magnetic moment per unit area, \tilde{m} . Below the compensation temperature $T_{comp} \approx 330 \pm 5$ K, Tb dominates the magnetization. In red: coercivity. Green shaded area: estimated range for the perpendicular anisotropy. Lower right schematic: the film's Tb and Fe moments illustrate the relative moment direction and qualitative size on either extreme of the temperature scale. Inset upper right: Hysteresis loops acquired at 50 K and 280 K. 61
- 5.3 Magnetometry of the ferromagnet/ferrimagnet bilayer, sample 2. At applied fields of 1 T the 7.9 K hysteresis loop (blue curve) displays a switching process corresponding to the ferromagnet, which is thus exchange-biased. At 280 K the corresponding exchange-bias amounts to 0.8 T (red curve). The shaded areas represent the energy required in the switching, with the average termed $\sigma_{int}^{7.9K}$ and σ_{int}^{280K} at 7.9 K and 280 K respectively. Inset diagrams indicate the relative magnetic moment orientation of the different elements in the bilayer. The exchange-bias as a function of temperature, obtained from hysteresis loops such as the ones plotted here is given in the upper left inset 62
- 5.4 Magnetic force microscopy (MFM) characterization RE-ferrimagnet-based exchange bias systems at 7.9 K. (a–e) $2 \times 2 \mu\text{m}^2$ images of sample 1 (ferrimagnet) obtained at 30 nm tip-sample distance at applied fields of 0 T, 0.5 T, 1.75 T and 7 T, with return to 0 T. The shape and contrast of the magnetic domains is essentially constant, indicating that the magnetic structures are stable in applied fields of at least 7 T. (f–j) $2 \times 2 \mu\text{m}^2$ images of sample 2 (ferrimagnet+ferromagnet) obtained at 35 nm tip-sample distance at the same field levels as in (a–e). The initial contrast is much weaker than in (a–e), and increases to these levels for fields ≥ 2 T. The structures, however, do not change shape as during the magnetization by vertical domain wall motion in perpendicular magnetization systems. (k) Image contrast obtained from the images in (a–j) and other intermediate fields (images not shown). Sample 2 is seen to attain the same contrast level as sample 1 once the ferromagnetic layer has been saturated. The smaller contrast prior to saturation is consistent with the ferromagnet's antiparallel alignment with the ferrimagnet, which results in a smaller areal density of magnetic moment. (l)–(n) Schematic arrangement of magnetic domains in the bilayer system of sample 2, and the effective portions contributing to the MFM signal. A homogeneously magnetized film layer does not result in stray fields; in particular the saturated ferromagnetic layer is “transparent” to the MFM. 64
- 5.5 MFM of a $500 \text{ nm}^2 \times 500 \text{ nm}^2$ area obtained at 1 T, 1.75 T and 3 T for increasing and then decreasing fields respectively, showing a fine magnetic structure (sample 2). 65
- 5.6 Magnetic force microscopy images of the ferrimagnetic/ferromagnetic sample 2. (a) image obtained at +1 T applied field. (b) image obtained at –1 T. The contrast is inverted in (b) to correct a contrast inversion arising from the flipped tip magnetization, and allow a more direct comparison of the images. 66

List of Symbols and Abbreviations

$EB - effect$	exchange bias effect
F	ferromagnet, ferromagnetic
AF	antiferromagnet, antiferromagnetic
H	magnetic field
H_{min}	minimum magnetic field
H_{eb}	exchange field
H_c	coercive field
H_{cool}	cooling field
H_{sw+}	positive switching field
H_{sw-}	negative switching field
T_C	Curie temperature of the F
T_N	Neel temperature of the AF
T_B	blocking temperature of the AF
M_F	saturation magnetisation(of the F)
t_F	thickness of the F layer
t_{AF}	thickness of the AF layer
m_{uc}	uncompensated magnetic moment
m_{uc}^p	pinned uncompensated magnetic moment
m_{uc}^r	rotatable uncompensated magnetic moment
D_F/S_F	domain/saturation state (of the F)
D_{AF}/S_{AF}	domain/saturation state (of the AF)
A_{AF}	exchange stiffness of AF
A_{12}	interlayer exchange stiffness
K_F, K_{AF}	anisotropy constants of F and AF, respectively
K_u^{est}	estimated uniaxial anisotropy (Chapter 5)
J_{eb}	interfacial exchange anisotropy
J_{eff}	effective anisotropy in spin glass model
K_{eff}^{SG}	effective spin glass anisotropy

ΔE	interface anisotropy energy/unit area
L	AFM crystallite diameter
Q	quality factor
z	tip/sample distance
A	(unit) sample area
A_{osz}	amplitude of cantilever oscillation
c_L	spring constant of free cantilever
c_{eff}	spring constant of cantilever
f_0	resonance frequency of free cantilever
f_{eff}	resonance frequency of cantilever
Δf	frequency shift
ϕ	magnetic potential
F_n	force normal to a surface
F_{exc}	excitation force
F_{ts}	tip/sample interaction force
F_z	force in z-direction
$q_{tip}(k)$	Fourier transform of a tip-equivalent surface charge pattern
\mathbf{k}	k-vector: (k_x, k_y)
\mathbf{r}	r-vector: (x, y)
\tilde{m}_r	remanent magnetic moment areal density
T_{com}	Compensation temperature
σ_{int}	inter-layer coupling energy
UCS	uncompensated spins
TRM	thermoremanent magnetisation
MRAM	Magnetoresistive random-access memory
XMCD	x-ray magnetic circular dichroism
FC, ZFC	field cooled, zero-field cooled
VSM	vibrating sample magnetometer
TEM	transmission electron microscopy
RBS	Rutherford back scattering
GMR	giant magnetoresistance
RE	Rare-earth
DW	domain wall
DAFF	diluted antiferromagnetis in external field
MFM	magnetic force microscopy
SFM	scanning force microscopy

UHV	ultra high vacuum
PLL	phase-locked loop
LTSFM	low temperature scanning force microscope
LCF	lever canting function
ICF	instrument calibration function

Acknowledgements

This thesis would not have been possible without the cooperation and support of many collaborators and friends. I'd like to express my gratitude to all of them. I would like to express my gratitude to Prof. Dr. H. J. Hug who gave me the great chance to do a PhD thesis in his group. I wish to thank Hans for his support and patient explanations during my thesis work and for his help to complete this thesis.

I would like also to thank the following people that helped me to complete this thesis:

- Dr. Miguel Marioni for sharing his wide knowledge on all aspects of magnetism, and for helping me to read and correct the draft of the dissertation. I benefited a lot from the discussions that we had.
- Dr. Niraj Joshi with whom I did the measurements presented in this thesis. He has shared his experience with me, and encourage me in the difficult moments.
- Dr. Sara Romer for preparing the samples that we used in this thesis, and for helping me to read and correct the draft of the dissertation.
- Prof. Dr. Ernst Meyer and Prof. Dr. Martino Poggio for kindly accepting to be the external examiner for my thesis.
- Yves Pellmont for help in our laboratory regarding mechanical and technical issues.
- Germaine Weaver for her kind attitudes and help with the beaurocratical issues.
- Muge Deniz Yuksek, Ceyda Sanli, Deniz Cakir, Neriman-Halil Cebeci family and Serpil Boz for their support and friendship.
- My parents, Emine-Sabri Ozer for their support through my whole life.
- Finally, My old brothers Yahya and Sinan Ozer, and my twin Soner Ozer. They are always with me.

List of Presentations and Publications

Talks

- S. Ozer, N. Joshi, S. Romer, M. Marioni and H. J. Hug. *Exchange-bias Effect studied by quantitative Magnetic Force Microscopy*, Yale University, Connecticut, USA, November, 2011.
- S. Ozer, N. Joshi, P. Stickar, T.V. Ashworth, S. Romer, M. Marioni and H. J. Hug. *Engineering the ferromagnetic domain size for optimized imaging of the pinned uncompensated spins in exchange-biased samples by magnetic force microscopy*, MMM 2011, Scottsdale AZ, USA, October, 2011.
- S. Ozer, N. Joshi, S. Romer, M. Marioni and H. J. Hug. *Contrast Formation and Deconvolution of pinned UCS by MFM*, DPG, Dresden, Germany, March 2011.
- S. Ozer, N. Joshi, S. Romer, M. Marioni and H. J. Hug. *Exchange bias enhancement by Cr addition to CoO in a CoO-Co/Pt multilayer system*, International Conference on Nanoscale Magnetism, Gebze, Turkiye, September 2010.
- S. Ozer, N. Joshi, P. Stickar, S. Romer, M. Marioni and H. J. Hug. *Exchange bias enhancement by Cr addition to CoO in a CoO-Co/Pt multilayer system*, SPG, Basel, Switzerland, June 2010.

Posters

- N. Joshi, S. Ozer, S. Romer, and M. Marioni, and H. J. Hug. *How to map Pinned Uncompensated Spins in Exchange Biased Systems by MFM*, IEEE 7th International Symposium on Metallic Multilayers (MML2010), Berkeley CA, USA, September 2010.
- S. Ozer, N. Joshi, S. Romer, M. Marioni and H. J. Hug. *Mapping Pinned Uncompensated Spins in Antiferromagnet/Ferromagnet Systems by high-resolution Magnetic Force Microscopy*, Fourth Seeheim Conference on Magnetism, Frankfurt, Germany, March 2010.

Publications

- N. Joshi, S. Ozer, P. Stickar, T.V. Ashworth, S. Romer, M. Marioni and H. J. Hug. *Engineering the ferromagnetic domain size for optimized imaging of the pinned uncompensated*

spins in exchange-biased samples by magnetic force microscopy, Appl. Phys. Lett. 98, 082502 (2011).

- M.A. Marioni, S. Romer, N. R. Joshi, S. Oezer, K. Thorwarth, M. Parlinska-Wojtan, T.V. Ashworth, H. Rohrmann, H.J. Hug. *Giant Exchange-Bias: beyond 1 Tesla by frustration avoidance. (Submitted).*
- S. Ozer, N. Joshi, S. Romer, M. Marioni and H. J. Hug. *Imaging of Pinned Uncompensated Spins in Exchange-Bias Systems by Quantitative Magnetic Force Microscopy. (In preparation).*

Curriculum Vitae

07. February 1981 Born in Istanbul (Turkiye), Daughter of Emine and Sabri Özer.
- 1987-1995 Primary and secondary school in Istanbul (Turkiye).
- 1995-1998 High school, “Bakirköy Lisesi”, Istanbul.
- 1998-2000 English preparation school and study of physics,
“Abant İzzet Baysal University”, Bolu (Turkiye).
- 2000-2003 Study of Physics, “Middle East Technical University” in Ankara (Turkiye).
- 2003-2006 Study of Physics (Master of Science), “Bilkent University” in Ankara (Turkiye)
under Prof. Dr. Recai Ellialtıoglu and Dr. Tarık Reyhan,
- 2006-2007 Study of Physics, “Bilkent University” in Ankara (Turkiye)
under Prof. Dr. Ahmet Oral.
- 2008-2012 Ph.D. thesis in Physics at University of Basel, Switzerland.
under Prof. Dr. Hans Josef Hug.